THERMAL TRANSPORT PROPERTIES OF NANOPOROUS ZEOLITE THIN FILMS

A Dissertation
Presented to
The Academic Faculty

by

YENY HUDIONO

In Partial Fulfillment
of the Requirements for the Degree
Doctor of Philosophy in Chemical Engineering in the
School of Chemical & Biomolecular Engineering

Georgia Institute of Technology
August 2008

THERMAL TRANSPORT PROPERTIES OF NANOPOROUS ZEOLITE THIN FILMS

Approved by:

Dr. Sankar Nair, Advisor
School of Chemical & Biomolecular Engineering
Georgia Institute of Technology

Dr. Amyn S. Teja
School of Chemical & Biomolecular Engineering
Georgia Institute of Technology

Dr. Samuel Graham, Co-Advisor
School of Mechanical Engineering
Georgia Institute of Technology

Dr. Peter J. Ludovice
School of Chemical & Biomolecular Engineering
Georgia Institute of Technology

Dr. Mo Li
School of Materials Science and Engineering
Georgia Institute of Technology

Date Approved: June 19, 2008

Dedicated to the memory of

My grandmother,

whose support and trust
has continually inspired me.

ACKNOWLEDGEMENTS

Success is not final, failure is not fatal; it is the courage to continue that counts ~ Sir Winston Churchill.

This quote best describes the ups and downs of my stay at Georgia Tech. My journey of completing a doctorate degree has not been solely a great technical learning experience, but most and foremost it has been a great life training experience; and I thank God for giving me great mentors, colleagues, friends and family who have guided, taught, encouraged and trusted me during these four and half years. Without them, this journey would have been unattainable.

I would like to express my most sincere gratitude to my advisor, Prof. Sankar Nair, for taking me as his student and extending continuous encouragement, support and guidance. His support, patience and intelligence have inspired and enriched my growth as a student, and as a researcher. Thank you for being an example and an inspiration for excellence and dedication.

I would also like to express my most sincere gratitude to my co-advisor, Prof. Samuel Graham for taking me as his student and extending unflagging support, guidance and trust. His support has been a tremendous motivator in the completion of this thesis, especially in conducting difficult thermal conductivity measurements. He is one of the great teachers I have known.

I would like to thank my committee members Prof. Amyn Teja, Prof. Peter Ludovice, and Prof. Mo Li for serving on my committee and providing valuable suggestions during this work. I am grateful to acknowledge Abraham Greenstein for his invaluable work, which was a critical part of our research collaboration. His originality

and dedication have inspired my intellectual maturity, from which I will benefit for a long time to come.

I would also like to thank Adam Christensen and Prof. Brandon Olson (University of Oklahoma) and for their invaluable time and discussion on 3-omega method. Their assistance was extremely helpful in the early stages of this research. I would like to thank Namsu Kim and Amir Ahmadi for their assistance on heater fabrication, and to Carine Saha Kuete for her work on zeolite MFI membrane synthesis under my supervision.

I am grateful to Dr. Yolande Berta, Todd Walters, Yueming Hua, and Yonghao Xiu for their assistance with microscopy techniques. I would like to express my sincere gratitude to Jeff Andrews and Brad Parker for their tremendous support in the machine shop without which my research would not be possible. I am grateful to the Georgia Institute of Technology and the National Science Foundation for financial support of this research.

I would like to thank Graham and Nair groups, whose friendship has encouraged me to continue working hard in the lab. Special thanks to Dr. Sanjoy Mukherjee, Dr. Weontae Oh, Dr. Chilhung Cheng, and Suchitra Konduri, whose friendship and advice have been a tremendous support for my growth as a doctoral student.

My parents deserve special gratitude for their prayers and trust, especially to my father, whose dedication has inspired me to pursue beyond what I could ever imagine a few years ago; and to my mother who has trusted and lovingly supported me throughout. To my siblings, Lanny, Fanny and Shianny who have cheered me up anytime I went through a difficult time. And to all my dearest friends: Fel, Gracy, Dewi, Reginald, Rentian, Steph, Shu, Suchi, Sanjoy, Henry, Preeti, Ashwini, YongHao, Fr. Mario, Ang, Icha, and Lany who I have indebted a tremendous support and encouragement. And to all friends and

acquaintances whom I have not mentioned but had been there for me along the way. Thank you!

TABLE OF CONTENTS

LIST OF TABLES

LIST OF FIGURES

SUMMARY

In comparison to other transport properties, the thermal transport properties of solid materials remain the least understood. Due to increasing complexity in the structure of new classes of materials (e.g. nanopores) and increasing importance of thermal transport phenomena in many technological applications based upon these materials, it is critical to understand thermal transport mechanisms in these materials, and their dependence on the material structure. There are both experimental difficulties as well as theoretical challenges in measuring and describing thermal transport in complex materials. This thesis focuses on the thermal transport properties of zeolite materials due to their well defined, yet complex, crystal structures. The capability of altering the composition of a given zeolite (e.g. by lattice atom substitution or by introducing metal cations and organic molecules into the pores) while maintaining the same framework structure, or conversely the ability to synthesize different framework structures with the same composition, make zeolites extraordinarily versatile materials with interesting structure–function relationships as well as many important applications. This thesis focuses on two types of zeolite materials, MFI and LTA. The zeolite MFI was used as model to examine thermal transport mechanisms in zeolite and to study the effects of framework atoms substitution on the thermal conductivity. On the other hand, the effects of non-framework cations on thermal conductivity were studied using LTA zeolite.

This work focused on developing reliable experimental approaches to obtain the thermal transport properties of both MFI and LTA, and also on understanding heat

transport mechanisms both quantitatively and qualitatively. To achieve the overall objectives, this thesis consists of the following aspects:

(I) *Hydrothermal synthesis (by the "secondary growth" method) of well-intergrown and preferentially oriented zeolite films with various Si/Al ratios (MFI) and non-framework cations (LTA).* The films were characterized using Scanning Electron Microscopy (SEM), Energy Dispersive X-ray Spectroscopy (EDS), X-ray Diffraction (XRD) to investigate the morphology, composition and orientation of the film. A series of sample preparation steps including sample polishing and surface roughness measurement using atomic force microscopy are presented in order to obtain reliable thermal conductivity measurements.

(II) *Investigation of the effects of framework cations on thermal transport properties*. Here, we measure the thermal conductivity of a series of MFI zeolite films with various Si/Al ratios using a 3-omega method. The phonon transport mechanisms were then analyzed using a Boltzmann Transport Equation (BTE), and the relaxation times for different scattering processes were fitted to the experiment data.

(III) *Investigation of the effects of non-framework cations on thermal transport properties*. Here, we measure the thermal conductivity of a series of LTA zeolite. Synthesis of LTA zeolite films via secondary hydrothermal method is presented. The effects of cation size and valency on thermal conductivity were investigated.

(IV) *The thermal conductivity can also be studied via molecular dynamics simulation*. A non equilibrium molecular dynamics simulation was constructed to investigate the thermal conductivity of zeolite materials. Even though, this method can predict the thermal conductivity of simple Lennard Jones solid, the effects of temperature on the thermal conductivity of zeolite materials cannot be predicted accurately. The incorporation of quantum effects in the MD simulation is necessary.

This thesis has therefore addressed several of the fundamental challenges in correlating the structure–thermal transport properties of complex crystalline zeolite materials. By demonstrating the requisite experimental techniques for reliable thermal property measurements, then investigating the effects of both the framework and non-framework cations on the thermal conductivity of zeolite, and by separately analyzing the contributions of different phonon scattering processes, this thesis represents our progress towards a robust framework for understanding and predicting thermal transport properties of zeolite materials and complex crystals in general. Furthermore, the important roles of boundary and defect scattering, as illustrated in this thesis, also imply that the thermal conductivity of zeolite materials can be tuned by exploiting not only the composition but also the pore structure.

CHAPTER 1

INTRODUCTION

1.1 Motivation

One of the major challenges in nanoscience and nanotechnology is the development of accurate structure-property relationships of nanostructured materials [1]. Transport properties (e.g., mass, electrical, thermal) of nanostructured materials constitute a technologically important class of functional properties, that are of relevance in the engineering of devices and systems that employ nanostructured materials. Thermal transport properties of nanostructured materials have remained the least well-understood among all transport properties. The interest in thermal transport properties of materials was initially catalyzed by the thermal management challenges occurring in the operation of integrated circuits for microelectronics applications [2]. For example, the shrinkage of field-effect-transistors (FETs) and interconnects to a sub-100 nm regime will pose serious difficulties of higher electrical resistance and hence higher heat generation, which make the development of new cooling methods necessary [3]. Efficient heat transfer is also a serious issue in the development of new dielectric materials used for packaging electronic devices. On the other hand, the development of ultra-low thermal conductivity materials is also of important in the development of heat-insulating materials for a variety of applications, such as for jet engines. The high thermal conductivity materials are used as heat sinks, and heat dissipation is achieved by an increase in the phonon velocity. In contrast, the ultra-low thermal conductivity materials, which can be constructed by introducing point defects or interfaces (created by fabricating multilayer of thin films)

[2], are often used for power generation systems, thermal barrier coatings for jet engines and thermoelectric refrigeration. Figure 1 shows a schematic of range of thermal transport properties of various nanostructured materials.

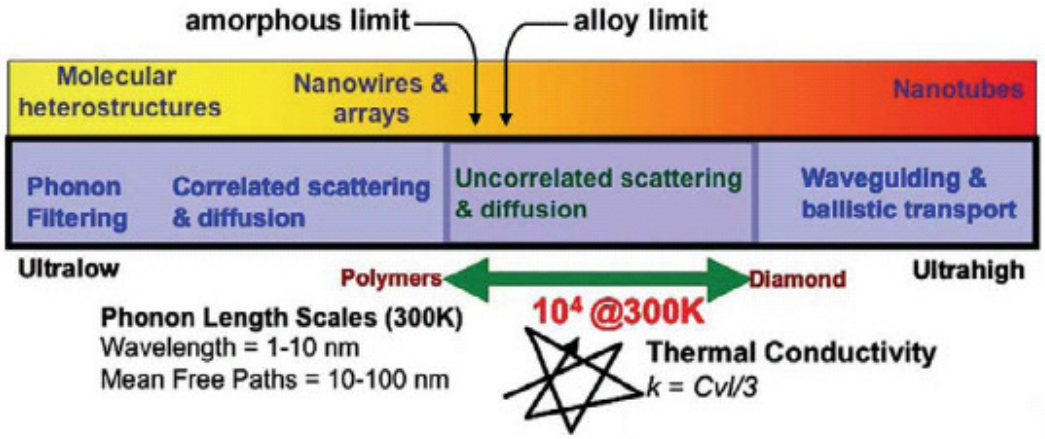

Figure 1: Schematic of approaches to expand the limits of thermal transport properties [2]

In nonmetallic materials, heat is transported by the atomic vibrations of the crystal lattice (i.e., phonons). At room temperature, the phonon mean free path is in the range of ~1-100 nm, which is comparable to the size of the nanostructuring features. Thus, the thermal transport properties can be manipulated by engineering the structure of the material. As a result, increasing structural and dynamical complexity is a major characteristic of materials whose thermal properties are of technological relevance, including (a) porous nanostructured materials for low-*k* dielectric films, adsorption-thermoelectric cooling of electronic devices and for energy-efficient refrigeration or heat recovery; (b) organic photonic materials for light-emitting devices and solar cells; and (c) compound semiconductors for novel solid state lighting devices. However, current experimental and theoretical knowledge of the thermal properties of these intriguing complex materials is inadequate. Thermophysical models widely used for simpler

materials fail in the case of these complex materials, due to the existence of unusual structural characteristics (e.g., ordered nanopores, host-guest architectures, and mix compositions) that lead to complicated phonon propagation and scattering processes.

The primary goal of this research has been to provide a better characterization and understanding of thermal transport properties of nanostructured materials, particularly those having ordered nanoporous structures and host-guest architectures. We have chosen zeolite materials as a model to understand the thermal transport behavior of complex nanostructured materials. A zeolite is defined as a crystalline aluminosilicate with a framework structure composed of tetrahedral SiO_4 and AlO_4 units. Zeolite materials incorporate highly periodic pores, channels and cavities that can occupied by metal ions, organic molecules, or water molecules [4]. Zeolite materials are found naturally as minerals. However, most technologically useful zeolites are synthetic. There are approximately 135 different natural and synthetic zeolite frameworks with different pore/channel structures and hence different thermal properties. Furthermore, it is possible to tune the thermal transport properties of zeolite materials by altering or tuning the composition of the crystal framework or extra-framework species while retaining the material structure (and vice versa). The composition of zeolite materials can be varied in a pre-determined manner by a variety of techniques. For example, (i) zeolite materials can be synthesized with a wide range of Si/Al ratios, (ii) the metal ions (e.g., Na^+, K^+, Ca^{2+}) are included in the nanopores can be chemically exchanged, (iii) organic species or water molecules can be adsorbed in the pores at well-defined adsorption sites. This tunability may lead to several possibilities for engineering the thermal transport

properties, e.g. by using the “rattling” motions of metal ions or adsorbed species in the nanopores to control the thermal conductivity.

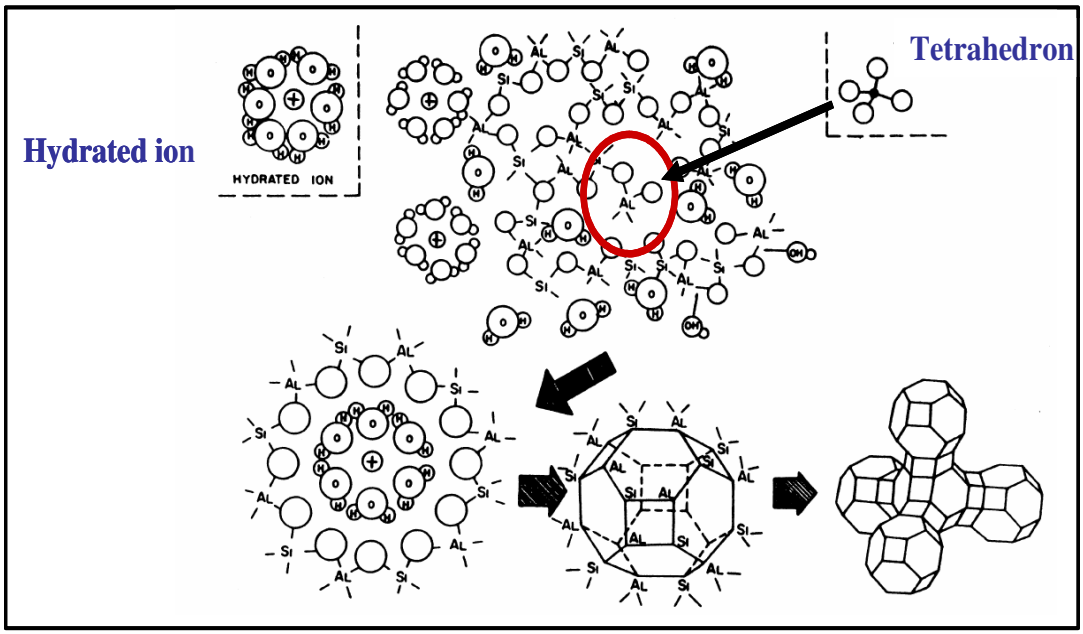

Figure 2: Schematic of zeolite synthesis mechanism [5]

Our interest in the thermal transport properties of zeolite materials originates primarily from their suitability as a model system containing complex, yet well-defined and characterizable, nanostructural features, such as an ordered nanopore network, lattice substitution sites, metal cations or organic species adsorbed in the pores. These nanostructure features interact with heat carrying phonons, and therefore, they offer a number of opportunities for developing and testing models for thermal conductivity in complex crystals. The rich structural complexity of these materials, as well as the increasing significance of thermal transport properties inherent in their emerging applications, justify detailed study of their thermal transport properties, of which current

knowledge is relatively limited. There are both experimental difficulties as well as theoretical challenges in describing thermal transport in complex materials with large unit cells [6-8]. This diversity of structural and physicochemical properties provides rich scope to test and refine thermal transport predictions incorporating a wide range of structural features and physical effects that can be expected in a complex material. Zeolite materials also have various and sometimes anomalous (e.g., negative thermal expansion) thermal transport properties [9, 10]. Thus, zeolite materials are a superior model that can be utilized to understand the thermal transport properties and phonons interactions in complex materials, consequently, this knowledge can facilitate the design of new materials. In addition, zeolite materials are considered for various novel applications in which heat transfer plays an important role. For example, zeolite materials are considered as a sorption-based heat exchanger either in stand-alone or hybrid mode (e.g., coupled with thermoelectric or solar-powered devices) as they offer efficient and inexpensive solutions to heat transfer problems in large-scale (> 1 kW) heat recovery and cooling, as well as in cooling small scale (< 100 W) microelectronic devices [11, 12]. The sorption efficiency strongly depends on the thermal conductivity of the sorption beds; consequently the understanding of structure-thermal transport property relationships of the zeolite material is critical. Recently, zeolite materials have also been considered as low dielectric materials [13, 14]. Zeolitic low-k dielectric film technology [15, 16] is currently being commercialized by semiconductor companies. High aluminum content zeolite is being investigated for coating of corrosive metal surface such as in heat exchanger [17, 18]. Moreover, zeolite materials can be used as rigid insulators [7] and

anodes in solid oxide fuel cells [19, 20] wherein an ultra-low thermal conductivity is required.

1.2 Background

There are only a few prior reports [7, 8, 21, 22] on the thermal properties of zeolitic materials. The thermal conductivity of zeolite materials is usually measured after compacting zeolite powder into a disk. The thermal conductivity is then measured by hot wire method [21]. The sample pellet powders are then saturated by an inert gas stream, and the effective thermal conductivity is measured. A model is used to extract the intrinsic thermal conductivity of the zeolite after subtracting the contribution from the gas thermal conductivity. This approach has several drawbacks. Since the measurements are made on a pelletized powder, the intrinsic thermal conductivity value is uncertain despite the existence of semi-empirical models to correct the experimental data for the presence of voids and particle-particle interfaces. Furthermore, many zeolites are highly anisotropic, whereas the use of palletized powders can only provide a measurement of the average (isotropic) properties of the material.

A computational approach for determining thermal transport properties of zeolite materials relies on molecular dynamics (MD) simulations using atomistic force fields. However, this is a difficult task [23] owing to the generally slow convergence of the computed heat flux. Equilibrium MD methods [7] can predict the specific heat with reasonable accuracy, whereas thermal conductivity is notoriously difficult to predict with equilibrium or non-equilibrium MD methods [8, 24]. In addition, the lack of comprehensive experiment data complicates the interpretation of simulated thermal

transport properties. There are only few reports on the thermal transport in zeolite materials using MD simulations [7, 8, 22]. There is also a discrepancy between the thermal conductivity of zeolite materials obtained by various authors from experiment and simulation (for example, Figure 4 shows the results of previous work for zeolite LTA). Based on the limitations summarized above, there is a need for development of methods for accurate measurement and prediction of the thermal transport properties of zeolite materials, and their correlation with the material structure.

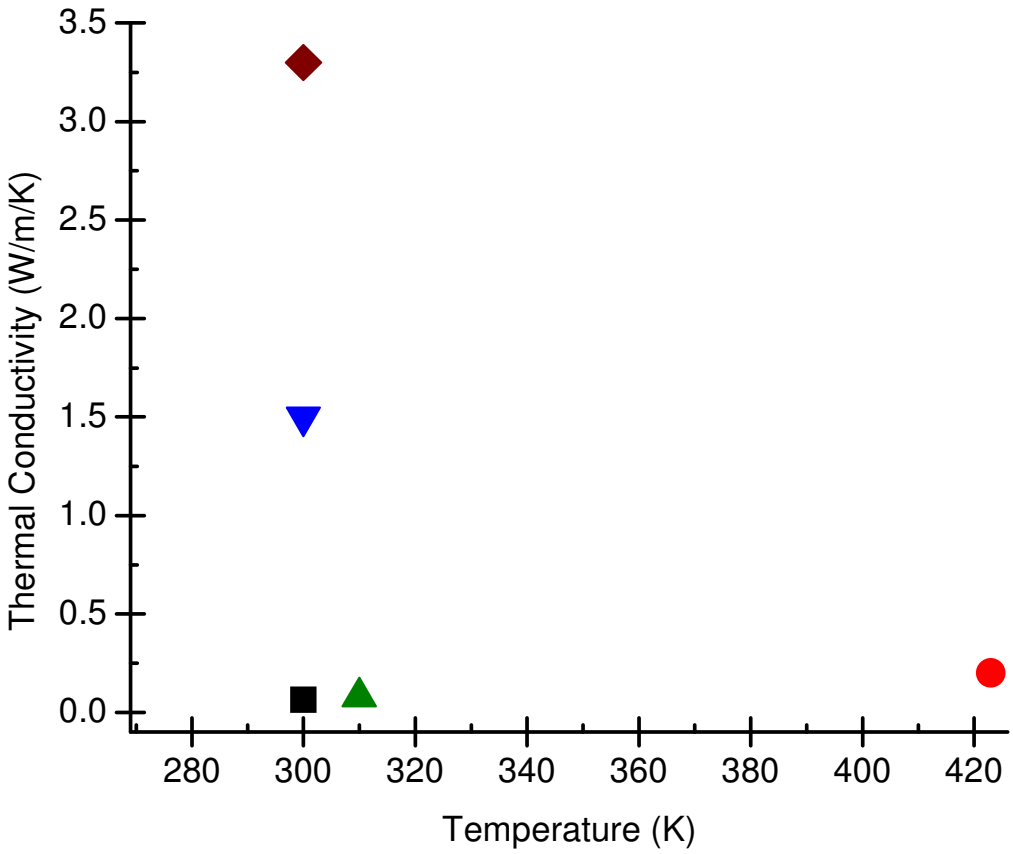

Figure 3: Thermal conductivity of LTA zeolite: diamond: calculated bulk thermal conductivity from the experiment result from [21], inverse triangle: simulation result from [7], rectangular: from [21], triangle: from [22],circle: from [21]

1.3 Objectives and Research Strategy

This thesis is motivated by the need to accurately measure and predict the thermal conductivity of zeolite, and to understand the thermal transport properties of complex nanostructured materials such as zeolites. Thus, the specific objectives of our research are:

1. Synthesis of well-intergrown preferentially oriented zeolite thin films of controlled structure and compostion, suitable for high-quality thermal transport measurements.
2. Direct and comprehensive measurements of thermal transport properties of zeolite thin films as a function of :
    i. Temperature
    ii. Framework composition (Si/Al ratio)
    iii. Non-framework composition (Metal cations)
3. Extraction and analysis of physically meaningful thermal transport (phonon scattering) parameters, by fitting experimental data to detailed theoretical models with significant computational input of other phonon properties such as dispersion curves.

One of the key challenges of this research is to accurately obtain thermal transport property measurements. This goal cannot be achieved using compacted powders of zeolite materials, due to the reasons described in the previous section. In this thesis, we are synthesizing well-intergrown zeolite films or controlled orientation and composition that are suitable for accurate measurements of the thermal transport properties. In Chapter 2, the synthesis and characterization of oriented MFI zeolite thin films with different

Si/Al ratio is discussed. The detailed measurements of thermal transport properties of MFI films, and the effects of Si/Al ratio on the thermal transport properties of zeolite materials such as MFI, are discussed in Chapter 3. Different phonon scattering mechanisms are considered and analyzed (in collaboration with Abraham Greenstein, Ph.D. Candidate in Mechanical Engineering) to develop a better understanding of phonon transport in zeolite materials. In Chapter 4, the synthesis of LTA zeolite films suitable for thermal transport property measurement are discussed, and the effects of non-framework cations on the thermal transport are discussed. The thermal transport properties of zeolite computationally studied as a function of Si/Al ratio and cations by non-equilibrium molecular dynamics simulation will be discussed in Chapter 5. Finally, concluding remarks and recommendations for future directions of the research are presented in Chapter 6.

CHAPTER 2

SYNTHESIS AND CHARACTERIZATION OF ZEOLITE MFI THIN FILMS FOR HIGH QUALITY THERMAL CONDUCTIVITY MEASUREMENT

2.1 Introduction

As mentioned in Chapter I, the thermal transport properties of zeolite materials were previously studied using zeolite powders which were compacted into a disk. Using this method, the measured thermal transport properties depend on the pellet density, and thus the bulk thermal transport property values were overestimated. Hence, a robust method of sample preparation and characterization is necessary to study the structure – property relationships, as will be described in this chapter. We use a hydrothermal method (called "secondary growth") to grow an oriented and dense zeolite crystal layer from an initial layer of deposited nanocrystals of the zeolite. The thermal transport properties can hence be accurately measured, and the anisotropic thermal transport properties can also be extracted using films of different orientations. Furthermore, this chapter introduces a secondary growth method to synthesize a series of oriented zeolite membranes with various Si/Al ratios and constant out-of-plane orientation.

This chapter will focus on the discussion of MFI zeolite thin film synthesis. MFI is an important zeolite material that is used in a large number of applications. It also has an extensive synthesis and characterization literature. MFI zeolite is an orthorhombic crystal with the crystal structure formed by 5 member rings that are connected to each

other to form a chain. Each chain is connected with each other through oxygen atoms. MFI is known to have a high Si/Al ratio. There are two types of channels/porosity in MFI, sinusoidal pores with the dimensions of 5.1 Å x 5.5 Å along (100) and a straight channel with the dimensions of 5.3 Å x 5.6 Å along (010) [25]. The structure of MFI is shown in Figure 4.

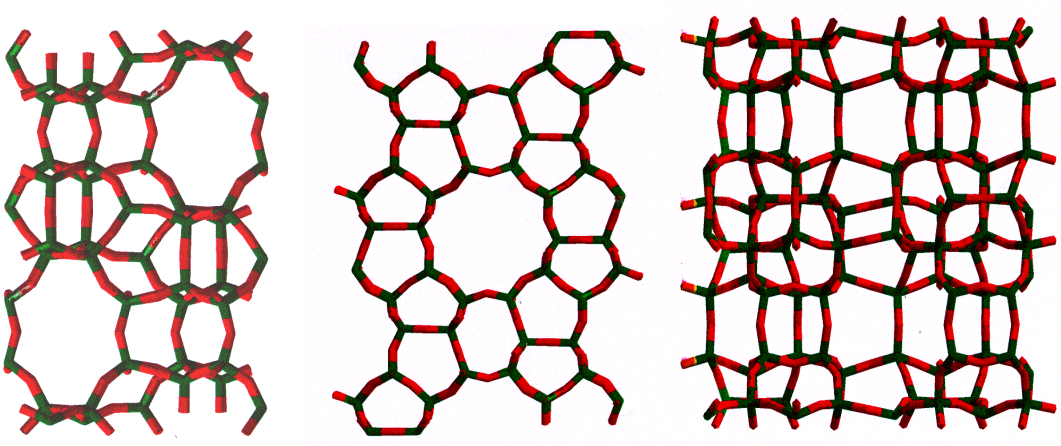

a-direction *b*-direction *c*-direction

Figure 4: Structure of zeolite MFI as viewed down crystallographic a, b, c directions.

2.1.1 Literature Review

The zeolite synthesis method that we use today is based on the pioneering work of Barrer [5, 26]. Zeolite materials are synthesized *via* a hydrothermal process with reagents consisting of a silica source, alumina source, a mineralizing agent (OH^-, ammonium cation), and an organic compound as directing agents. There are different reaction mechanisms proposed in the formation of zeolite particles. Chang and Bell [27] studied the formation of MFI zeolite from Al-free precursors gel. They suggested that the synthesis mechanism of MFI membrane is divided into three steps: (1) the formation of

clathrate like water structure around the template, which usually is tetrapropyl ammonium hydroxide, (2) the substitution of water by silicate in the cages which formed pore network similar to MFI, and (3) repetition of step (1) and (2) form MFI zeolite crystal structure. The current consensus regarding the synthesis mechanism of MFI zeolite is shown in Figure 5.

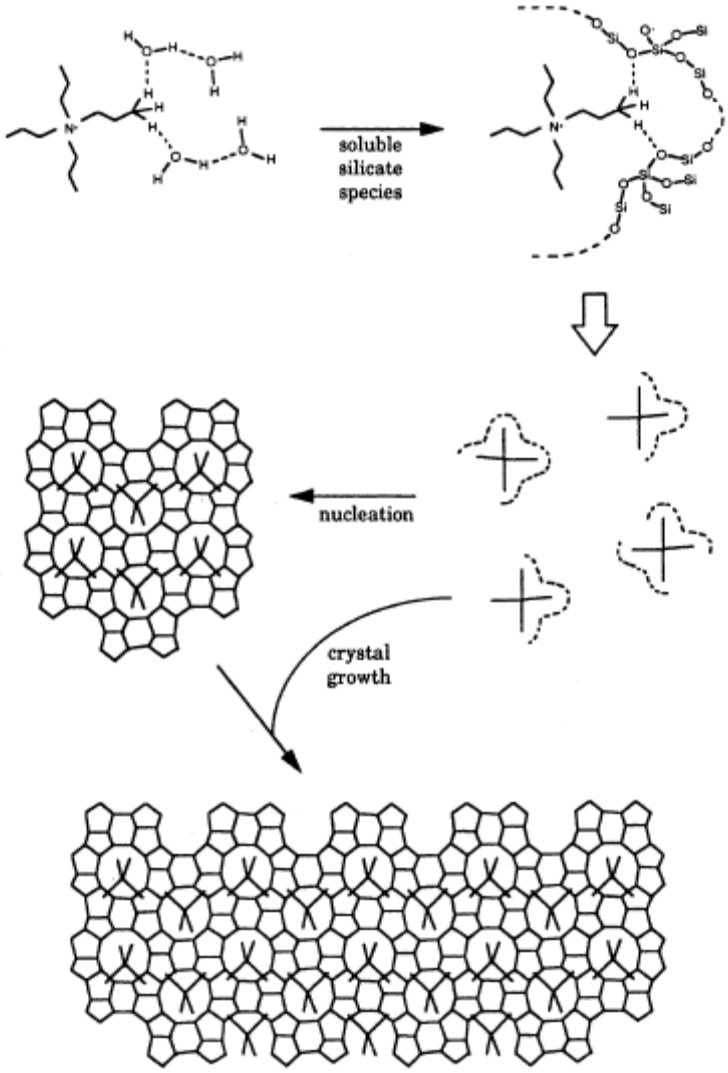

Figure 5: Currently accepted mechanism of zeolite MFI synthesis [28]

Even though the synthesis of zeolite powders has been well studied, the synthesis of zeolite films is relatively new. There are two synthesis methods for zeolite films: (i) *in situ* growth and (ii) seeded (secondary) growth. The *in situ* growth is carried out by introducing the support/substrate directly into the synthesis solution, and the zeolite is allowed to nucleate and crystallize on the substrate under hydrothermal conditions. The zeolite crystal size and thin film orientation depends on the concentration of the nuclei on the substrate. This method is known to usually form a film with the crystals in random orientations; however, Wang and Yan [29] reported that an oriented membrane can be achieved by varying the OH^-/Si ratio in the synthesis solution. The secondary hydrothermal synthesis is performed by first coating a seed layer of zeolite nanoparticles on the substrate. The zeolite seeds serve as the nuclei for subsequent secondary growth of a dense film. The group of Tsapatsis has able to prepare a pure silicate MFI films with a, *b*, and *c* out-of-plane orientations using the secondary hydrothermal method [30-32]. Lai et al [33] reported that the orientation of the MFI zeolite film depends on the zeolite growth environment, which is controlled by manipulating the seed concentration on the substrate, while the film morphology is affected by the synthesis composition and temperature.

2.1.2 Objectives

The primary objective of this chapter is to describe the preparation and characterization of oriented zeolite MFI films which are compatible with thermal transport measurement techniques by 3-omega methods (discussed in Chapter 3). The zeolite synthesis procedure involves the secondary hydrothermal synthesis method. This

chapter also discusses the first synthesis of oriented MFI zeolite films with varying Si/Al ratios. We then describe our thin film characterizations based on Scanning Electron Microscopy (SEM), X-ray Diffraction (XRD), Energy Dispersive X-Ray Spectroscopy (EDS), and Atomic Force Microscopy (AFM), and finally the fabrication of micro-heaters on the film surface for 3-omega measurements.

2.2 Experimental Section

The MFI zeolite films were synthesized using the secondary growth method. Pure-silica MFI zeolite nanoparticles were hydrothermally synthesized from a clear solution of the following molar composition: 1 tetraethylorthosilicate (TEOS, Aldrich): 1 tetrapropylammonium hydroxide (TPAOH, Aldrich): 23 H_2O. The mixture was first hydrolyzed at room temperature under vigorous stirring until a clear solution was obtained. The solution was then filtered, and put in the Teflon lined stainless steel autoclave. The hydrothermal synthesis was done at 90^{o}C for 24 hours under rotation to obtain ~ 100 nm particles. At the end of the reaction, the as-synthesized particles were washed in DI H_2O using a centrifuge for 3 times 20 minutes at 7000 rpm. The particles were dried at 60^{o}C overnight, and then they were calcined at 500^{o}C for 6 hours using a heating rate of 2^{o}C/min. The particles were then dispersed in water for storage.

There are two types of synthesized thin films in this study. The first syntheses method was adapted from Xomeritakis [32] to form a (002)-oriented pure-silica MFI film on silicon wafers. Silicon wafers were cleaned using piranha solution as described in reference [34]. A colloidal suspension of silicalite MFI nanocrystals (~ 100 nm) were

prepared as described above. A 50% suspension in ethanol was filtered, ultrasonicated, and spin-coated (Model 100CB, Brewer Science, Inc.) on the silicon substrate at 3000 rpm for 30 seconds. The coated substrates were dried at 60^{o}C overnight. Silicalite MFI films were then grown in a Teflon-lined stainless steel autoclave by secondary growth of the nanocrystals at 175^{o}C for 48 hours, with a growth solution composition as described elsewhere [32]. The films were rinsed with hot DI water, dried in 60^{o}C overnight, and then polished with SiC paper (Buehler Inc., 1200 and 4000 grit) at 100 rpm for 15 and 35 seconds, respectively. The sample is calcined in air (500°C, 5 hours) to remove the organic tetrapropylammonium ion (TPA^{+}) template, creating an empty nanopore structure. Both calcined and uncalcined MFI films were prepared.

The second type of MFI zeolite film was synthesized in order to obtain a variety of Si/Al oriented MFI membranes (Figure 6). Firstly, the synthesis was completed by following the method described by Ulla for synthesis of zeolite particles of varying Si/Al ratios [35]. A commercially available Porous α-alumina disk (Coorstek) with porosity of 25% was chosen to be the substrate. The substrates were polished with SiC paper (Buehler Inc., 400/800 grit) at 140 rpm for 2 minutes in order to obtain a smooth surface favoring the absorption of MFI nanoparticles. The substrates were washed with DI H_2O to remove any debris, and dried with an N_2 gun. A 50 wt% MFI nanoparticle solution in ethanol was made, ultrasonicated, and filtered to remove a large agglomeration of particles in the solution. The solutions were spun-coated (Model 100CB, Brewer Science, Inc.) on alumina substrate by pipetting 4-5 drops of solution onto the substrate. The substrates were initially spun at low speed of 500 rpm with a ramping rate of 250 rpm for

5 seconds, and then they were spun at higher speed of 3000 rpm and ramping rate of 500 rpm for 40 seconds. The coated substrates were further dried at 60^{o}C for about 1 hour.

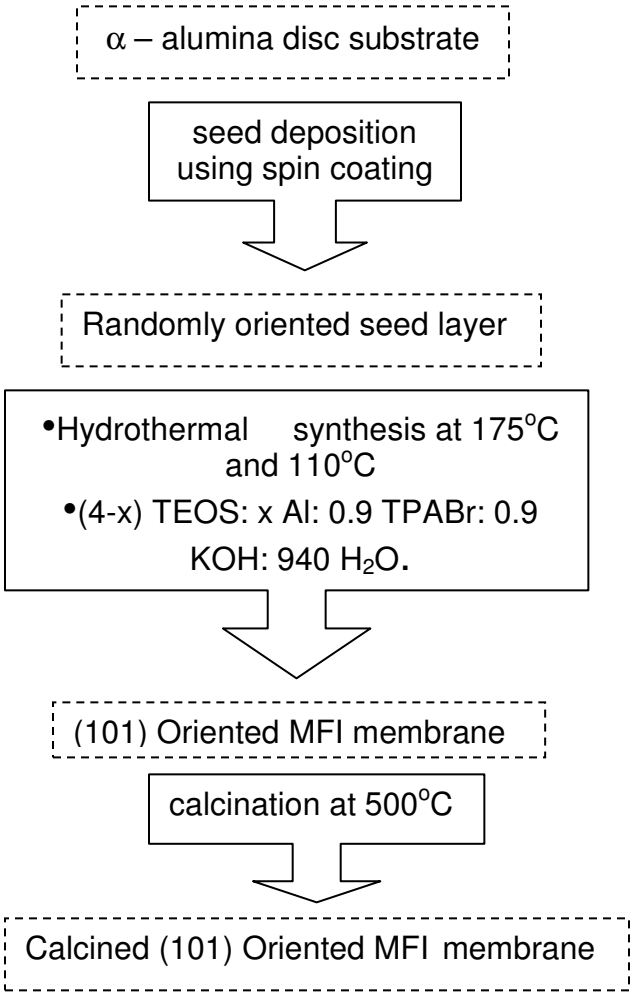

Figure 6: Schematic of oriented zeolite film synthesis by secondary hydrothermal method

The coated substrates were placed at an inclined angle with the seeded side facing downwards in a Teflon-lined stainless steel autoclave for hydrothermal synthesis at

180°C. The secondary growth solutions were contained molar ratios of 1 SiO_2:0.014 Al_2O_3:46 H_2O:0.043 TPABr: 0.13 KOH. The films synthesized using this solution do not have a uniform Si/Al throughout, as be discussed in the next section. Hence, a new hydrothermal synthesis is conducted at 175°C (lower Si/Al ratios) for 48 hours and 140°C (higher Si/Al ratios) for 72 hours. The secondary growth solutions have compositions of (4-*x*) TEOS: *x* Al: 0.9 tetrapropylammonium bromide (TPABr, Aldrich): 0.9 KOH: 940 H_2O. The values of *x* are adjusted according to the desired Si/Al ratio of the films. The potassium aluminate solution was prepared by hydrolyzing aluminum powder in KOH, TPABr, and water solution for one hour. The potassium silicate solution was prepared by mixing TEOS in KOH, TPABr and water solution for one hour. Then both solutions were mixed together. After the reaction ended, the films were rinsed with hot DI water, dried at 60°C for 3 hours, and calcined in air at 500°C for 6 hours with a heating rate of 1°C/min (see Figure 6). The films were then characterized by XRD (PANalytical X'Pert Pro, CuKα) to obtain the film orientation. The films were then polished with SiC papers (Buehler Inc., 400/800, 600/1200, 1000 and 4000 grit) at 100 rpm for 35 seconds each. The films were further polished with alumina polishing suspensions of 0.5 micron, 0.3 micron and 0.05 microns. The film roughnesses were then characterized by Atomic Force Microscopy (AFM). The film thicknesses and compositions were characterized by SEM and EDS (both carried out on a LEO 1550 instrument operating at 10kV).

2.3 Results and Discussion

Figure 7 shows the SEM cross section and top views of a pure-silica MFI film. The facets represent the (101) planes of the crystals [32] and increase the surface

roughness, resulting in a poor quality of microheater deposition. The top view shows the surface of the film with a grain size of 4 µm. Figure 7 shows the membrane after polishing. The thickness was reduced to 20 µm and the surface is considerably smoother, allowing a reliable heater deposition. The MFI crystals in the film have a (002) out-of-plane orientation which was determined by XRD (Figure 8).

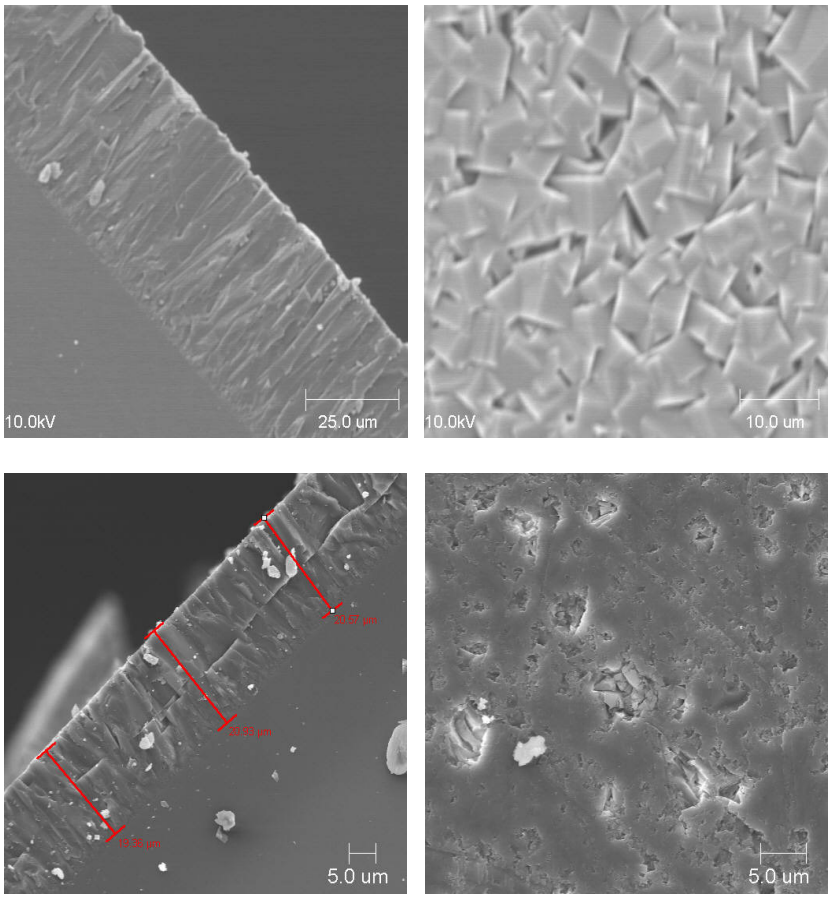

Figure 7: SEM images of (a) cross-section of unpolished pure-silica MFI film, (b) surface morphology of unpolished film, (c) cross-section of polished film, (d) surface morphology of polished film

MFI zeolite films with various Si/Al ratio were first synthesized using a concentrated amount of precursor as suggested by Ulla [35], and the XRD patterns show that the films have a (101) orientation. However, the EDS results (e.g., Table 1) do not show a uniform silicon-to-aluminum ratio throughout the cross section. Hence, these

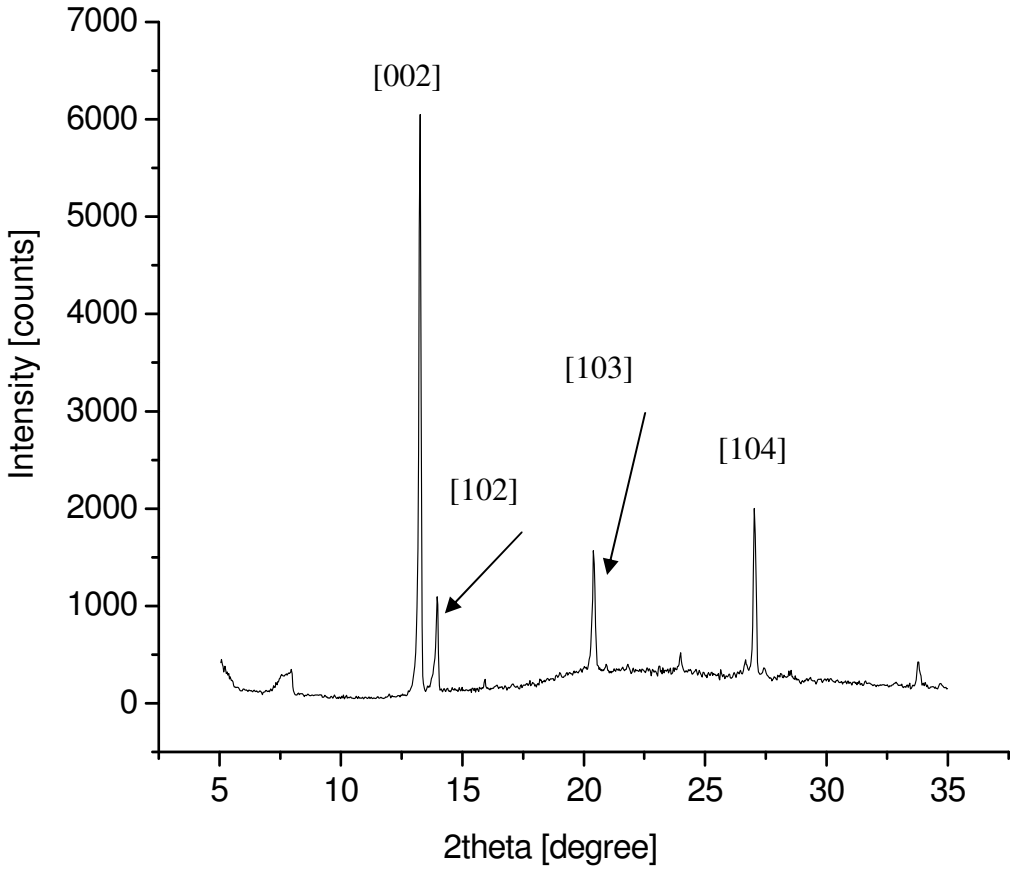

Figure 8: X-Ray Diffraction Pattern of (002) pure-silica MFI oriented film

films cannot be used for studying the structure – property relationships because one cannot extract the correct composition of the membranes. In addition, the morphology of the films (Figure 9) shows a different morphology between a higher resolution and a

lower resolution, thus, one will not be able to extract the correct structure effect on the thermal transport properties mechanism through these materials.

Table 1: Initial EDS results on an aluminosilicate MFI film

spot	Si/Al	Si/K
1	32.07	7.06
2	83.68	46.54
3	108.18	50.91
4	96.57	25.19

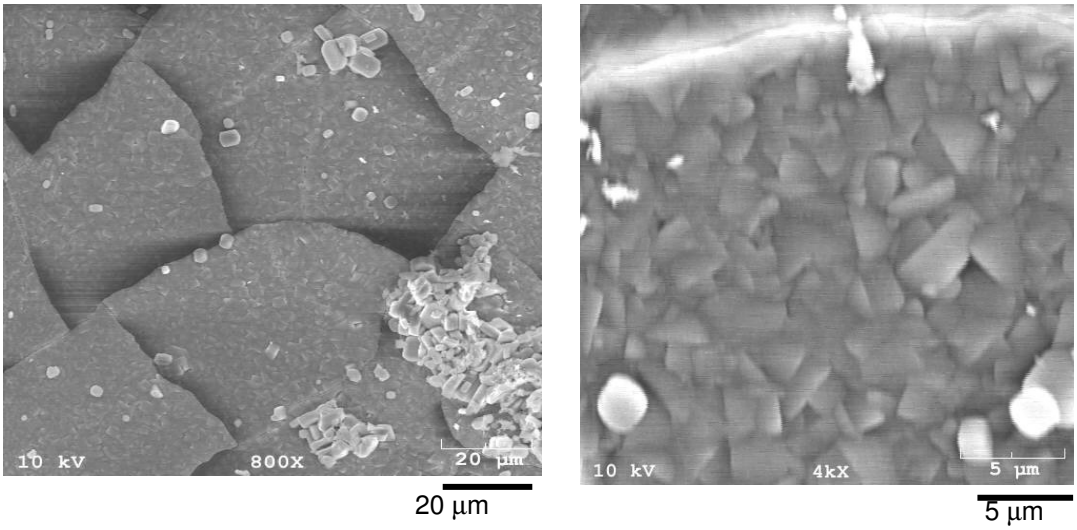

Figure 9: SEM Images of aluminosilicate MFI zeolite film obtained from the initial concentrated synthesis composition

Due to the difficulty of synthesizing high-quality MFI films on silicon wafers using the above method, the second approach using lower concentrations of reactants and

lower growth temperature (as described in Section 2.2) was used to synthesize MFI zeolite films with Si/Al ratios of 26, 36, and 83 in addition to a pure-silica MFI film. The film orientation was determined by XRD (Figure 10). All films showed a constant (101) orientation. The introduction of aluminum into the synthesis changes the crystal growth characteristics, and thus the film orientation, in ways that are poorly understood. Considerable optimization of the synthesis conditions (temperature, composition) was necessary to synthesize several MFI films with varying Si/Al ratios. MFI films with Si/Al ratios below 25 could not be prepared irrespective of the crystal orientation, for reasons that are likely related to the stability of the crystal structure and the alteration of the growth mechanism in the presence of larger amounts of aluminum precursors.

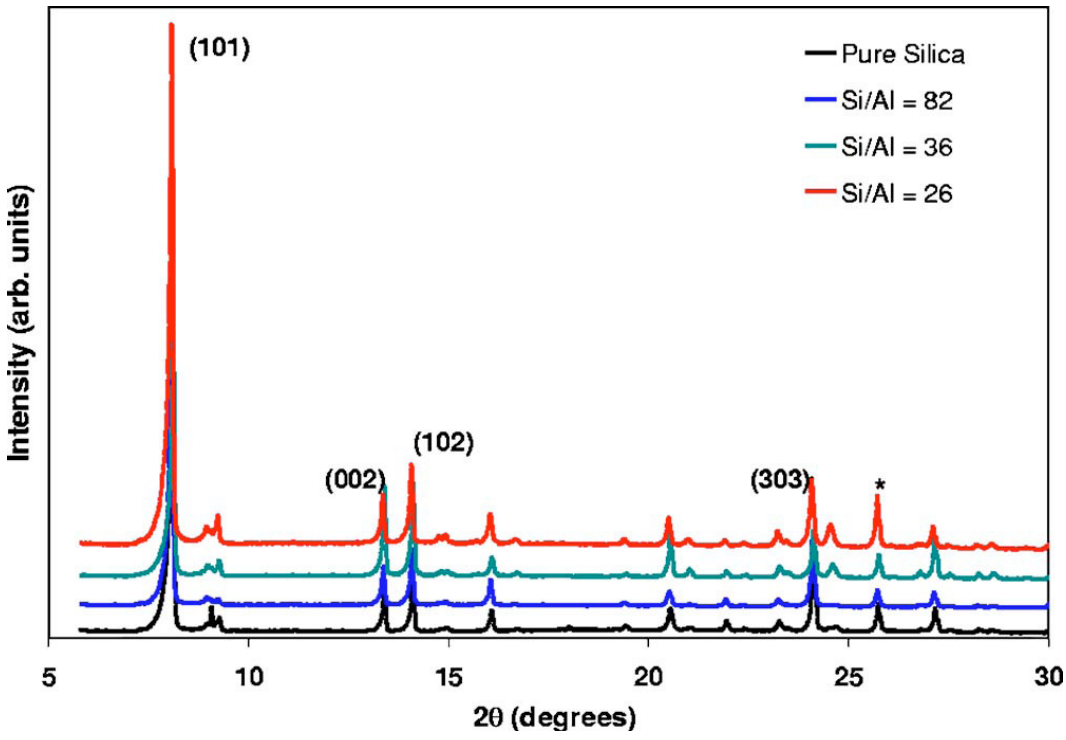

Figure 10: X-ray Diffraction Pattern of MFI films as a function of film composition

Figure 11 shows the SEM top views of a typical film before and after polishing, and the cross-section view of the film after polishing. The polishing step was found to be important for reliable heater deposition prior to 3 omega measurements of thermal conductivity. Table 2 summarizes the obtained Si/Al ratios from EDS, the root-mean-square (rms) roughnesses from AFM, and the Scherrer domain sizes (*vide infra*) obtained from XRD. The EDS results were obtained using an electron beam of 3 μm spot size and were averaged over numerous regions of the membrane cross section to obtain a reliable estimate of the composition. The present MFI films are measured to have Si/Al ratios of ∞, 82, 36, and 26.

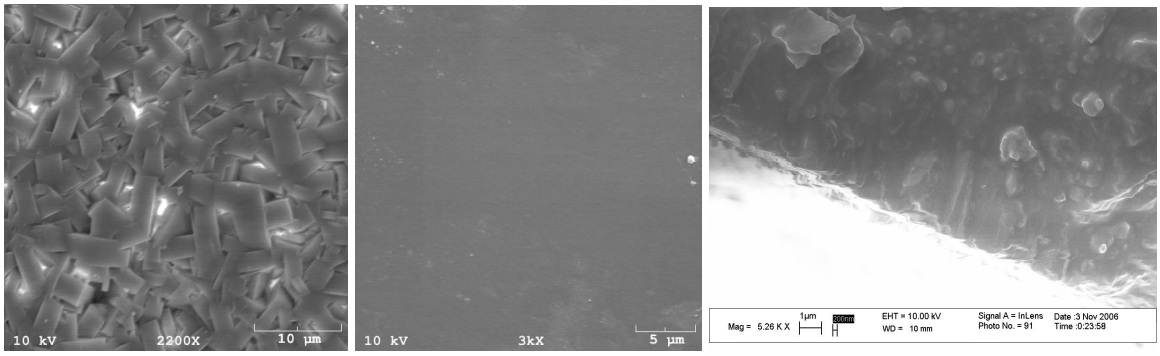

Figure 11: SEM Images of MFI films (a) top view of MFI films, (b) polished surface of MFI films, (c) cross-sectional view of MFI films.

Table 2: Film composition measured by EDS and film roughness measured by AFM

Sample	Synthesis Composition Si/Al	Synthesis Temp. (^{o}C)	EDS results Si/Al	Roughness (Angstrom)	Domain Size (nm)
1	Infinity	140	Infinity	102	97.1
2	100	140	82 $\pm$ 15	65	99.5
3	65	175	36 $\pm$ 6	64	93.7
4	35	175	26 $\pm$ 5	45	92.5

2.4 Conclusion

We have described a thin film preparation method that can be accurately used to make the first accurate measurements of the thermal transport properties of zeolite MFI. Oriented MFI zeolite films with various Si/Al ratio can be obtained and thoroughly characterized for their structure and composition. The incorporation of aluminum favors (101)-oriented films. We also found that minimizing the roughness of the films is critical in order to obtain high quality of thermal conductivity values.

CHAPTER III

MFI ZEOLITE FILMS: THERMAL CONDUCTIVITY MEASUREMENTS AND MODELING

3.1 Introduction and Objectives

The capability of altering the composition of a given zeolite (e.g. by lattice atom substitution or by introducing metal cations and organic molecules into the pores) while maintaining the same framework structure, or conversely the ability to synthesize different framework structures with the same composition, make zeolites extraordinarily versatile materials with interesting structure – function relationships as well as many important applications. There are both experimental difficulties as well as theoretical challenges in measuring and describing thermal transport in complex materials. The experimental difficulties have been discussed in the previous chapters, and have been overcome by us through the synthesis of high-quality zeolite films suitable for accurate thermal transport measurements. The theoretical challenges have been done in collaboration with A. Greenstein (GTME). Detailed calculations of the thermal transport parameters found in this chapter are further discussed in Greenstein's thesis [36].

The thermal transport properties of materials can be described theoretically by solving the generalized Boltzmann phonon transport equation. The relaxation time approach, describing the phonon scattering process, is usually utilized to understand the heat transfer mechanism in the materials [37]. Theoretically, relaxation times can be obtained directly from the Fermi golden rule [38] if full details of the phonon dispersion and mode eigenvectors can be calculated. Difficulties in directly calculating relaxation

times have led to various simplifying assumptions for incorporating the effects of different scattering mechanisms on phonon transport. Good agreement is obtained with experimental data for crystals with only a small number of phonon branches (e.g., Si, Ge, diamond). The thermal transport properties of zeolite materials have been previously determined using similar approach by only considering the acoustic phonon branches [22]. However, this approach is not adequate because the phonon velocity, at higher frequency phonon branches, does not vanish as they behave in the simple materials.

In this chapter, we study the thermal transport properties of MFI zeolite materials that combine systematic variation of zeolite composition, measurements of thermal conductivity using well-intergrown polycrystalline zeolite films, and modeling of thermal transport using a detailed lattice dynamics calculation. We consider the entire phonon branches in the Brilloiun zone, and we are able to obtain an excellent agreement between the heat capacity calculated by our model and the experiment data. We use a highly accurate atomistic force field to calculate the phonon dispersion curves. This study allows separation and analysis of the structural and dynamical factors that influence the thermal conductivity. We chose zeolite MFI as a well-characterized model system because it can be made as a pure SiO_2 material or with different Si/Al ratios (as low as 25). As described in Chapter II, we have prepared oriented MFI films on polished α-alumina substrates by secondary (seeded) growth. In this chapter, we describe experimental thermal conductivity measurements by 3-omega techniques and the modeling of the results to extract physically meaningful transport parameters. We model the thermal conductivity in the framework of the Boltzmann transport equation, with detailed input on phonon

dispersion and specific heat from atomistic lattice dynamic simulations. Detailed consideration of various phonon scattering processes, represented by theoretical expressions with a small number of physically significant fitting parameters, allowed us to elucidate both the effects of aluminum incorporation as well as the relative importance of each scattering mechanism, in determining the temperature and composition dependence of the thermal conductivity.

3.2. Theory

3.2.1 Thermal Transport Theory

In semiconducting and insulating solids, heat is primarily carried by phonons. A phonon represents the quantized vibrational energy of an atom or a group of atoms in the crystal [39]. The bonding of two atoms can be described as a spring, which has a certain spring constant and mass according to the atom types and the bond strength. The atoms can be assumed to have a harmonic oscillation around the minimum energy configuration, with the potential energy represented by a parabolic function (see Figure 12). The combined vibration of many atoms in a lattice can be described in terms of a wave motion [39]. The position of any atom in a monatomic unit cell is described as:

$$x_n = x_o \exp i(nka - \omega t) \tag{3.1}$$

where x is the atom position, a is the lattice parameter, ω is the oscillation frequency, t is time, and k is the wave vector defined as:

$$k = \frac{2\pi}{\lambda} \tag{3.2}$$

According to the number of atoms and interactions in the solid, the total polarization modes of phonons are 3Z in number (Z equals to the number of atoms in a unit cell), of which 3 of the polarization modes are acoustic modes and (3Z-3) of the polarization modes are optical modes (see Figure 12 for diatomic crystal). The fundamentals of phonon vibration and thermal transport in solid crystals have been widely studied [40-42].

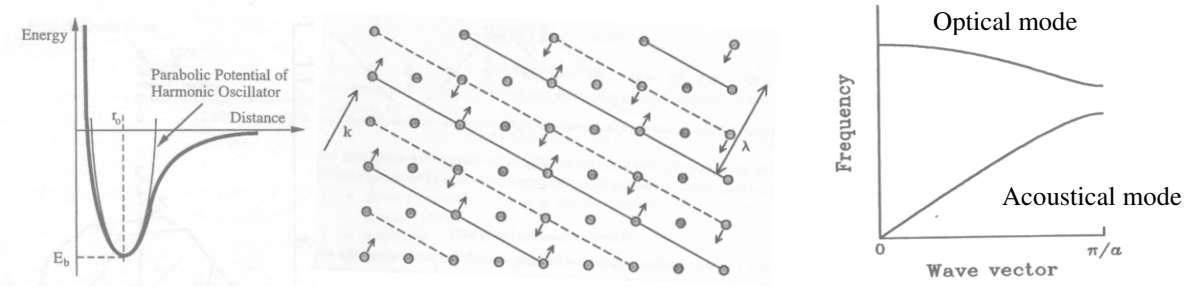

(a) (b) (c)

Figure 12: (a) Energy-distance diagram of a typical chemical bond [39], (b) Diagram of traveling waves in two dimensional monatomic crystal. The arrows indicate the vibration direction [41], (c) Dispersion curve for one dimensional diatomic crystal [41].

Analogous to the quantization of electron and photon energies, the quantized phonon energy can be described as [39]:

$$E_l = \sum_{\vec{k},p} \left(\left\langle n \right\rangle_{\vec{k},p} + \frac{1}{2} \right) \hbar \omega_{\vec{k},p} \tag{3.3}$$

where $\langle n \rangle_{(\vec{k},p)}$ is the phonon distribution function, $\hbar$ is the plank constant, ω is the frequency, k is the wave vector and p is the type of polarization. Energy equal to $\hbar\omega/2$ represents the zero-point energy. The equilibrium phonon distribution at a given temperature T is expressed as [39].

$$\left\langle n(\vec{k}, p) \right\rangle = \frac{1}{\exp\left(\frac{\hbar\omega}{k_B T}\right) - 1}, \tag{3.4}$$

which is a Bose-Einstein distribution. The heat capacity is expressed as [39]:

$$C_l = \frac{\partial E_l}{\partial T} = \sum_p \int \frac{\partial \langle n \rangle_p}{\partial T} \hbar\omega_p D_p(\omega) d\omega \tag{3.5}$$

where and $D_p(\omega)$ is the phonon density of states, which is the number of modes per unit frequency range. As described by Kittel [42], density of states equals to:

$$D(\omega) = \frac{dN}{d\omega} = \frac{VK^2}{2\pi^2}\frac{dK}{d\omega} \tag{3.6}$$

where V is the volume of the solid, and N is the number of vibrational modes.

Therefore, the thermal transfer in semiconductors and insulators is due to the phonon propagation, and the physical limits on heat transport rates in perfect crystals are

determined by the scattering of phonons from each other. There are two types of phonon-phonon scattering. The first is the elastic scattering by the solid defects, boundaries or dislocation; this type of scattering conserves the phonon frequency. The second is the inelastic scattering (Figure 13) (Normal and Umklapp scatterings) which is a scattering between phonons where the phonon frequency changes. These phonon interactions can be described by [39, 41, 42].

$$\begin{aligned} \omega_1 + \omega_2 &= \omega_3 \\ \vec{k}_1 + \vec{k}_2 &= \vec{k}_3 + \vec{G} \end{aligned} \tag{3.7}$$

where $\vec{G}$ is a reciprocal lattice vector. The first equation represents energy conservation while the second equation represents momentum conservation. When $\vec{G}$ equals to zero (momentum is conserved), the scattering process is called Normal scattering, and when $\vec{G}$ is non-zero (momentum is not conserved), the scattering is called Umklapp scattering.

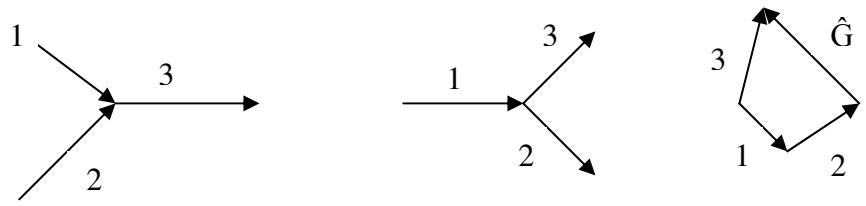

Figure 13: Phonon scattering diagram (left) when the wavevector of the third phonon is the combination of the wavevector of two phonons, (middle) when a phonon splits into two different phonons, (right) when the wavevectors of two phonons are larger than the allowable value.

According to the kinetic theory, the thermal conductivity equals to [39, 41, 42]:

$$k = C_l v l \tag{3.8}$$

where v is the phonon group velocity and ℓ is the phonon mean free path. However, in a non-equilibrium condition, kinetic theory cannot predict the thermal conductivity of the solids; Boltzmann transport equation (BTE) has to be used. In BTE, it is assumed that there exists a phonon distribution function $< n(\vec{k}, p) >$.When there is a temperature gradient in the solid, the phonons will travel by *diffusion* (limited by *scattering* processes*)*, so that at the steady state of heat transfer, the time-change in the phonon distribution function is zero. One of the benefits of using BTE is its capability to solve a large system reasonably quickly [43]. However, the phonon properties, such as dispersion curve, density of states, and relaxation times, have to be determined experimentally and computationally, or predicted by theoretical expressions.

3.2.2 Experimental Techniques - 3ω Method

The 3ω method [44] is chosen to measure the thermal conductivity of zeolite films. A metal line heater, which functions both as a heater and thermometer, is micro-fabricated on to the film surface. The metal line is heated by a sinusoidal current of frequency ω, which results in joule heating and temperature oscillation at frequency of 2ω. These temperature oscillations at 2ω are measured by voltage oscillations at the third harmonic 3ω caused by the temperature-dependent resistance of the metal line. By using

a reference potentiometer, the lock in amplifier is used to subtract the signal from the potentiometer and the signal from the test devices to eliminate unwanted signal noise prior to the measurement of the third harmonic signal. The schematic of the instrumentation is shown in Figure 15. The heat conduction in the solid state is described by the differential equation of 1D heat conduction:

$$\frac{\partial T}{\partial r} = \frac{\alpha}{r}\frac{\partial}{\partial r}\left[r\frac{\partial T}{\partial r} \right] \tag{3.9}$$

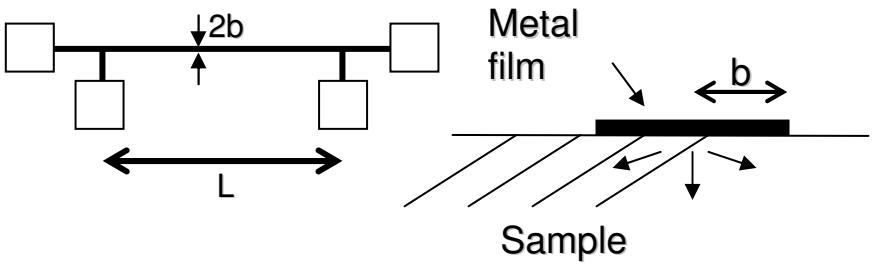

Figure 14: Schematic of heater element and samples, b is the width of the heater and L is the heater length.

The approximate solution of this equation for a given metal line of width 2*b* and length *L* (see Figure 14) yields the following formula correlating the complex amplitude of the temperature oscillations in the metal line and the thermal conductivity of the underlying material [45].

$$\Delta V_{3\omega\_rms} = \frac{V_{rms}^3}{4\pi R^2 Lk}\frac{\partial R}{\partial T}\left[\ln\left(\frac{\alpha}{4\pi f b^2} \right) - \frac{\pi}{2}i + 1.848 \right] \tag{3.10}$$

$$k = \frac{V_{rms}^3}{4\pi R^2 L}\frac{\partial R}{\partial T}\frac{\ln\left(\frac{f_1}{f_2}\right)}{\left(\Delta V_{3\omega\_rms}\right)_2 - \left(\Delta V_{3\omega\_rms}\right)_1} \tag{3.11}$$

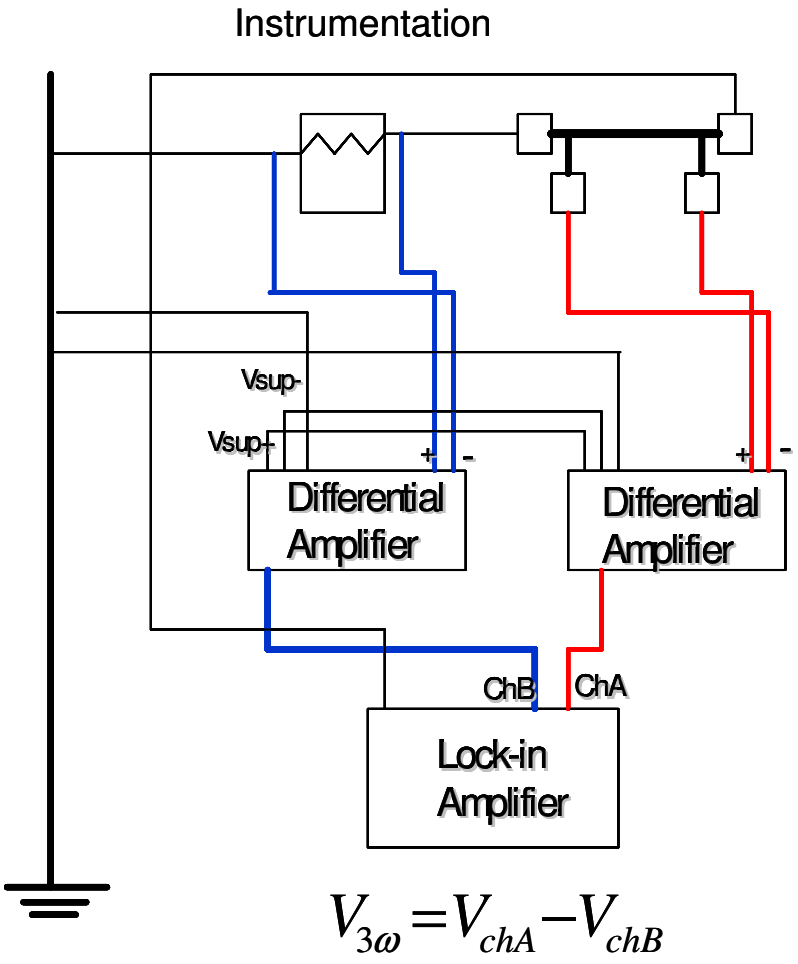

Figure 15: Schematic of 3-omega instrumentation

3.3. Experimental Details

The thermal transport properties of MFI zeolite films were characterized using 3-omega technique [44, 46]. The metal heater was fabricated by evaporation of the titanium and gold. The thickness of titanium layer was 30 nm, and the thickness of gold layer was

160 nm. A 5 Volts AC voltage is applied to the metal heater, and both the in-phase and out of phase response of the third harmonic voltage over a frequency range of 75-2000 Hz were employed to analyze the thermal conductivity of the zeolites films. The measurements were performed at temperature between 150K and 450K in a vacuum cryostat (~10^{-8} torr). The 3-omega voltage responses were obtained and used to calculate the thermal conductivity. The voltage drop was directly related to the temperature response of the metal line which is a function of the thermal properties of the underlying material. The thermal conductivity was deduced by a least squares fit of a 2D analytical solution for a periodic heat source on a multilayer film on substrate system [46]. The thermal conductivity of the substrate was measured in a separate experiment to provide a built in reference for the multilayered system (Figure 16). The substrates were shaped into a disk with a thickness of 1 mm, and a diameter of 1 inch. The heat capacity values of porous α-alumina substrate were calculated from the bulk α-alumina heat capacity by first determining the volume fraction of the substrate. This was achieved by physically measuring the mass and the volume of the substrate and comparing the volume obtained to the volume calculated from the density of bulk α-alumina. Then, the heat capacity values of the porous α-alumina were calculated (Figure 17) from the known heat capacity of bulk α-alumina [47] and heat capacity of air by the following expression.

$$C_{p,porousalumina} = xC_{p,bulkalumina} \tag{3.12}$$

in which x is the volume fraction of the alumina.

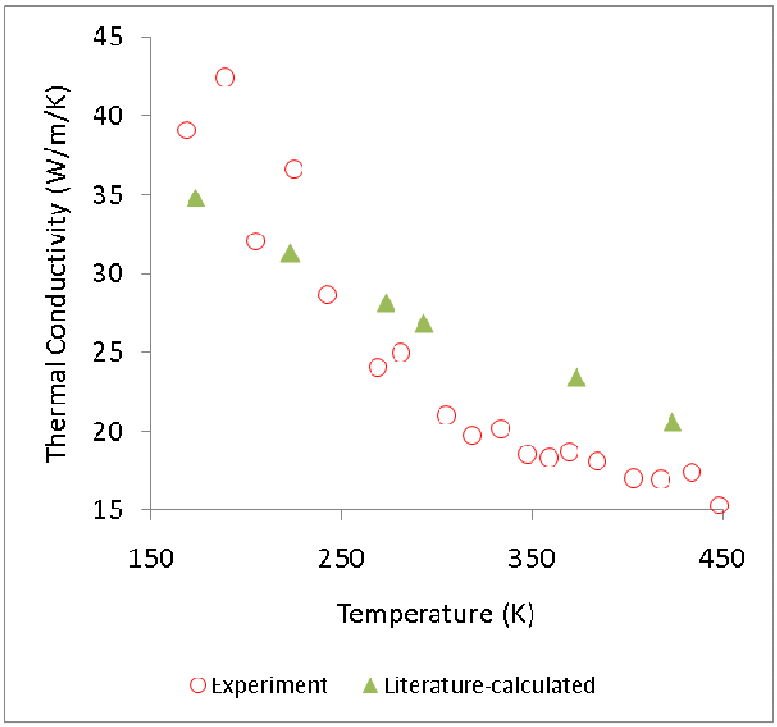

Figure 16: Thermal conductivity of porous alpha-alumina substrate. The experiment values were obtained from 3-omega measurement, the literature-calculated were obtained from [47] and corrected to take into account of the porosity of alumina substrate

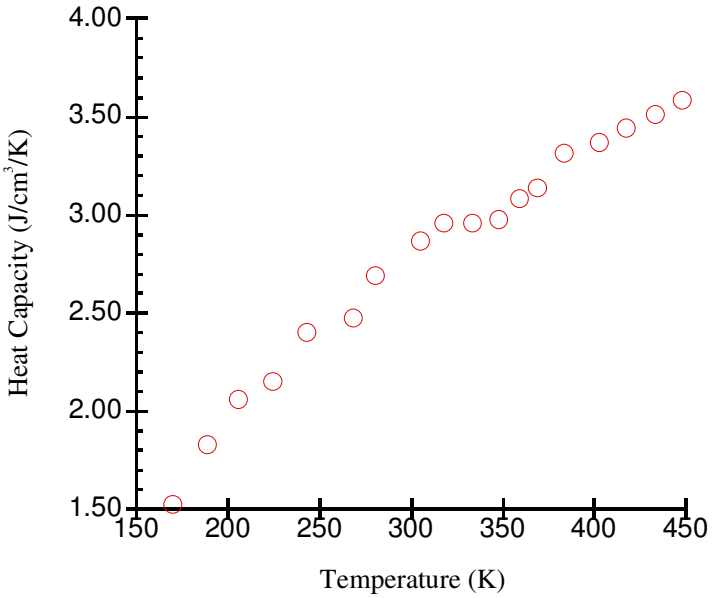

Figure 17: Heat Capacity of porous alpha-alumina substrate.

3.4. Results and Discussion

3.4.1 Thermal Conductivity of (002) oriented MFI zeolite film

The thermal conductivity of (002) oriented MFI film obtained from 3-omega method is shown in Figure 18. The thermal conductivity of (002)-oriented pure-silica MFI film is of the same order of magnitude as that previously reported for zeolites FAU and LTA by MD simulation [7, 8] and by experiment [21, 22]. In addition, the temperature dependence of thermal conductivity appears to be dominated by the strong contribution of specific heat of MFI and not as much by phonon-phonon scattering events in the large zeolite crystals. The single phonon scattering mechanism is fitted to the experiment data by first modeling the specific heat. The specific heat over a wide range of temperatures is shown in the Figure 19. This specific heat is measured experimentally using calorimetry [9].

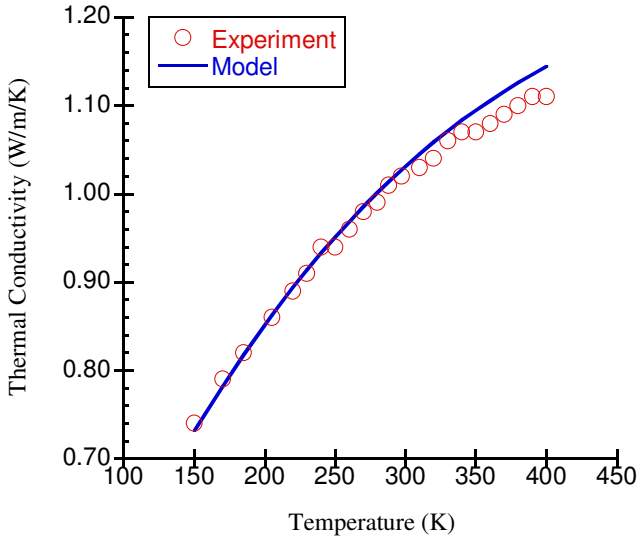

Figure 18: Thermal Conductivity of (002) oriented pure-silica MFI zeolite film

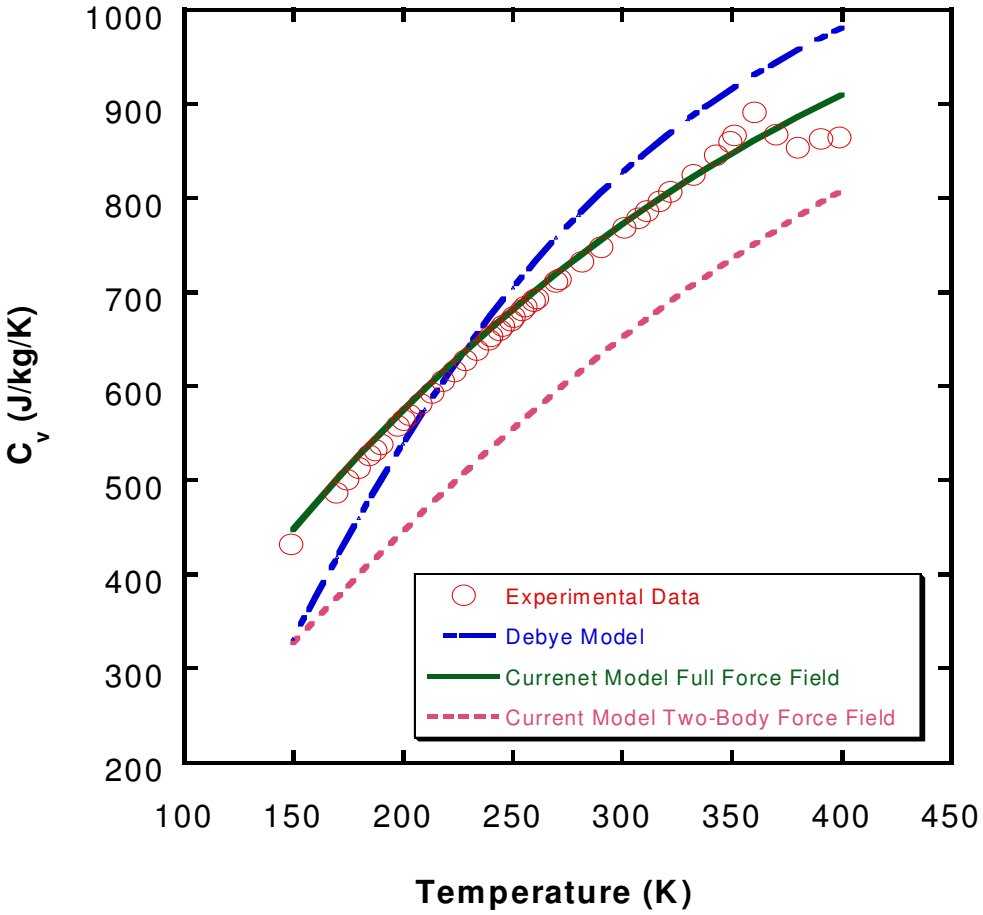

Figure 19: Specific heat of calcined MFI. The experimental data are from Boerio-Goates et al. [9]

Normally, specific heat is modeled via Debye theory, which uses the Debye temperature [48]. The Debye temperature is often obtained by fitting the Debye model to the specific heat data. An attempt to fit the Debye model to MFI (Figure 19) shows that it is unable to predict the specific heat of MFI. The theory makes several assumptions: (1) only the three acoustic phonon branches contribute to the specific heat, (2) the summation over discrete phonon states can be replaced by an integral, (3) the phonon dispersion is

linear and is the same for all polarizations, (4) the dispersion is isotropic, and (5) there is a cutoff frequency represented by the Debye temperature [48]. MFI, an anisotropic orthorhombic crystal, has 288 atoms per unit cell, 864 dispersion branches, and no appreciable band gap between the 3 acoustic and 861 optic modes of nonlinear dispersion. Hence, all the above assumptions but assumption (2) are invalid. A general expression for the specific heat is [49]:

$$C_v = k_B \sum_P \sum_{\vec{K}} x_P(\vec{K})^2 \frac{e^{x_P(\vec{K})}}{(e^{x_P(\vec{K})} - 1)^2} \tag{3.13}$$

$$x_P(\vec{K}) = \left(\frac{\hbar \omega_P(\vec{K})}{k_B T} \right) \tag{3.14}$$

The outer summation is over all 864 polarizations. The inner summation is over all phonon modes or wave vectors in the first Brillouin zone. The assumptions we make are that (i) the wave vectors are continuous, (ii) the dispersion curves are temperature independent, (iii) anharmonicity can be neglected, and (iv) thermal energy storage occurs only in phonons. Replacing the summation over the wave vectors with an integral over the first Brillouin zone results in:

$$C_v = k_B \frac{V}{(2\pi)^3} \sum_{P=1}^{864} \iiint x_P(\vec{K})^2 \frac{e^{x_P(\vec{K})}}{(e^{x_P(\vec{K})} - 1)^2} dV_{BZ} \tag{3.15}$$

To obtain the specific heat with Eq. 3.2, the dispersion curves must be calculated in all directions. The General Utility Lattice Program (GULP) [50] was used to calculate

phonon properties with two different force fields. The first [51] is a two body force field that uses only a Buckingham potential (Eq. 3.17) and Coulomb potential (Eq. 3.16). The second includes a Buckingham potential, a Coulomb potential, a three-body bending term (Eq. 3.18), and a core-shell model (Eq. 3.19) for oxygen polarizability [52]. .

$$E = \tfrac{1}{2}\sum_{i=1}^{N}\sum_{j\neq 1(r_{ij}<Rc)}\left(\frac{q_i q_j\, erfc(\alpha r_{ij})}{r_{ij}} - \frac{q_i q_j\, erfc(\alpha Rc)}{Rc}\right) - \left(\frac{erfc(\alpha Rc)}{2Rc} + \frac{\alpha}{\pi^{1/2}}\right)\sum_{i=1}^{N} q_i^2 \tag{3.16}$$

$$E = \sum_{i>j}\left[A_{ij}\exp(-b_{ij}r_{ij}) - C_{ij}r_{ij}^{-6}\right] \tag{3.17}$$

$$E = k_b(\theta - \theta_o)^2 \tag{3.18}$$

$$E = k(r_{core} - r_{shell})^2 \tag{3.19}$$

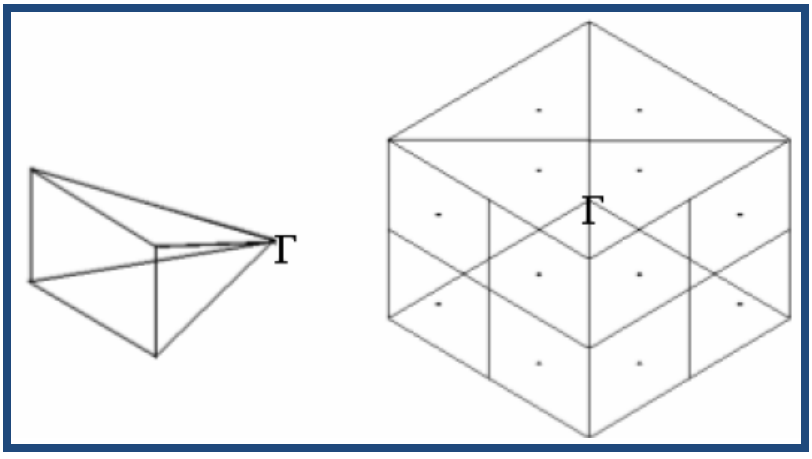

Figure 20: Schematic showing full volume of one of the twelve subsections, and the positive octant of the Brillouin zone of MFI.

A unique discretization scheme is used to integrate over the box-shaped Brillouin zone, which is consistent with the orthorhombic unit cell for MFI. Due to symmetry considerations, the calculation needs to be performed only in the positive octant. In this

scheme, the three orthogonal faces in the positive octant are discretized into 4 subsections, giving a total of 12 subsections. The volume of each subsection is bounded by lines from the edges of the subsection's face on the Brillouin zone surface to the origin. Figure 20 shows a schematic of the Brillouin zone discretization. Dispersion curves are calculated from the origin to the center of each subsection. It is assumed that in a given subsection, each dispersion curve is dependent only on kx, ky, or kz, depending on whether the subsection ends on the kx, ky, or kz plane. The final expression for Cv is:

$$C_v = k_B \frac{V}{(2\pi)^3} \sum_{i=1}^{3} \sum_{S=1}^{4} \sum_{P=1}^{864} \iiint x_P(\vec{K})^2 \frac{e^{x_P(\vec{K})}}{(e^{x_P(\vec{K})} - 1)^2} dV_{BZ} \tag{3.20}$$

$$dV_{BZ1} = \frac{K_x^2}{\cos^3\theta \sin^2\phi} dK_x d\phi d\theta \tag{3.21}$$

$$dV_{BZ2} = \frac{K_y^2}{\sin^3\theta \sin^2\phi} dK_y d\phi d\theta \tag{3.22}$$

$$dV_{BZ3} = \frac{K_z^2}{\cos^3\phi} \sin\phi dK_z d\phi d\theta \tag{3.23}$$

The integration is over the volume elements $dV_{BZ,i}$. The i summation is over the 3 faces and the S summation is for the 4 discretized subsections that end on each face (Eq. 3.20). With appropriate geometric adjustments, this model can be used to predict the heat capacity of many crystalline dielectrics and semiconductors. We first tested the computational technique with silicon, modeled using the well established Stillinger-Weber potential [53]. The details can be found in reference [6]. The model was then

applied to calculate the specific heat of MFI. Figure 19 shows good agreement between the current model and experiment when an accurate force field is used. The only deviation of the current model from experiment is in the region around 350 K. This is most likely due to the well-known displacive second-order phase transition of MFI in this temperature region [54, 55].

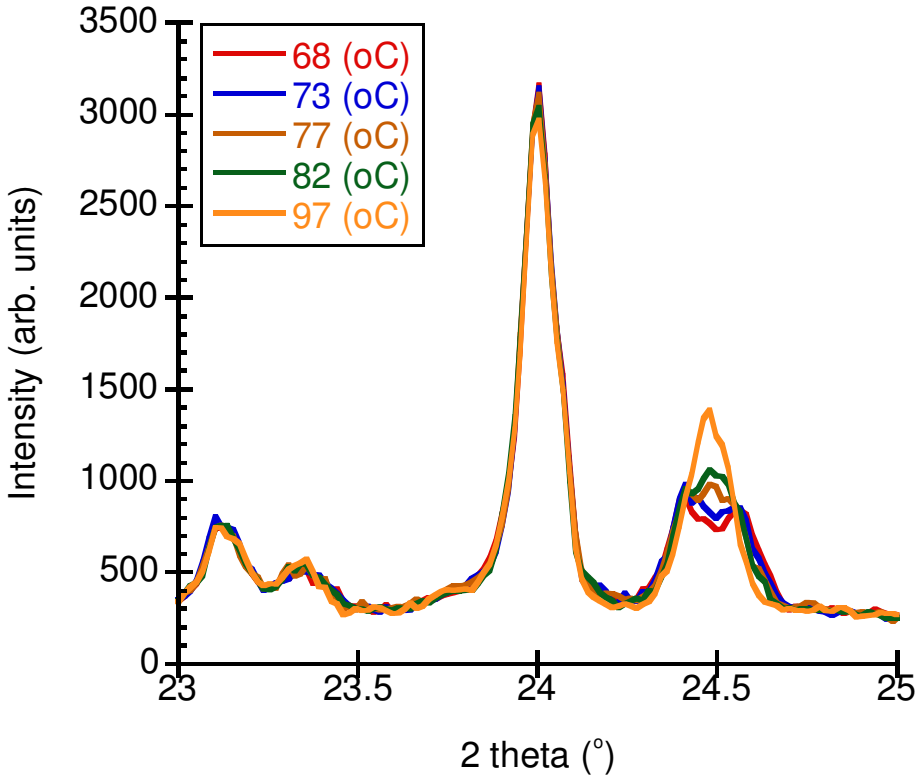

Figure 21: X-ray diffraction pattern of MFI zeolite as a function of temperature. It shows the phase transition at temperature of 350K

In the present study, we have only used the low-temperature crystal structure and hence the effects of the phase transition are not captured. However, this can be addressed

computationally within the framework of free energy minimization techniques, as shown recently [56]. In other words, the free energy of the crystal could first be minimized at each temperature to capture potential phase transitions, before calculating the phonon properties. Neither the two-body force field (even when used with the current model) nor the Debye model produces accurate results. At 400 K the specific heat is still increasing strongly with temperature. This is because the Dulong-Petit law regime is not reached for MFI zeolite structure until 1200–1300 K.The temperature at which the Dulong-Petit limit is reached is directly dependent on the highest phonon frequencies that exist in the solid. The highest phonon frequency in MFI (~30 THz) is nearly double than that observed in silicon.

Using the current theoretical approach, the thermal conductivity can be derived as follows [48]:

$$k_j = \frac{k_B}{(\pi)^3} \sum_{i=1}^{3} \sum_{S=1}^{4} \sum_{P=1}^{864} \iiint x_P(\vec{K})^2 \frac{e^{x_P(\vec{K})}}{(e^{x_P(\vec{K})} - 1)^2} v_{PS,j}^2(K_i) \tau_{PS,j}(K_i) dV_{BZ,i} \qquad (3.24)$$

The index *j* runs over the three principal crystal directions. The conductivity is strongly influenced by phonon velocities (v) and their scattering rates (quantified by phonon relaxation times t). Despite the use of fitted parameters, widely used relaxation time expressions [37, 57] are unable to reproduce the thermal conductivity of MFI, which requires more detailed quantification of the scattering processes. However, we found that in MFI the conductivity can be reproduced by (Eq. 3.5) with a single relaxation time

parameter for all phonons. All other quantities are obtained from the calculation of phonon dispersion. The thermal conductivity result is shown in Figure 18 for the c direction of MFI which corresponds to the out-of-plane orientation of the films studied here.

The value of the fitted relaxation time in our thermal conductivity calculations was 9.2 ps, which is the same order of magnitude as those estimated for quartz near room temperature (250 K) [58] . The estimates in previous works were obtained by decomposition of MD-derived heat flux autocorrelation functions. Therefore, the fitted ‘‘effective’’ relaxation time for MFI appears reasonable. From the dispersion calculations, the average phonon velocity in MFI is estimated at approximately 500 m/s at 300 K. Thus, the low thermal conductivity is due in part to the low phonon velocity. Based on the fitted relaxation time, the phonon mean free path was found to be 4.5 nm at 300 K. Despite its low conductivity, MFI cannot be modeled as an amorphous material. Attempts to model it using a minimum thermal conductivity model, wherein the modal relaxation times were calculated as half the period of the phonons of that mode, resulted in a drastic underestimation of the conductivity.

3.4.2. Thermal Conductivity of (101)-oriented zeolite MFI films

As was tentatively stated earlier, the temperature dependence of thermal conductivity of MFI film appears to be dominated by the strong contribution of specific heat of MFI and not as much by phonon-phonon scattering events in the large zeolite crystals. In this subsection, the temperature dependence and the composition effect of thermal conductivity of MFI film is investigated in detail by measuring the thermal

conductivity of oriented (101) zeolite MFI film with various Si/Al ratios (i.e.26, 36, 86, infinity). Figure 22 shows the thermal conductivity of *(h0l)*-oriented MFI films as a function of Si/Al ratio in the temperature range of 150–450 K. It is clear that the thermal conductivity varies continuously as a function of the aluminum content. Furthermore, the conductivity increases with temperature over the entire range investigated. It was verified through repeated experimentation that the observed behavior was not the result of artifacts arising, e.g., from heater contact resistance.

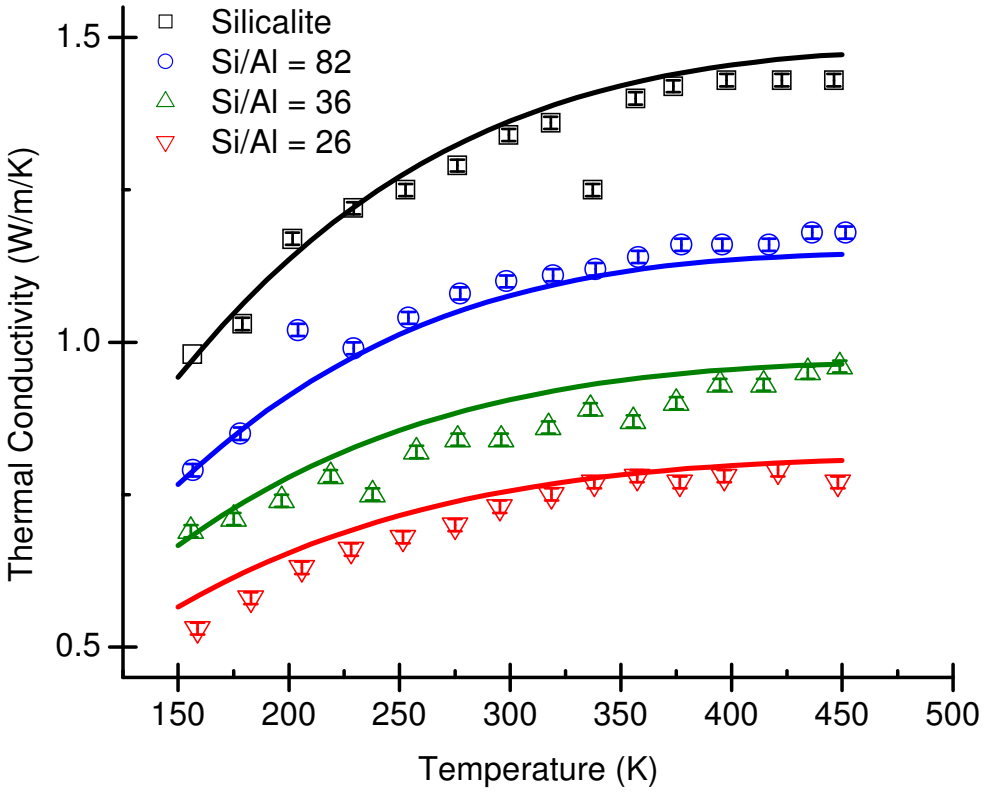

Figure 22: Thermal conductivity of MFI films measured by 3-omega method and fitted by the model for different film compositions

The thermal conductivity is calculated using a relaxation time model with fitted parameters. At first the conductivity is modeled the same way Murashov modeled the conductivity of zeolite 4A [22]. This model makes many assumptions that have been used the in past conductivity models. It assumes that the acoustic dispersions can be treated as linear and isotropic and that the optic modes can be neglected. Despite the use of fitted parameters, the model is unable to reproduce the experimental data. The shortcomings of applying such assumptions to MFI are made evident by the failure of the Debye model to accurately calculate the specific heat [6]. The model that is used to successfully calculate the conductivity is far more rigorous than many previous relaxation time models [59, 60]. The full anisotropic dispersion is calculated across the entire Brillouin zone for all dispersion branches. The General Utility Software Program (GULP) is used to minimize the crystal energy to obtain the atomic coordinates. Then it calculates the eigenvalues of the dynamical matrix to obtain the dispersion relationships.

Before energy minimizations can be done on the aluminosilicate samples, the location of the aluminum atoms and of the Hydrogen atoms, which are needed to maintain charge neutrality, need to be determined. Each Aluminum atom has a hydrogen atom near it; the Hydrogen atom is placed in a pore and is bonded to an Oxygen atom that is bonded to the Aluminum atom. Random Silicon atoms in a single unit cell are replaced by Aluminum atoms, with the constraint that no two Aluminum atoms can be adjacent. This creates two problems the first is related to the system size where because only one unit cell is being considered, only certain Si/Al ratios can be modeled. Secondly, an artificial periodicity is introduced into the crystal. Super cells could be used

to obtain the exact Si/Al ratios but they would be computationally expensive and might make the calculation impractical. Therefore, the dispersions of crystals with Si/Al ratios of 83, 35, and 26 will be approximated as dispersions of crystals with Si/Al ratios of 95, 47, and 31. This will lead to a slight overestimation of phonon velocity but the overestimation is consistent and the goal here is not a perfect calculation but to elucidate trends and understand phonon physics. The artificial periodicity issue should have minimal effects on the model because of the following reasons. An impurity will only affect local bonding because dipole-dipole interactions and the disturbance in the electric field, from the small dipole moment caused by the proton and Aluminum atom, are short ranged. Furthermore, only small amounts of Al are being considered and the unit cell of MFI is fairly large. Therefore, the different impurity sites should be independent of each other. The effect of aluminum configurations is checked by calculating the dispersion for two structures with the same Si/Al ratios but different aluminum atom locations. The resulting dispersions were qualitatively comparable to each other. The very small differences in the curves suggest a weak dependence of the dispersion. Figure 23 and Figure 24 show the sample results of the phonon dispersion and speed for one branch. Similar calculations are done for all 864 branches.

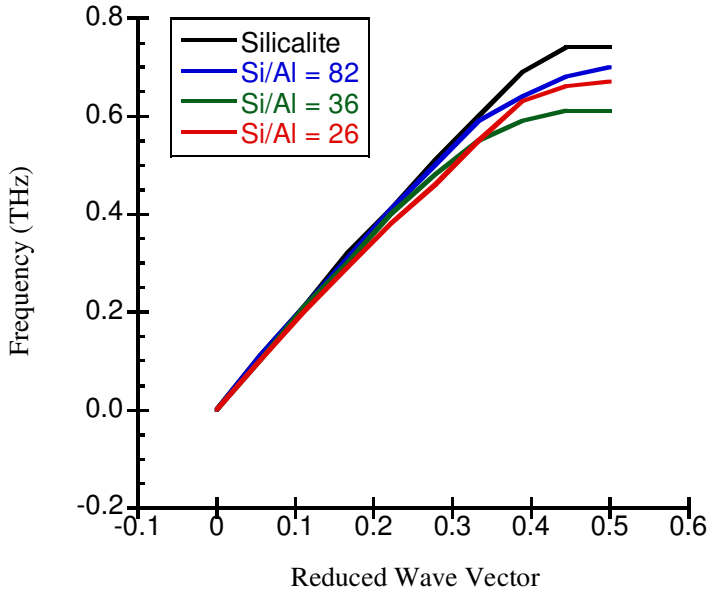

Figure 23: Calculated phonon dispersions of one transverse acoustic branch for different Si/Al ratios in the (1 0 0) direction.

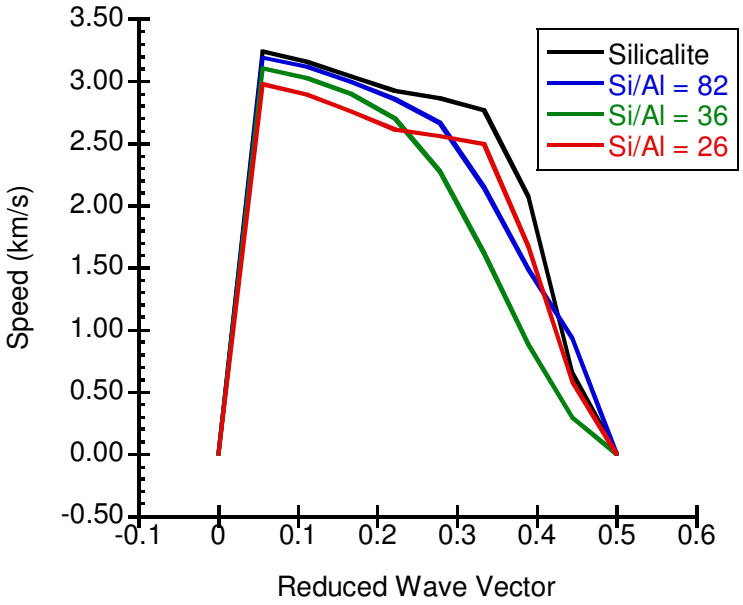

Figure 24: Calculated phonon speeds of one transverse acoustic branch for different Si/Al ratios in the (100) direction

The expression used to calculate conductivity is Eq. 3.24. The integral is over the Brillouin zone the integrand is calculated across a grid through the entire Brillouin zone. The summation is over all polarizations. Velocity is the gradient of the dispersion and is projected onto the direction j, which in this case is the (101) crystallographic direction. The dispersion gradients are calculated by taking the central difference derivative in the x, y, and z directions across the entire Brillouin zone. In theory the relaxation time can be calculated from Fermi's Golden rule [61]. However, this is an extremely expensive calculation for a simple material, for a more complex material the calculation is all but impossible. Some components of τ_j can be estimated from molecular dynamics [7], but defect and boundary scattering cannot be easily accounted for. There have also been molecular dynamics studies that explicitly calculate phonon lifetimes in simple crystals [7, 62], but this approach requires a large number of simulations with varying system sizes in order to adequately sample the Brillouin zone. As a result, fitted parameters and semi-empirical expressions are used to circumvent a direct calculation.

The three different processes considered in the conductivity model are phonon-phonon scattering, boundary scattering, and point defect scattering. Klemens showed that normal processes are unimportant in Quartz [63], so it is assumed that they will be unimportant in MFI. Furthermore, it will be shown that resistive process dominate therefore normal processes will be fairly small. The expression that is used for Umklapp (U) scattering is

$$\tau_U^{-1} = B\omega^2 T e^{-\frac{\theta}{3T}} \tag{3.25}$$

This expression is taken form reference [64]. It is one of the most ubiquitous relaxation time expressions. Here, θ is the Debye temperature and is estimated to be 926 K for MFI. This estimate is obtained by fitting the Debye model of specific heat to the experimental data [6]. However, the calculated results are insensitive to the exact value of the Debye temperature used, for reasons that will become clear during the subsequent analysis of relaxation time behavior. As temperature increases, *U* processes dominate and the conductivity would become inversely proportional to temperature. Debye gave theoretical justification for such trends [65] and many crystals experimentally exhibit such behavior. The calculated Umklapp scattering is the least rigorous part of the calculation and is only approximate. However, later it will be shown that point defect and boundary scattering dominate the conductivity. Therefore, error introduced by inaccuracies in the Umklapp term should be small.

Point defect and boundary scattering are two types of defect scattering. Point defect is the idealized case of an isolated zero dimensional defects in the lattice, while boundary scattering is the idealized case of two dimensional planar defects that divide the lattice into separate domains. The expression used for point defect scattering is [61]

$$\tau_D^{-1} = A\omega^2 g(\omega) \tag{3.26}$$

Here $g(\omega)$ is the phonon density of states. In theory A, which is a constant unique to a given sample, can be calculated ab-inito. In practice this would require far more

structural information about the defects that is practical or even realistic to experimentally ascertain. Therefore A is a fitted constant.

Boundary scattering can be caused by planes of impurities and point defects, stacking faults, grain boundaries, and any other features that may introduce an interface in the material. The expression used for boundary scattering is [61]

$$\tau_B^{-1} = v / l_{eff} \tag{3.27}$$

Like the constant coefficient in the point defect scattering term, the effective distance a phonon travels between planar scattering sites could be estimated theoretically if enough structural information about the defects were known. The shape and size of the domains created by planar defects would need to be known. Furthermore, the reflectivity of the interfaces would need to be known, which is quite an involved problem in itself. Since it is not practical to obtain all this information the effective distance is also treated as a fitted constant. To get an overall relaxation time, all scattering processes are treated as being in parallel and are summed using Matthiessen's rule.

$$\tau_j^{-1} = \tau_U^{-1} + \tau_B^{-1} + \tau_D^{-1} \tag{3.28}$$

There are only three parameters in the fit: A, B, and l_{eff}, of which the last two are constant across all the samples. We ensured that a large parameter space was explored by using a number of initial guesses. A unique best-fit result of high quality was obtained as shown

in Figure 22 and the fitted parameters are summarized in Table 3. The parameter A depends nonlinearly on the Si/Al ratio, since Al atoms can influence phonon transport by scattering from an impurity atom of different mass. Also, the difference in the effective spring constant of Al-O bonds, and local strain fields scatter phonons.

Despite the inclusion of U processes, the thermal conductivity of MFI increases with temperature, implying that other scattering processes as well as specific heat effects dominate the temperature dependence. We found that the boundary scattering term (with a fitted l_{eff} of 4.8 nm) makes by far the strongest contribution of the three phonon scattering mechanisms and hence, limits the absolute value of the thermal conductivity. The obtained value of *l*eff is worthy of more detailed discussion. Several authors report the existence of sub-100-nm domains in zeolite crystals [66, 67]. An upper limit on the domain size is estimated from XRD as (100 nm) (Table 3) by the Scherrer relation [68] which uses the full width at half maximum of the XRD peaks. However, the Scherrer domain size (100 nm) is much larger than the fitted l_{eff} and is unlikely to limit the propagation of phonons at nanometer length scales. Furthermore, the MFI structure is inherently free of pore stacking faults [25, 69] that might also act as phonon scattering boundaries. The high quality of the obtained fit strongly implies that the temperature-independent boundary-like scattering mechanism arises from the interaction of the lattice vibrations with the pore network, which disrupts long-range lattice vibrations. The periodicity of the pore structure in MFI is about 1.5 nm and the crystallographic pore size is about 0.9 nm [25, 69]. Heat carriers would thus have a mean free path that is determined by the length scale of the pore network. From the point of view of real-space

visualization of thermal transport (as opposed to the present reciprocal-space approach), the presence of nanoscale voids would impede the atom-to-atom transfer of heat energy at the surfaces of these voids, since this heat energy must be either reflected back from the void/pore or be channeled around it. Very recently, similar arguments (based upon the results of molecular dynamics simulations) have been advanced to qualitatively explain the thermal conductivity of nanoporous metal-organic frameworks [70].

Table 3: Fitted phonon scattering model parameters for MFI films. Umklapp parameter *B* and effective domain size l_{eff} are held constant across all the samples whereas *A* varies with Al content.

Si/Al ratio	A (10^{-31} s/rad^2)	B (10^{-21} s/K rad^2)	l_{eff} (nm)	Scherrer domain size (nm)
∞	5.7 $\pm$ 0.1	7.4 $\pm$ 0.1	4.8 $\pm$ 0.1	97 $\pm$ 2
82	6.4 $\pm$ 0.1	7.4 $\pm$ 0.1	4.8 $\pm$ 0.1	100 $\pm$ 2
36	45.2 $\pm$ 0.1	7.4 $\pm$ 0.1	4.8 $\pm$ 0.1	94 $\pm$ 2
26	85.2 $\pm$ 0.1	7.4 $\pm$ 0.1	4.8 $\pm$ 0.1	93 $\pm$ 2

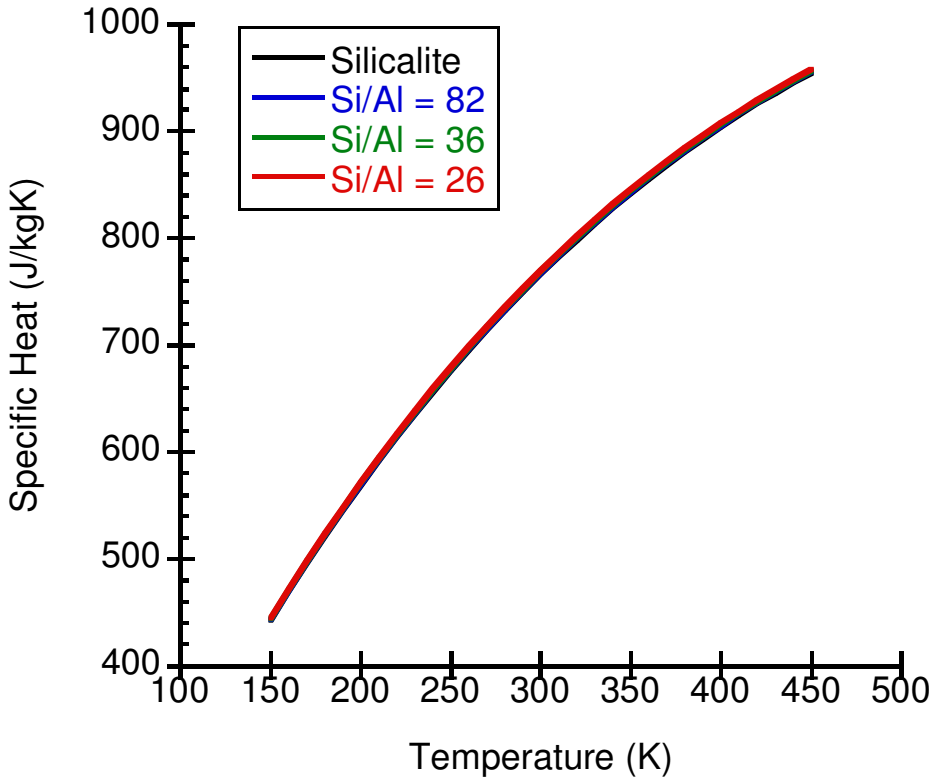

Figure 25: Specific heat of (101) oriented MFI films with various Si/Al ratios as a function of temperature

The temperature-independence of the main phonon scattering mechanism in MFI also explains the unusual (viz. monotonically increasing) temperature dependence of the conductivity, which is well described by the increase in specific heat with increasing temperature (also see Figure 25 and the following discussion). We note that the Umklapp relaxation time expression (Eq. 3.25) is the most rigorous one available from previous theoretical efforts, but is still based on assumptions that may not be perfectly valid for MFI. Future work could focus on developing a general Umklapp term valid for all

phonon branches, which could then allow a more quantitatively accurate estimate of the relative importance of boundary and Umklapp effects on phonon transport in complex crystals.

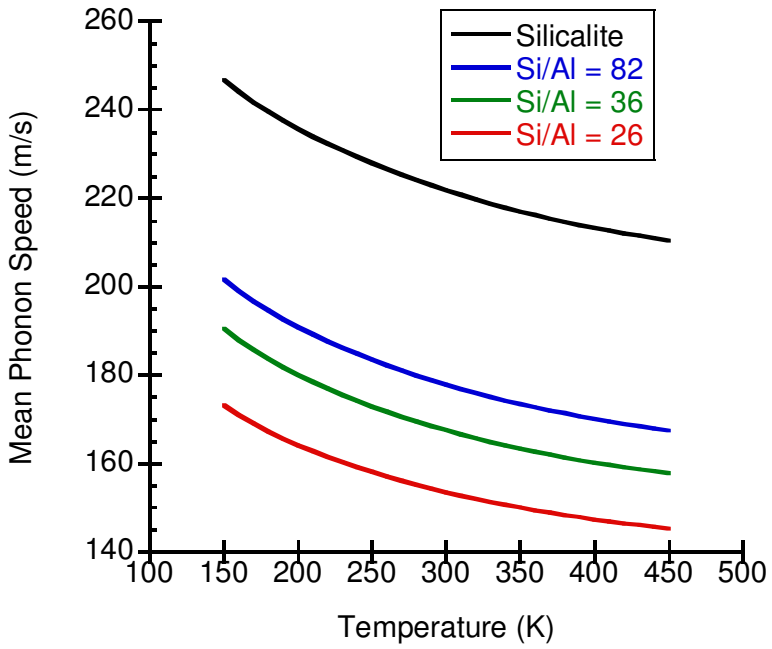

Figure 26: Phonon Mean Speed calculated using specific heat mode as the weighting factors.

With the upper limit being defined by boundary scattering, Al incorporation can effectively suppress the conductivity as seen from the rapid increase in the value of the parameter *A* with increasing Al content. Our approach allows us to determine whether this is due to decreased specific heat, decreased phonon velocity, or increased point defect scattering. The calculated specific heat (Figure 25) changes negligibly with increasing Al content, whereas the mean phonon velocity (Figure 27 and Figure 27) changes significantly. These results may seem surprising because both quantities are

calculated directly from the dispersion curves. However, the modal specific heats are fairly insensitive to small/moderate amounts of Al because phonon states with energies much lower than *kbT* all have the same specific heat and states with energies much higher than *kbT* do not contribute as much to the specific heat.

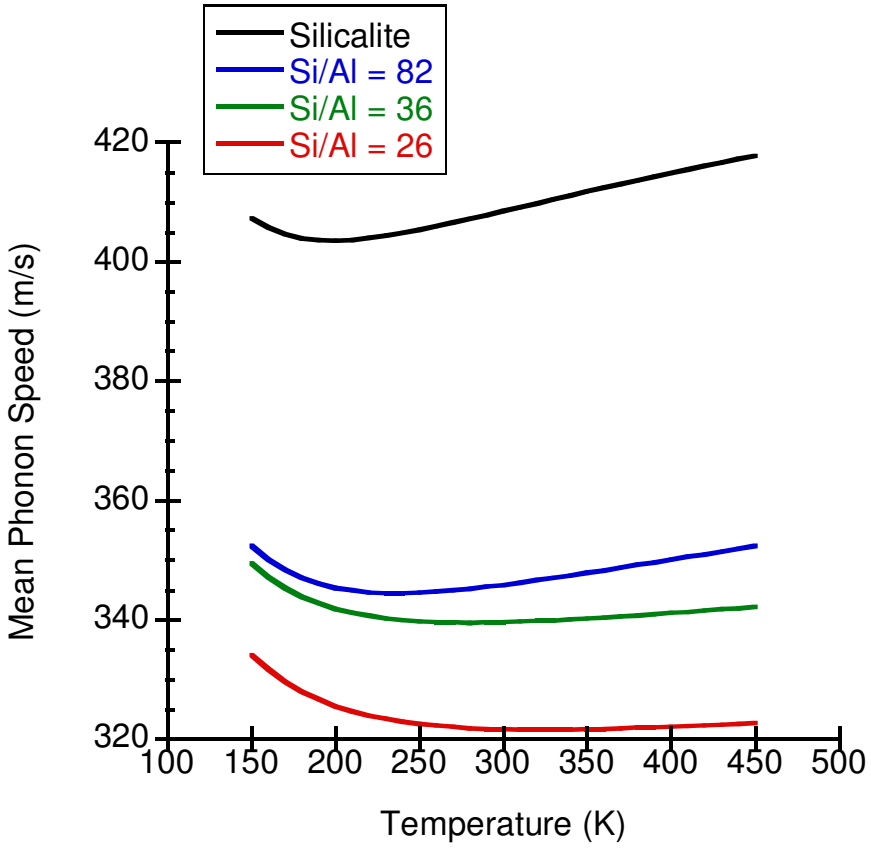

Figure 27: Mean Phonon Speed calculated using the mode thermal conductivities as weighting functions

The mean phonon velocity is calculated by taking a weighted average of the modal velocities of all phonon states. It is calculated with the modal thermal conductivity as weighting function (Figure 27). The mean phonon velocity decreases significantly with increasing aluminum content because aluminum has a smaller charge than silicon, so the

aluminum-oxygen bond is softer than the silicon-oxygen bond. The average speed initially decreases with increasing temperature, because phonon branches with higher frequencies start contributing to the specific heat and these phonon branches tend to have smaller group velocities. The phonon speed starts to increase at higher temperatures because the Umklapp scattering term becomes stronger and it scatters high-frequency, low velocity phonons more strongly than the faster, lower frequency phonons. The results of Figure 28 show that the presence of Al atoms slow the mean phonon velocity by about 25% from pure-silica MFI to the sample with Si/Al=26. However, the observed decrease in thermal conductivity (Figure 22) is also due to increased point defect scattering. We note from Table 3 that the point defect scattering parameter *A* is negligible for the pure-SiO_2 sample (but not zero since there is still a small concentration of defects such as missing Si atoms) [25], and that it increases sharply with Al content to an extent that defect scattering makes a significant contribution to the drop in conductivity at higher Al contents. It is important to mention that the effect of Al incorporation is stronger than that expected simply from the "isotope" effect (i.e., substitution of Si with Al, which has a slightly different atomic mass). The Al-O bonds are softer than the Si-O bonds and the resulting local strain would significantly impede the transfer of heat energy (i.e., serve as localized phonon scatterers in reciprocal space) in addition to slowing the mean phonon velocity. This phenomenon has also been visualized in real-space for other aluminosilicate materials by molecular dynamics simulations [7]

3.5. Conclusions

This chapter has presented a combined experimental, computational, and theoretical approach that leads to some new findings regarding the mechanisms of phonon transport in nanoporous materials. Combining 3-omega measurements with energy-dispersive x-ray analysis of the film composition, we obtained a first set of comprehensive data on thermal transport in MFI as a function of temperature and composition. The developed model, which incorporates information from detailed atomistic lattice dynamics calculations, well describes the observed behavior and strongly suggests that the main phonon scattering mechanism limiting the thermal conductivity of nanoporous crystals such as MFI is the boundary-like scattering from the pore network. We also find that Al incorporation significantly suppresses the thermal conductivity due to a combination of phonon slowing and localized phonon scattering, and not due to specific heat or isotope scattering effects. It is important to emphasize that the present approach, although approximate in the handling of the phonon scattering, still represents a considerable advance in measuring and modeling the thermal conductivity of zeolite materials. The synthesis of polycrystalline thin films with controlled compositional variation, thermal property measurements on these films and the current modeling approach together have potential to form a robust platform for understanding thermal transport properties in complex crystals and separating the contributions from different scattering processes. The important roles of boundary and defect scattering, as illustrated here, also imply that the thermal conductivity of these complex crystals can be tuned by exploiting not only the composition but also the pore structure, e.g., by the inclusion of molecular species in the pores.

CHAPTER IV

EFFECTS OF NON-FRAMEWORK METAL CATIONS ON THE THERMAL TRANSPORT PROPERTIES OF ZEOLITE LTA THIN FILM

4.1 Introduction and Objectives

Having employed zeolite MFI as an excellent model system to study the effects of changes in the framework composition on the thermal conductivity of zeolites, we now investigate the effects of the non-framework cations. MFI is not a good model system for this investigation since only limited numbers of aluminum atoms (and hence charge-balancing metal cations) can be introduced. Rather, we choose Zeolite A (LTA) as a model to study the non-framework cation effects on the thermal transport properties while keeping the structure and composition of the zeolite framework constant.

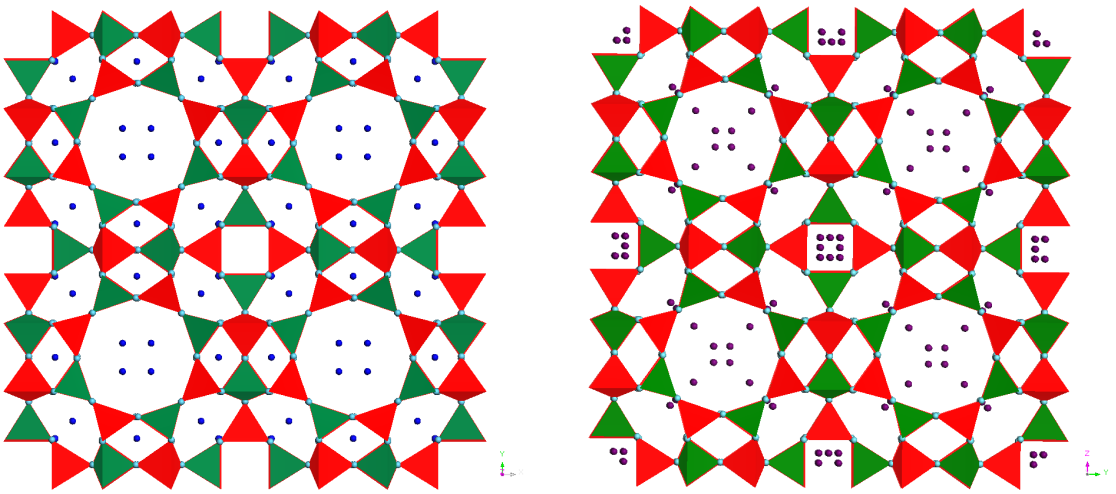

Figure 28: The crystal structures of (a) dehydrate sodium LTA [71] , and (b) dehydrated potassium exchanged LTA [72] . The structures are solved from their correspondence X-Ray Diffraction pattern

LTA Figure 28 was the first zeolite to be synthesized. Its structure is well studied [71-87] LTA is face-centered-cubic (FCC), and crystallizes in $Fm\bar{3}c$ space group at room temperature. It has been previously studied that the structure of LTA zeolite changes via dehydration and heating [71, 73, 80]. LTA structure is built by connecting two sodalite cages via oxygen on the 4 member ring face. It has a unit cell parameter of 24.61 Å. The framework of LTA has a composition of Si/Al = 1, and hence the silicon and aluminum arrangement in the framework is completely alternated to obey the Loewenstein's rule [88]. Aluminum has a +3 charge, thus LTA framework needs to be balance by an extra non-framework cation, to achieve charge neutrality. LTA zeolite is chosen because the effect of the non-framework cations will be much more apparent in this material than a high Si/Al ratio zeolite such as MFI. A unit cell of LTA contains one large cage, (α-cage) with a diameter of 11.4 Å, which is located in the center of its cube, and a small cage (β-cage) with diameter of 6.6 Å at each corner of its cube. Each face of the cube has an eight member ring on the center, a six member ring at the boundary between α and β cages. Two β cages are connected via a double 4 membered ring. Thus in one unit cell, there are three 8-membered rings, eight 6-membered rings, and twelve 4 membered rings, and only the 8 membered rings are shared with neighboring cell.

There are three kinds of sites available for cation exchange [71, 77, 78, 82, 84, 87, 89, 90]. First, α-site, which is located near the center of the eight member ring, β-site, which is located near the center of 6 member ring, and γ site which is located near the center of the 4 member ring. In most of the cases, γ-site has the weakest affinity for

cations, and β-site has the highest affinity for cations [81, 84, 86, 87]. The location of the non-framework cations in the LTA zeolite depends on the type of the cations. We focus on three types of cations, Na^{+}, K^{+}, and Ca^{+2}. In a full exchanged of sodium LTA, there resides 12 sodium ions, which three of the ions are located in α sites, eight ions are located in β sites, and one ion is located in the γ sites [87]. The same arrangement is observed for K-LTA. For Ca-LTA, four of Ca cations reside in the β-sites, 1 cation resides in the sodalite cage, and 1 cation resides in the α-sites [91]. In addition, LTA zeolite doped with alkali metals has been widely studied because of its physical properties. The changes and the movement of cations and the interaction between the non-framework and framework cations lead to interesting magnetic, optical, electrical and dielectric properties of zeolite materials [90, 92-110] .In this chapter, we study the thermal transport properties of LTA zeolite materials by combining systematic variation of non-framework cations composition and measurements of thermal conductivity using well-intergrown polycrystalline zeolite films. The results of these measurements will be critical in developing modeling approaches for understanding the effect of extraframework cations on thermal transport by methodologies related to those developed earlier for MFI**.**

4.2. Experimental Section

4.2.1. Synthesis and Ion Exchange of LTA Zeolite films

The synthesis of a continuous LTA zeolite film is more difficult than that of MFI zeolite because the high aluminum content inhibits the crystallization process. The

synthesis conditions were manipulated extensively in order to finally obtain a continous LTA zeolite film. The LTA zeolite nanoparticles are prepared from a clear solution with a composition of 4.1 $(TMA)_2O$: 0.35 Na_2O: 1 Al_2O_3: 3.4 SiO_2: 239 H_2O, as adapted from Boudreau et.al [34]. The tetrametylammonium hydroxide (25%) solution was purchased from Sigma Aldrich. Aluminum powder, microsphere (99%) and Ludox HS-40 colloidal silica were purchased from Sigma Aldrich. The sodium hydroxide powder was purchased from Fisher Scientific. The chemicals were mixed together at once to obtain a clear solution, and the solution was then hydrothermally synthesized at 90^oC for 16 hours under rotation. The LTA sols were washed three times by repeated centrifugation, and they were diluted in water for storage.

LTA zeolite films were prepared using the secondary hydrothermal method. The clear synthesis solution was composed of 4.1 $(TMA)_2O$: 0.36 Na_2O: 1 Al_2O_3: 4.4 SiO_2: 706.2 H_2O. 50 g/lt of zeolite seeds in ethanol was spin-coated on the alumina substrate. The substrate was dried at room temperature for 4 hours. The synthesis mixture was hydrolyzed at room temperature to achieve a clear solution. The coated substrate was placed in the synthesis solution with the coated side facing downward. The hydrothermal synthesis was performed at 110^oC for 3 days. The films were then washed with warm water, and they were dried at 60^oC for 6 hours. The films were then calcined at 500^oC for 8 hours with a heating rate of 1^oC/hour. This process was repeated twice in order to obtain a thicker LTA zeolite film. After, the films were obtained; the films were polished with SiC paper (Buehler Inc., 600/1200, 1000 and 4000 grit) at 100 rpm for 20 seconds each. The films were then polished with alumina polishing suspension of 0.5 micron, 0.3

micron and 0.05 microns. Ion exchange of the as-synthesized sodium-containing films with potassium or calcium ions, was performed by suspending the films vertically in 0.1 M salt solutions containing KCl or $CaCl_2$ at 70°C. This process was repeated twice, and each time a fresh solution was used, the films were first washed with warm water to remove any excess chloride or salt on the surface. The schematic of the synthesis and ion-exchange process is shown in Figure 29.

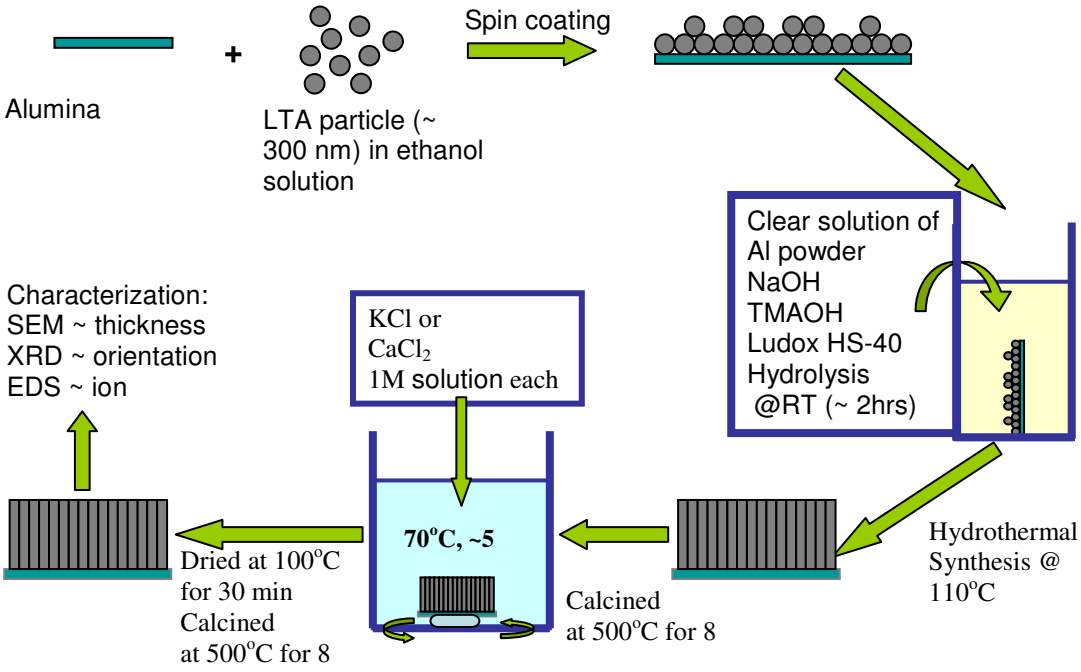

Figure 29: Schematic of LTA zeolite film synthesis by secondary hydrothermal method

4.2.2. Thin Film Characterization

The films were characterized by XRD (PANalytical X'Pert Pro, CuKα) to verify the formation of zeolite A films. The film roughnesses were characterized by AFM. The film morphology, thicknesses, and compositions were characterized by SEM and EDS.

4.2.3. Thermal Conductivity Measurements

The thermal conductivity is measured using 3-omega method, as previously discussed in Chapter III. In measuring the thermal conductivity of LTA zeolite, the zeolite film was first heated under vacuum to 450K and held overnight. This step is necessary to ensure the complete dehydration of LTA, which is a hydrophilic material. This procedure will also ensure that the thermal conductivity measurement was conducted on the cubic crystal of LTA. It was reported [73] that although the crystal structure of LTA zeolite initially changes upon evacuation and heating, the fully dehydrated structure returns to cubic and does not change upon further heating or cooling until rehydrated.

4.3. Results and Discussion

The LTA crystals in the film have a (200) out-of-plane orientation as determined by XRD (Figure 30). Figure 31 shows the SEM cross section and top views. As expected, the morphology of the films does not change upon ion exchange. The thickness of the LTA membrane is 10 μm after 6 days of hydrothermal synthesis. These films are thicker than the previously reported LTA films. This can be due to the higher synthesis temperature used in this study.

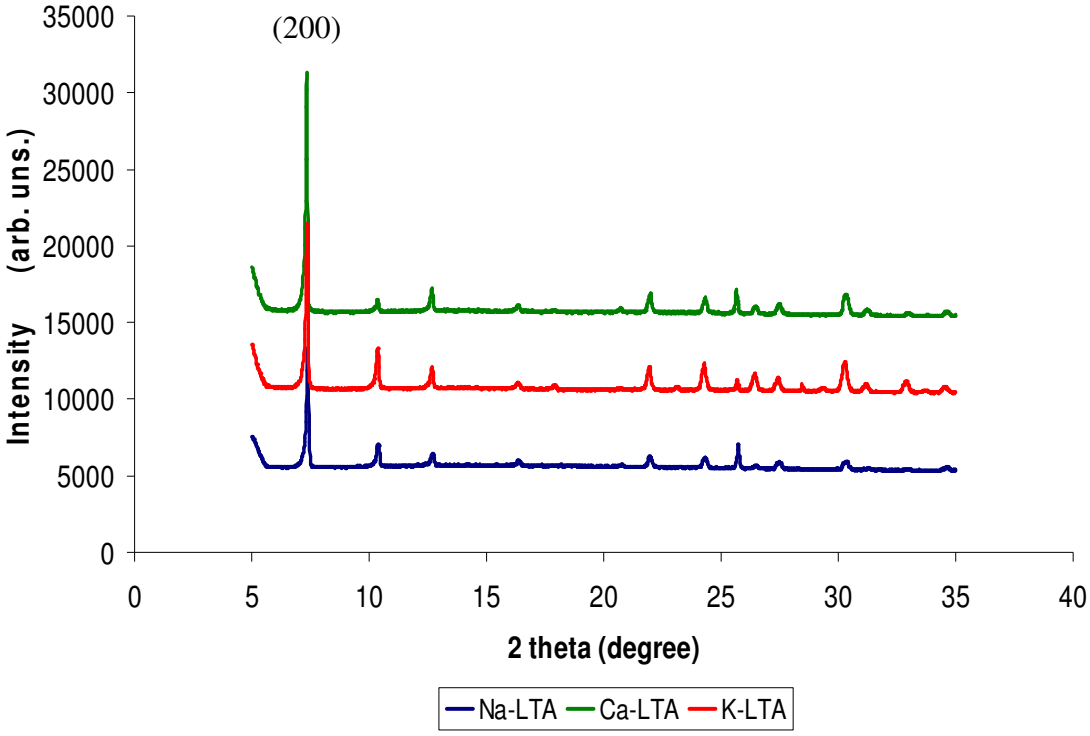

Figure 30: X-Ray diffraction patterns of LTA zeolite with various non-framework metal cations

In order to fabricate a good quality heater on the film surface, the films were polished using procedures developed previously (Chapter III) for MFI films. The final thickness of the LTA films was about 3-5 microns. The composition of the films was investigated by EDS measurements (Table 4) taken from a number of points in the film cross section. All the films show an Si/Al ratio of approximately 1 within the experimental error. As expected, the Al/Cation ratio is about 1 for the univalent cations Na^+ and K^+, and about 2 for the bivalent cation Ca^{2+}.

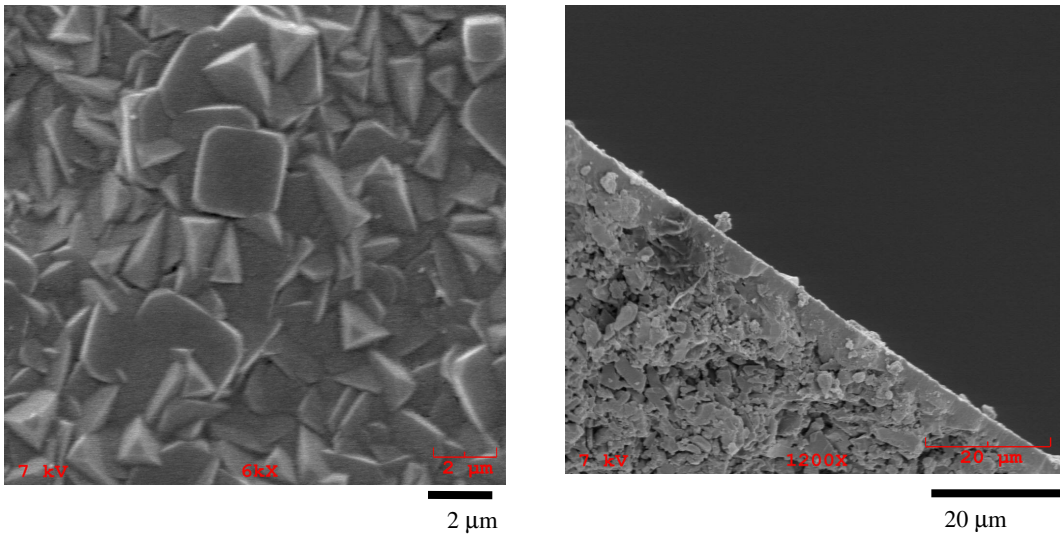

Figure 31: SEM images of non-polished LTA zeolite films

Table 4: LTA film composition for three non-framework cations

Sample ID	Si/Al	Al/cation	Si/cation
Na-LTA	1.18 ± 0.17	1.3 ± 0.21	1.52 ± 0.13
K-LTA	1.33 ± 0.15	1.27 ± 0.2	1.69 ± 0.28
Ca-LTA	1.42 ± 0.2	1.87 ± 0.7	2.6 ± 0.7

The thermal conductivity of LTA zeolite films was obtained via the 3-omega method in a temperature range of 150-450 K. The films were first heated to 450 K, followed by thermal conductivity measurements in vacuum. The thermal conductivity of LTA zeolite films (Figure 32) initially increases as the temperature increases, which mean that the heat capacity is dominated by the temperature dependence on thermal transport properties of LTA zeolite films. However, the Na-LTA thermal conductivity displays a weak maximum at around 340 K, unlike the thermal conductivity of MFI which continues to

increase in the 150-450 K temperature range. The two ion-exchanged materials both have lower thermal conductivities than the as-made Na-LTA and do not display a definite maximum in the thermal conductivity. Detailed modeling and quantitative analysis of these results are ongoing. However, the present data is significant in that (i) it establishes clearly the dependence of the thermal conductivity value on the mass and ionic strength of the extraframework cations, and (ii) it also indicates that the qualitative behavior of the thermal conductivity (specifically the temperature dependence) changes with cation mass and strength, due to changes in the relative contributions of specific heat, umklapp scattering, and boundary scattering processes.

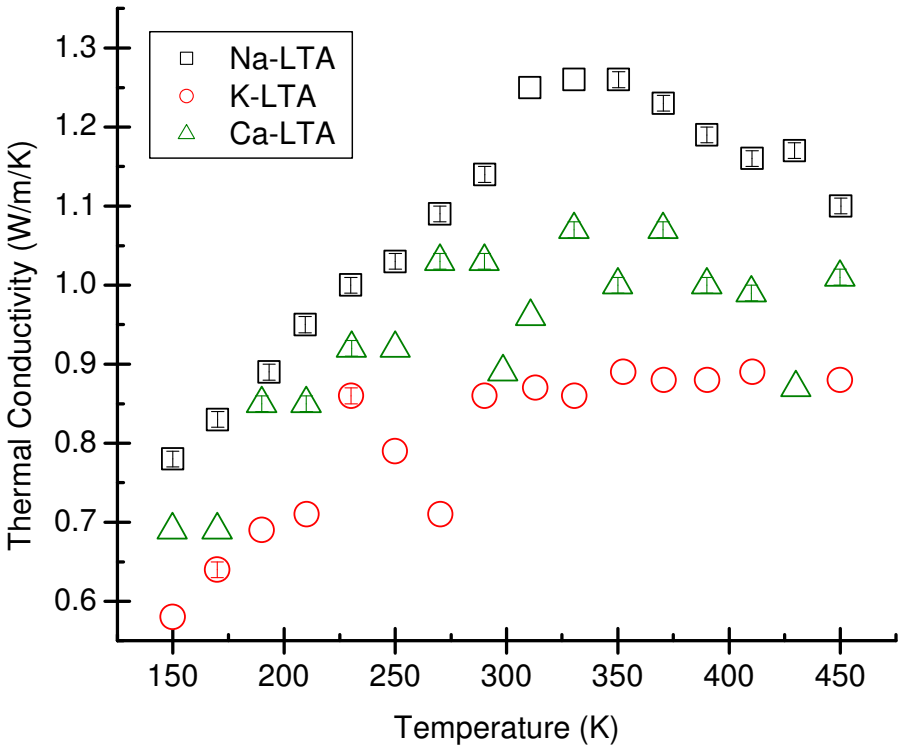

Figure 32: Thermal conducitivity of LTA zeolite films for various non-framework cations

4.4 Conclusions

This chapter presented synthesis and thermal transport measurement of LTA zeolite thin films. We have successfully synthesized continous zeolite LTA films and ion-exchanged them with various metal cations, to obtain samples suitable for high-quality thermal conductivity measurements. The thermal transport properties of these films were successfully measured for the first time, using a 3-omega method. This work shows qualitatively that the behavior of thermal conductivity in LTA is different from that in zeolite MFI. Specifically, the thermal conductivity values of Na-LTA displays a maximum with increasing temperature. The thermal conductivity also changes substantially with the cation mass and valency, indicating that the relative contributions of specific heat, phonon dispersion, umklapp scattering and boundary scattering in a nanoporous material can be altered by ion exchange. Overall, this chapter provides reliable experimental insight into the thermal transport behavior of LTA zeolite films, and also supplies data which is currently being used for quantitative modeling of thermal transport in LTA zeolite films.

CHAPTER V

CALCULATION OF THERMAL TRANSPORT PROPERTIES OF ZEOLITE MFI BY NON-EQUILIBRIUM MOLECULAR DYNAMICS SIMULATIONS

5.1 Introduction and Objectives

Thermal conductivity of solid materials can be predicted using molecular dynamics (MD) simulations. The thermal conductivity calculation using this approach is performed in real space rather than in the reciprocal space (phonon space) as is done for the Boltzmann transport calculation (BTE). Therefore, no prior knowledge of the nature of the thermal transport is required. The position-space and momentum-space trajectories of each atom in the system are then calculated using the Newton's law of motion and an appropriate interatomic potential to describe the interactions between the atoms. However, it is only accurately valid for solids above their Debye temperature [40]. The objectives of the work described in this chapter are to develop an MD simulation code for thermal conductivity predictions, and to evaluate the applicability of MD simulations for thermal conductivity predictions in complex materials.

Two common MD approaches to calculate thermal conductivity are Green Kubo (GK) or equilibrium MD, and the "direct" method or non-equilibrium MD. Atomistic simulations have been widely used in calculating thermal transport of materials. Significant work has been done using equilibrium molecular dynamics [43, 111-115] as well as non-equilibrium molecular dynamics [7, 24, 116-120] to calculate the thermal

conductivity of simple and complex materials. In the GK method, equilibration fluctuations of the heat current are analyzed to calculate the thermal conductivity. The thermal conductivity is described as:

$$k = \frac{1}{Vk_B T^2} \int_0^\infty \frac{\langle \vec{q}(0) \cdot \vec{q}(t) \rangle}{3} dt \tag{5.1}$$

q is the heat current vector, which is calculated from the first law of thermodynamics and is described as:

$$\vec{q}(t) = \frac{d}{dt} \sum_i E_i \vec{r}_i = \sum E_i \vec{v}_i + \frac{1}{2} \sum_{i,j} \left(\vec{F}_{ij} \cdot \vec{v}_i \right) \vec{r}_{ij} \tag{5.2}$$

Where E_i, r_i, and v_i, are the energy, position, and velocity vector of atom i. r_{ij} is the interatomic distance between atoms i and j. F_{ij} is the interatomic force between atoms i and j.

The "direct method" to calculate thermal conductivity imitates experiment by computationally imposing a temperature gradient on the system, monitoring the resulting heat flux, and determining the thermal conductivity from the Fourier's Law (Eqn. 5.3).

$$\vec{q} = -\lambda \cdot \vec{\nabla} T \tag{5.3}$$

In this method, heat of Δq is added/ removed in a thin slab of thickness, *d*. Each particle velocity in the heat source/sink region is scaled by the same factor such that the resulting net kinetic energy is increased and decreased by Δq. The atoms outside this thin slab are allowed to move according to Newton's laws of motion. The existence of heat source and heat sink will increase the scattering of the phonons, which is hypothesized to result in a lower calculated thermal conductivity than obtained from experiments.

Both methods have been used to calculate the thermal conductivity of solids. However, both methods were limited by the finite size effects and relatively a long simulation time. Che and Volz [43, 115] stated that the thermal conductivity values calculated by using equilibrium MD are sensitive to the size of the simulation cell because the phonon mean free path can be longer than the simulation box dimension. However, smaller simulation cells had successfully been used to calculate the thermal conductivity of solids, and the results were comparable with experiment. The GK method gave a slow convergence of heat current which results in a long simulation time. At the same time, the direct method had a different limitation. In order to measure a statistically significant heat current, a large temperature gradients is required. The temperature gradients are so large that the temperature may change by 50% within a few tens of Angstroms. Thus, the assumption of linear response is questionable. Recently, a comparison of GK and "direct methods" observed that when the system size was extrapolated to infinite size, the thermal conductivity obtained from GK method and direct method gave consistent values, even though each has error bars of 20% or more [23].

Atomistic simulation has previously been used by two groups to study the thermal conductivity of zeolites [7, 8]. Kaviany et al. applied equilibrium molecular dynamics using the GK method [7] whereas Murashov [8] used non-equilibrium molecular dynamics. Kaviany et al. studied the thermal conductivity of idealized pure-silica LTA and FAU zeolite frameworks using equilibrium molecular dynamics, and calculated the energy correlation functions of groups of atoms in the zeolite structure. By inspection of the energy correlation functions, they claimed that the lower thermal conductivity in zeolites such as LTA and FAU (in comparison to dense silica crystals such as quartz) is caused by the energy localization near specific groups of atoms and the necessity of circumventing the pore structure. The conclusions of this real-space MD study agree qualitatively with our study of phonon scattering mechanism using a reciprocal-space approach. On the other hand, Murashov [8] investigated the thermal conductivity of quartz and different types of zeolites (LTA, FAU, hypothetical pure-silica-LTA). By calculating the radial distribution function of the atoms in the material, Murashov concluded that the thermal conductivity of zeolites is determined mainly by the vibrations of the oxygen sublattice. The presence of cations and the substitution of silicon with aluminum decrease the thermal conductivity because they distort the oxygen sublattice.

In this chapter, we focus our study of thermal conductivity of zeolite using non-equilibrium MD simulations based on the method proposed by Evans [121]. This method is the combination of the equilibration linear response theory and non-equilibrium molecular dynamics. In this method, a small external force (fictitious force) is exerted on the entire simulation box to replace the temperature gradient as the driving force of the

heat current. This technique is homogeneous with no temperature gradients across the simulation box. The fictitious force will act on each atom depending on the difference between the total energy of each individual atom and the average energy of the entire simulation box. The thermal conductivity is then calculated by:

$$\lambda = \lim_{F_e \to o} \lim_{t \to \infty} \frac{\left\langle J_Q(F_e, t) \right\rangle}{VF_eT} \tag{5.4}$$

The detailed algorithm of this method will be discussed in the next section. We will calculate the thermal conductivity of MFI zeolite as a function of temperature, and compare them with the thermal conductivity obtained from the experiment.

5.2 Methodology

5.2.1 Algorithm

As mentioned in the previous section, in this algorithm, a ficitious force is applied on the entire simulation system to replace the temperature gradients, thus the simulation temperature is uniform across the simulation box. Evans proposed that the equation of motion can be described as:

$$\dot{\vec{r}}_i = \vec{p}_i / m \tag{5.5}$$

$$\dot{\vec{p}}_i = \sum_j \vec{F}_i + (E_i - \overline{E})\vec{F}_e - \frac{1}{2}\sum_{j \neq i} \vec{F}_{ij}\left[\vec{r}_{ij} \cdot \vec{F}_e\right] + \frac{1}{2N}\sum_{j,k} \vec{F}_{jk}\left[\vec{r}_{jk} \cdot \vec{F}_e\right] + \alpha \vec{p} \tag{5.6}$$

Where Fi is the force acting on atom i. Fe is the ficitious force, F_{ij} is the force between atom i and j. α is the Nose-Hoover thermostat parameter. E_i is the total energy of atom i, and E is the instantaneous average energy per atom, which is the sum of kinetic energy and potential energy of the system per all the total number of particles or atoms in the system.

$$\overline{E} = \frac{1}{N}\left(\sum \frac{\vec{p}_i^{\,2}}{2m} + \frac{1}{2}\sum_{i \neq j} \phi_{ij} \right) \tag{5.7}$$

The second term of the equation (5.6) determines the heat current. An atom which has an energy greater than the average energy will move in the direction of the fictitious force (F_e), while an atom with a lower energy than the average energy will move in the opposite direction than F_e.

The Hamiltonian of such system can still be described as the total kinetic and potential energy, which is

$$H = \sum_{i=1}^{N} \left[\frac{\vec{p}_i^{\,2}}{2m} - \sum_{i \neq j} \phi_{ij} \right] \tag{5.8}$$

If the total momentum of the system is conserved, the change in the Hamiltonian is described as:

$$\dot{H}_o^{ad} = \sum_{i=1}^{N}\left[\frac{\vec{p}_i}{m}\cdot\left((E_i-\overline{E})\vec{F}_e - \frac{1}{2}\sum_{j\neq i}\vec{F}_{ij}\left[\vec{r}_{ij}\cdot\vec{F}_e\right] + \frac{1}{2N}\sum_{j,k}\vec{F}_{jk}\left[\vec{r}_{jk}\cdot\vec{F}_e\right]\right)\right] \tag{5.9}$$

As previously mentioned, the heat flux is derived from the first law of thermodynamics is described as in equation (5.2), thus the change in the Hamiltonian depends on the flux of the particles/atoms in the system, which depends on the fictitious force applied to the system.

$$\vec{J}_Q = \sum \vec{v}_i e_i - \frac{1}{2}\sum \vec{r}_{ij}\vec{F}_{ij}\cdot\vec{v}_i \tag{5.10}$$

$$\dot{H}_o^{ad} = -\vec{J}_Q(t)\vec{F}_e \tag{5.11}$$

From the linear response theory, the average heat flux can be described as:

$$\left\langle \vec{J}_Q(t)\right\rangle = -\beta V\int_0^t ds\left\langle \vec{J}_Q(t-s)\vec{J}_Q\right\rangle\cdot\vec{F}_e \tag{5.12}$$

Thus, the thermal conductivity is defined as the ratio of the average heat flux to the product of the temperature and the magnitude of the fictitious force at the limit of t goes to infinity and fictitious force goes to zero.

$$k = \frac{V}{k_B T^2}\int_0^\infty dt\left\langle J_Q(t)J_Q(0)\right\rangle = \lim_{t\to\infty}\lim_{F_e\to 0}\frac{-\left\langle J_Q(\infty)\right\rangle}{TF_e} \tag{5.13}$$

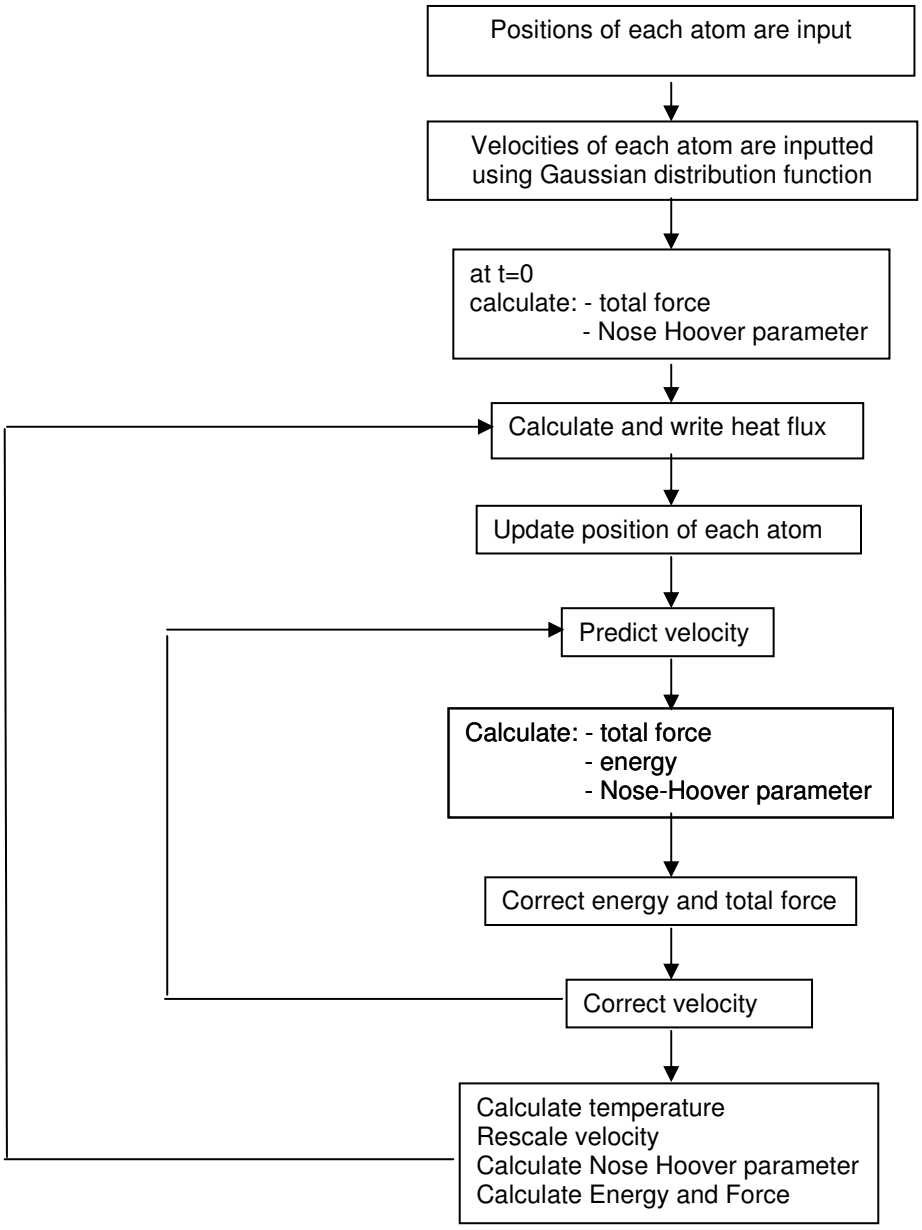

Figure 33: Non-equilibrium molecular dynamics algorithm to calculate thermal conductivity using Gear predictor-corrector integration.

5.2.2 Simulation code

The code was written in FORTRAN, and the detailed algorithm is presented in Figure 33. The equations of motions were solved using the Gear predictor-corrector algorithm. The initial positions of the atoms were obtained from published crystal

structure data. The initial velocity of each atom was assigned randomly from a Gaussian distribution function. Parallelization of the code has been implemented using MPI directives. The total force, and the average heat flux, is calculated and output. The Nose-Hoover thermostat was used to control the temperature of the simulation. These steps are repeated until the total simulation time is reached.

5.2.3. Code Validation

Solid argon was used as a simple model material to test and debug the code. The non-bonded interatomic interactions between the argon atoms are described by the Lennard-Jones potential:

$$U_{ij} = 4\varepsilon\left(\left(\frac{\sigma}{r_{ij}}\right)^{12} - \left(\frac{\sigma}{r_{ij}}\right)^{6}\right) \tag{5.14}$$

where U_{ij} is the potential energy between atom i and j. ε is the depth of the potential energy well. σ is the equilibrium distance between atom i and j, and r_{ij} is the actual distance between atom i and j. The Lennard-Jones parameters are 3.4 10^{-10} m for σ, and 1.67 10^{-21} Joule for ε. The simulation was conducted in the NVT (constant mass, volume and temperature) ensemble with a time step of 1 fs, and used a periodic boundary condition.

Prior to collecting production data, the Nose-Hoover thermostat parameter was adjusted. The Nose-Hoover thermostat parameter in our simulation is defined as

$$\alpha = \frac{dt^2}{1.5Nk_BTt_{dec}^2}, \tag{5.15}$$

wherein dt is the integration time step in the simulation, N is the number of atoms in the simulation, T is the simulation temperature, and t_{dec} is the characteristic decay time, which is optimized. The value of t_{dec} was systematically varied and the thermal conductivity values were computed for each case until the thermal conductivity values did not change any further (e.g., Figure 34). This establishes the optimal value of the Nose-Hoover parameter. Specifically, a decay time of 100 ps was chosen because it gives the most reliable results. Please see Appendix A for the correlation between heat flux convergence and the decay time.

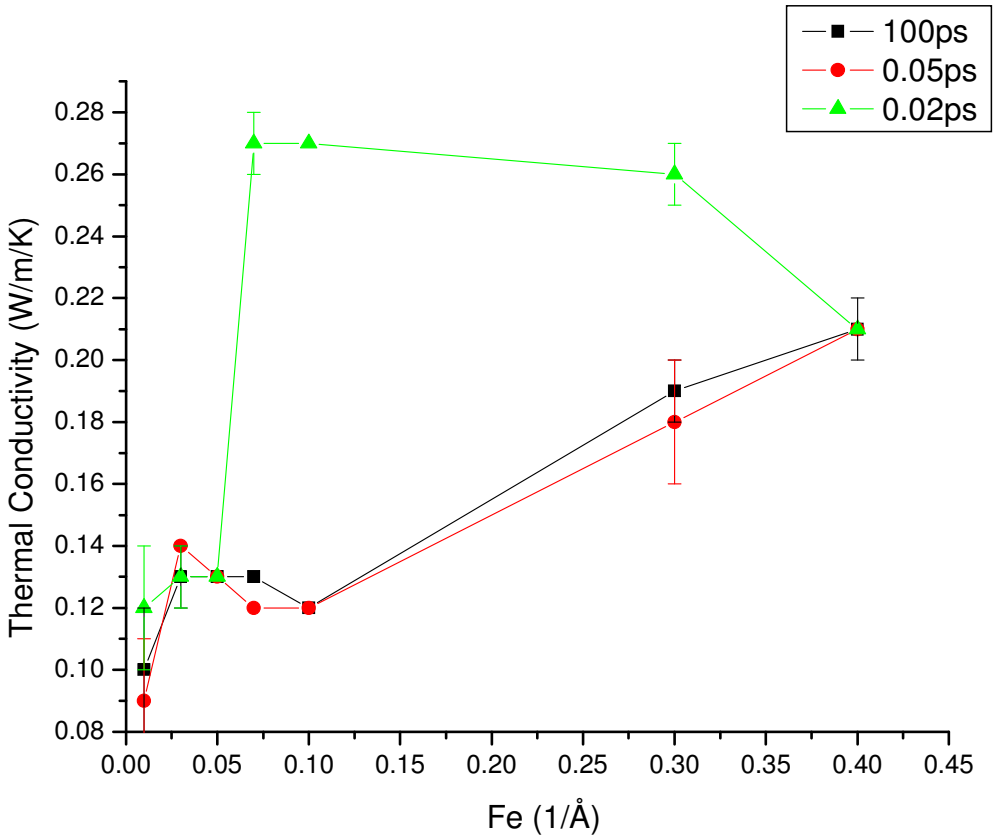

Figure 34: The thermal conductivity of solid argon at 86.5 K as a function of decay time and the fictitious force.

The test simulations were conducted in all three lattice direction (a, b, and c directions) at the triple point temperature (T = 86.5 K), and the results were compared to the literature values. The simulation box is cubic with a total of 108 argon atoms. In the beginning of the simulation, the structure was first equilibrated by conducting the simulation without applying the external force. After 40 ps, the external force was applied to the system, and the average heat flux was collected for every output time step. The thermal conductivity for each external force was obtained by averaging the average heat flux over time as the average heat flux became stable (from 80 ps to 125 ps), see

Figure 35. The thermal conductivity was plotted as a function of external force, and the thermal conductivity values for very small external forces were averaged out to eliminate the larger statistical errors on simulations carried out under such conditions.

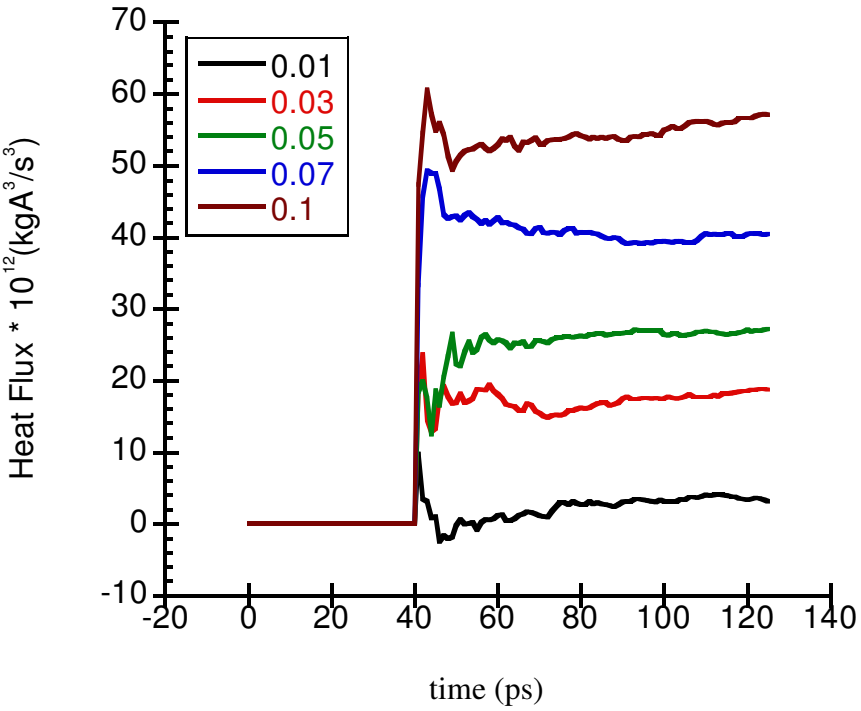

Figure 35: Heat Flux of Argon in the *a*-direction at triple point simulation

Before using the code to perform calculations on MFI, it was further validated by testing it on quartz, a much simpler material with the same chemical composition (SiO_2) as pure-silica MFI. This test would also be helpful in testing the quality of the force field, since we used the same force field for both quartz and MFI. In the case of quartz, we used a simulation box with 243 atoms. The interactions were modeled using the Beest-Kramer-van Santen (BKS) [51] potential, which is described as:

$$U_{ij} = \sum_{i>j} \frac{q_{\alpha i} q_{\alpha j}}{r_{ij}} + \sum_{i>j} \left[A_{\alpha i \alpha j} \exp(-b_{\alpha i \alpha j} r_{ij}) - C_{\alpha i \alpha j} r_{ij}^{-6} \right] \quad (5.16)$$

The first term contains the long range electrostatic interaction between the effective charges on atom i and j and on species α, which was described using Wolfe electrostatic. The second term contains the short range non-bonded interaction between atom i and j. Those parameters are presented in Table 5.

Table 5: Force field parameters [51]

α_i-α_j	$A_{\alpha i-\alpha j}$ (eV)	$b_{\alpha i-\alpha j}$ ($Å^{-1}$)	$C_{\alpha i-\alpha j}$ (eV $Å^{6)}$	q_α
O-O	444.7686	2.48513	0	q_O = -1.1
Si-O	24441.24	4.93504	180.8045	q_{Si} = 2.2

The electrostatic interaction is described using the Wolf method [122]. In this method, the electrostatic interaction is described as:

$$\frac{q_i q_j}{r_{ij}} \cong \frac{q_i q_j erfc(\alpha r_{ij})}{r_{ij}} \quad (5.17)$$

where α is the damping parameter, and is chosen so that the long-range many-body Coulomb summation can be replaced by a short-range term as given above. As previously determined [122], the α value is chosen to be 4/L where L is the size of the simulation

box. The simulation was conducted with the simulation time step of 0.5 fs for a total simulation time of 200 ps. The system was first equilibrated for 50 ps. The heat flux was averaged out from the time of 100 ps to 200 ps, which is shown the stability (Figure 36). NVT ensemble was applied, and the thermal conductivity was calculated at temperature equal to 300 K in the a-direction.

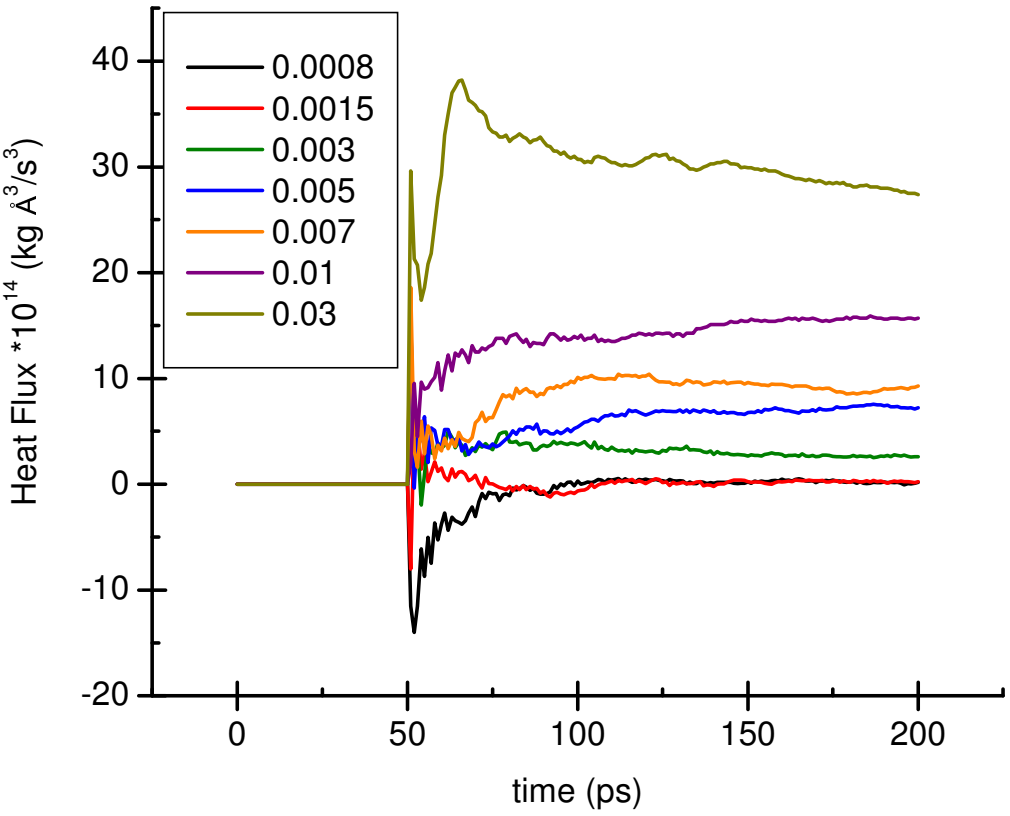

Figure 36: The average heat flux of quartz for different fictitious forces.

The calculation of thermal conductivity of MFI was then performed, using the KBS force field. The MFI structure was first energy-optimized. The simulation was conducted on one unit cell because the system was large; the number of atoms in one

simulation box is 288 atoms. The minimized structure was then equilibrated for 50 ps, and the simulation was conducted for a total of 200 ps. The simulation time step was 20 fs. The thermal conductivity for each external force was obtained by averaging the average heat flux over time as the average heat flux became stable (from 150 ps to 250 ps).

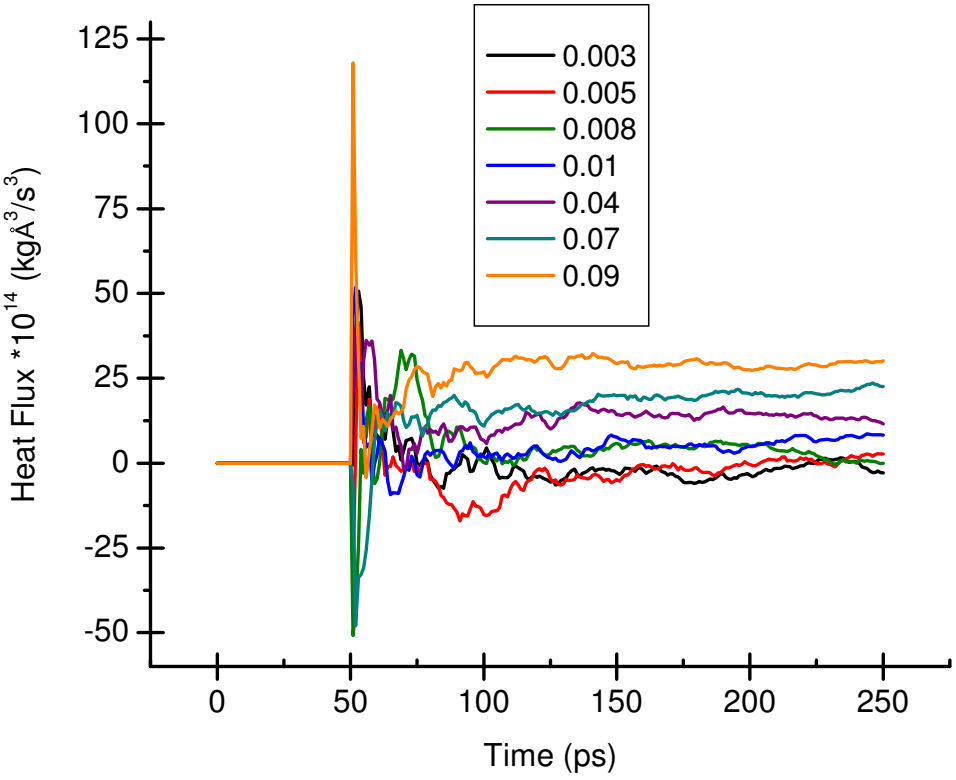

Figure 37: Average heat fluxes of (002) MFI at 300K calculated by NEMD with different fictitious force values

5.3. Results and Discussion

The thermal conductivity of argon as a function of external force is shown in Figure 38. The thermal conductivity at low external forces has large error, due to the relatively small magnitude of the external force term relative to the thermal fluctuations. Thus, the thermal conductivity is obtained by averaging out the values calculated below an external force of 0.08 $Å^{-1}$. The thermal conductivities of argon in all lattice directions are presented in

Table 6. The thermal conductivity showed good agreement with literature data, thus validating the nonequilibrium molecular dynamics algorithm.

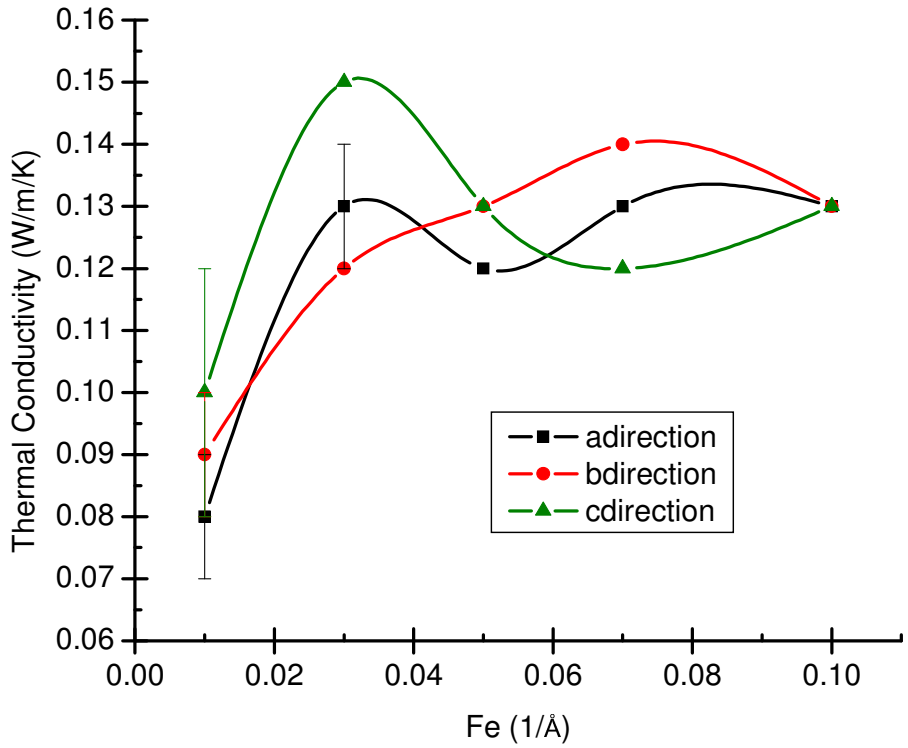

Figure 38: The thermal conductivity of argon at various fictitious forces for *a*, *b*, and *c* directions

Table 6: Thermal conductivity of argon at 86.5 K

direction	Average (W/m/K)	St. Deviation	Literature (W/m/K)	% error
a-direction	0.118	0.005	0.13	-9.367
b-direction	0.121	0.004	0.13	-6.679
c-direction	0.128	0.006	0.13	-1.763

Furthermore, the thermal conductivities of Argon at several other temperatures were calculated, and the results are shown below inFigure 39. As can be seen, there is excellent agreement of the results with previously reported experimental values for the thermal conductivity of solid argon.

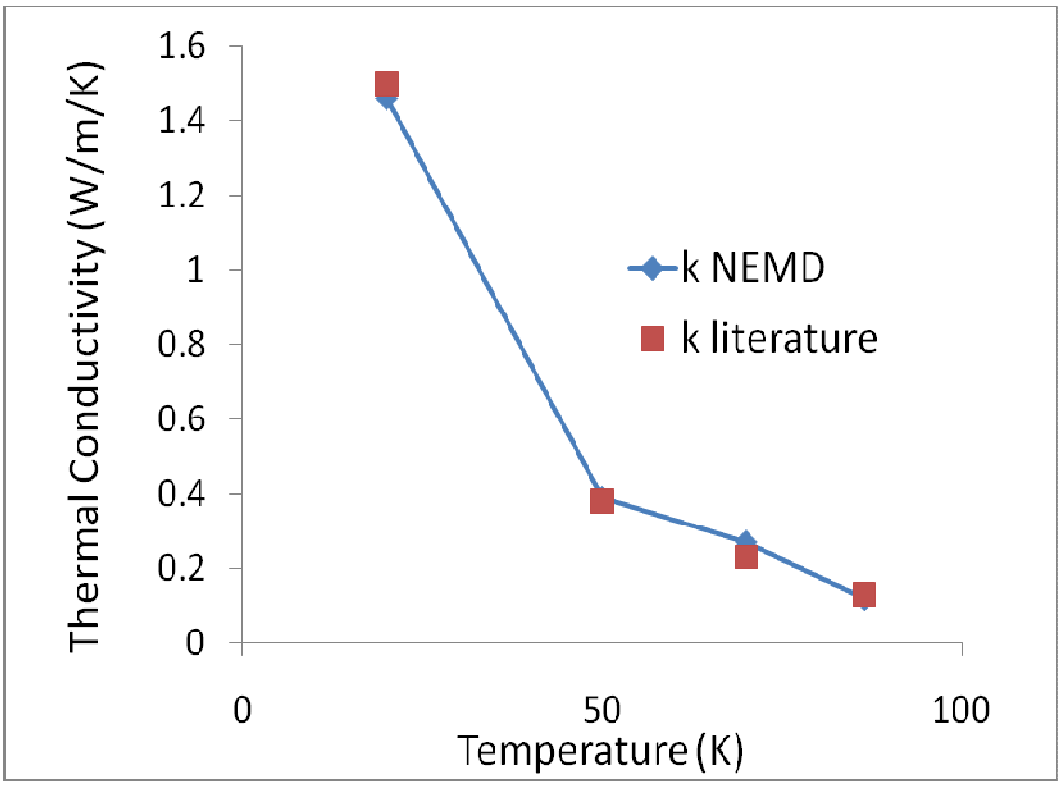

Figure 39: Thermal conductivity of solid argon at temperature of 20, 50, 70, and 86.5 K. The literature thermal conductivity values were obtained from [116, 123]

The calculated thermal conductivity of quartz in the *a*-direction was also shown to be in agreement with the experiment data. The thermal conductivity of quartz as a function of fictitious force in the a-direction is shown in Figure 40. The thermal conductivity is obtained by averaging the results from F_e= 0.003 $Å^{-1}$ to F_e = 0.03 $Å^{-1}$. The thermal conductivity was evaluated for various temperatures, and they were compared to experimental data from the literature. Figure 41shows excellent agreement between the calculated thermal conductivity from NEMD and the experimental data within the error bar of the simulations. This also shows that the force field accurately predicts the interatomic interactions in quartz, and thus also in pure-silica MFI zeolite.

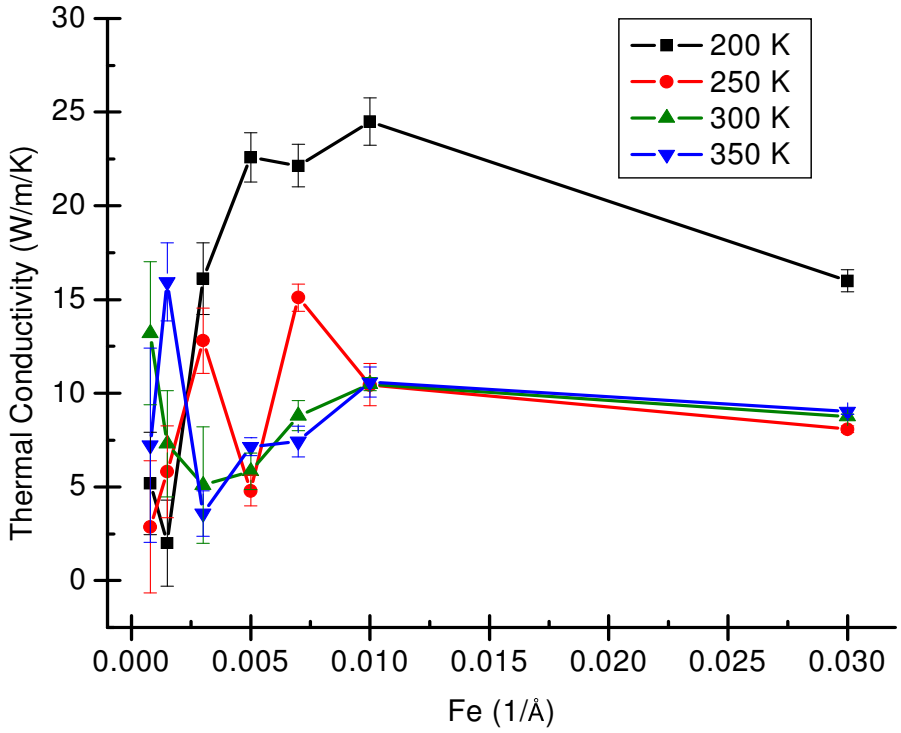

Figure 40: The thermal conductivity of quartz in a-direction at various temperatures, and as a function of fictitious force.

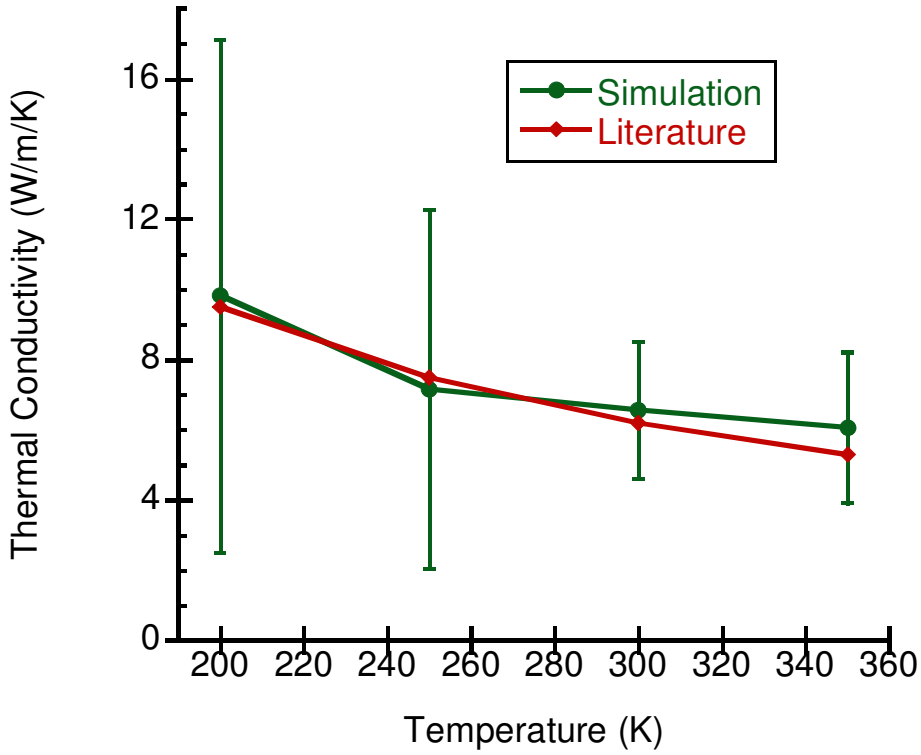

Figure 41: The thermal conductivity of quartz as a function of temperature, comparison between the NEMD simulation (this work) and experiment values [124]

The thermal conductivity of MFI in the c-direction is presented in Figure 42. The conductivity was obtained by taking the average of results obtained using external forces between 0.008 $Å^{-1}$ and 0.07 $Å^{-1}$. The calculated thermal conductivity at 298 K is 2.58 $\pm$ 0.55 W/m/K, which is not in good agreement with our experimental result (1.02 W/m/K). The (101) direction thermal conductivity of pure-silica MFI was also investigated. The thermal conductivity was calculated at three temperatures in order to compare to the experimental data. The thermal conductivity was obtained by applying external force in

(101) direction. The heat flux in (101) was obtained (Figure 43)(Figure 43) from the computed heat fluxes in a-direction and c-direction for each output time step:

$$J_Q^2 = J_{Qx}^2 + J_{Qz}^2 \tag{5.17}$$

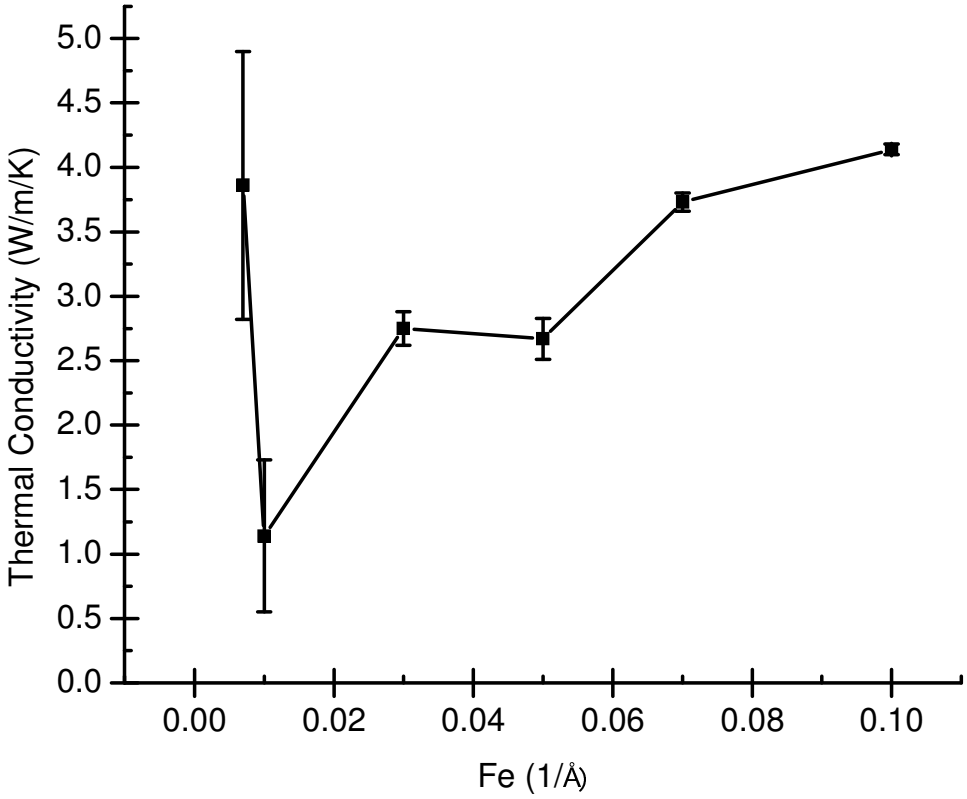

Figure 42: The thermal conductivity of pure-silica MFI in c-direction at 298 K

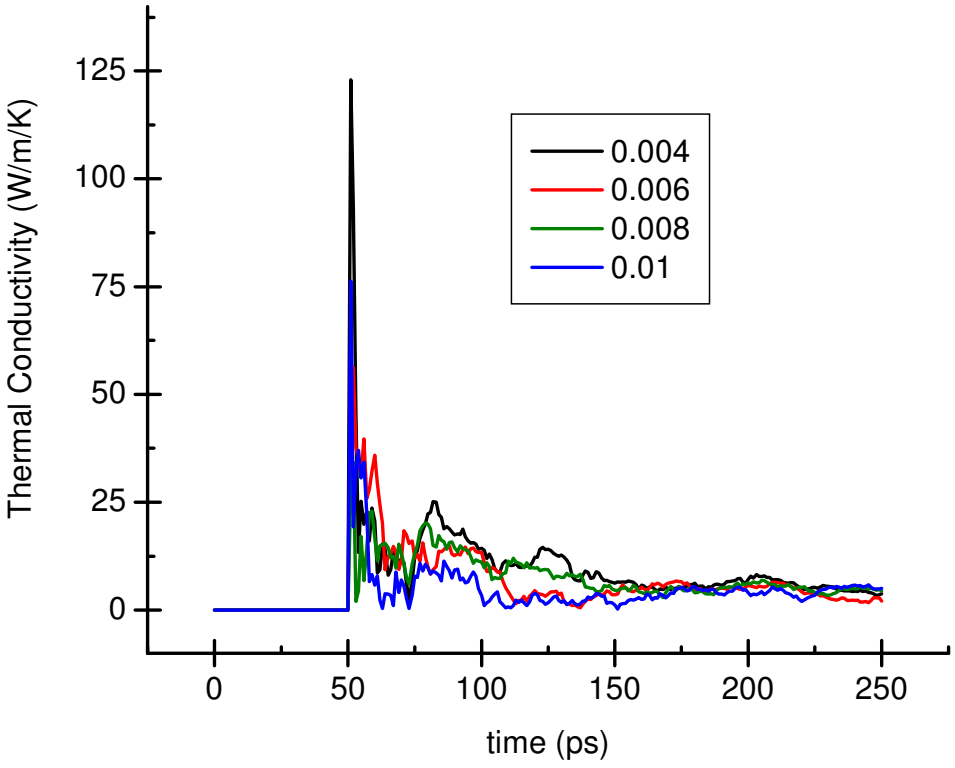

Figure 43: Heat flux in (101) direction of pure-silica MFI at 298 K

The thermal conductivity (Figure 44) increases as the temperature decreases, which was not observed in the experiments. This phenomenon can be due to the fact that classical MD simulation (which assumes Maxwell-Boltzmann statistics) cannot capture the quantum statistical effects of phonon propagation, specifically the Bose-Einstein statistics of the phonons. Similarly, Kaviany [125] observed that in a simple Lennard-Jones system, the transverse phonon polarization behaves differently at low and high temperatures, and that the longitudinal and transverse relaxations became similar at high temperature as expected for a system obeying Maxwell-Boltzmann statistics. While these effects are relatively unimportant in simple materials such as argon and quartz (which have only a few unique phonon branches in their unit cells), they can be quite important

for complex materials such as MFI which have a large number of phonon branches. The simulation cell size can also affect the calculated thermal conductivity. Zeolites have large unit cells (e.g., MFI has 288 atoms in one unit cell), therefore increasing the size of the simulation cell and requiring a larger computational time for full convergence of the heat flux. Furthermore, the previous analysis has revealed the small mean free path (~ 5 nm) for boundary scattering of phonons from the pore network in MFI. Thus, the simulation cell may not be large enough to accurately represent the boundary scattering contributions.

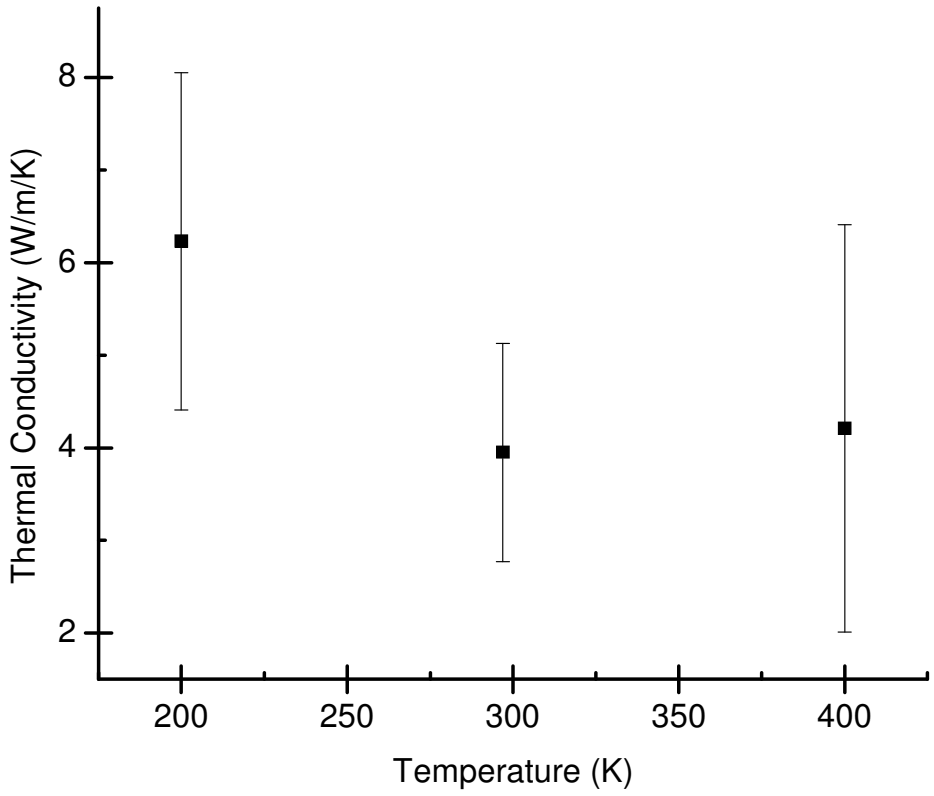

Figure 44: The thermal conductivity of Silicalite MFI in (101) direction at various temperatures.

5.4. Conclusions

In this chapter, we have described a molecular simulation method adapted from Evans to calculate the thermal conductivity of solids. We have built a simulation code that is capable of evaluating the thermal conductivity of simple materials. The thermal conductivity of both argon and quartz were calculated and showed agreement with the experiment values. The thermal conductivity of pure-silica MFI zeolite was also calculated. MD simulations, however, could not predict the thermal conductivity in the (101) silicalite MFI as a function of temperature, we suspect that this is due to the following factors (1-3 being the primary factors, whereas 4 and 5 are likely of a secondary nature):

1. The quantum statistical (Bose-Einstein) properties of the phonons, as opposed to Maxwell-Boltzmann behavior assumed in classical MD.
2. The finite simulation cell size effects on the heat flux convergence.
3. The finite simulation cell size effects on capturing the phonon scattering events.
4. Possible deficiencies in the force field.
5. Assumption of perfect crystal lattices with no defects.

In the light of the above factors, we believe that MD-based computational results on thermal conduction in zeolites and complex materials in general, should be interpreted with caution. We therefore currently believe that the combined experimental-BTE approach described in previous chapters offers a more tractable alternative for describing

thermal conduction in such materials. However, our results corroborate the utility of classical MD for predicting the thermal properties of simpler materials with few phonon branches and which are close to (or above) their Debye temperature so that classical statistics provides a good approximation of the phonon behavior.

CHAPTER 6
CONCLUSIONS AND RECOMMENDATIONS FOR FUTURE WORK

6.1 Summary of Current Work

We have focused our study on thermal transport properties of zeolite materials because these materials have a complex but yet well defined structures. In addition, the framework and non-framework composition can be altered, which allow the study of thermal transport mechanism in molecular scale. We chose two types of zeolites, MFI and LTA, which have been widely used. We have studied both by experiment and simulation – the heat transport properties of these materials. Both the effect of framework atom substitutions and non-framework cations on the thermal transport mechanisms were investigated using MFI zeolite and LTA zeolite respectively. We found that the main phonon scattering mechanism limiting the thermal conductivity of nanoporous crystals such as MFI is the boundary-like scattering from the pore network. We also find that Al incorporation significantly suppresses the thermal conductivity due to a combination of phonon slowing and localized phonon scattering, and not due to specific heat or isotope scattering effects. It is important to emphasize that the present approach, although approximate in the handling of the phonon scattering, still represents a considerable advance in measuring and modeling the thermal conductivity of zeolite materials.

We have also seen, using zeolite LTA as our second model system, that the balance of specific heat, phonon dispersion, umklapp scattering, and boundary scattering

can be altered significantly by introducing non framework metal cations with different ionic strengths and masses. We found that the thermal conductivity values of LTA zeolite films decrease as the cation mass and strength increase. Also, the thermal conductivity of Na-LTA zeolite films showed a maximum as a function of temperature. These interesting and novel observations are now being investigated further by quantitative modeling to better understand the phonon scattering mechanisms operating in zeolite LTA and to compare it with the behavior observed in zeolite MFI.

Overall, we have made substantial progress in developing a robust framework for measuring, understanding, and modeling thermal transport phenomena in complex crystals, and in separating the mechanistic contributions from different phonon scattering processes. The important roles of boundary and defect scattering, as illustrated by the present work, also imply that the thermal conductivity of these complex crystals can be tuned by exploiting not only the composition but also the pore structure.

We have also investigated the simulation of thermal conductivity using non-equilibrium MD. We find that even though MD simulation can be used to accurately predict the thermal conductivity of simple Lennard-Jones solids such as argon, and dense silicates of simple structure such as quartz, there is considerable doubt whether it can be used to accurately calculate the thermal transport properties of complex materials such as zeolites. Several reasons for this problem have been suggested, including the existence of quantum statistical effects, system size limitations, and assumptions of defect-free structural models.

6.2 Recommendations for Future Work

6.2.1 Quantitative Analysis of Thermal Conductivity of LTA Zeolite Films

As presented in Chapter 4, the thermal conductivity of LTA zeolite films is indeed affected by the non-framework metal cations for reasons explained qualitatively earlier in this thesis. In order to quantitatively analyze these phenomena, a detailed phonon scattering mechanistic analysis needs to be conducted, in a manner similar to that conducted for zeolite MFI. As part of the collaboration with A. Greenstein in the School of Mechanical Engineering, the phonon dispersion behavior of LTA zeolite materials are being calculated using lattice dynamics, and their thermal conductivity behavior is being modeled by means of the Boltzmann transport equation. The boundary scattering, umklapp scattering, specific heat contribution, and phonon dispersion effects are being incorporated. The ongoing work is expected to result in the desired quantitative insights into the effects of extra-framework cations.

6.2.2 The Effects of Inclusion of Organic Molecules in Zeolite Pores

As shown in this thesis, the thermal transport properties of zeolites are strongly influenced by the zeolite pore network. One of the ways of tuning the properties of the pore network is by inclusion of metal cations (Chapter 4). However, this can also be accomplished by the inclusion of organic molecules in the pores. The inclusion of organic molecules in zeolite is well-studied [126-129]. Several researches have shown that inclusion of organic molecules in zeolite pores can create nonlinear optical properties which are dramatically different from either the host or the guest molecules properties

[128]. The wide variety of the zeolite pore structure, size, shape, and framework charge density allows the zeolite host to be matched with the organic molecules. This means that the interaction between the guest-guest molecules and guest molecule- host framework can also be tuned [127]. We have made preliminary investigations of the effect of inclusion of tetrapropylammonium bromide, which is the organic template for MFI zeolite synthesis. Our measurements show an increase in the thermal conductivity of zeolite (Figure 45) when it is uncalcined and therefore includes the organic template in the pore structure. The increase in the thermal conductivity can be due to various factors such as the interaction between the framework and the guest molecules thus increasing the phonon velocity, or changes in the specific heat of the material.

The effects of organic species included inside the pore network is thus an interesting subject for future work. In particular, it could provide a method for tuning the thermal conductivity of porous materials. Furthermore, it poses interesting theoretical challenges in describing phonon scattering mechanisms. Currently available theoretical expressions for phonon scattering from localized sites contain a number of assumptions that are likely not valid in describing the interaction of organic molecules with the phonons.

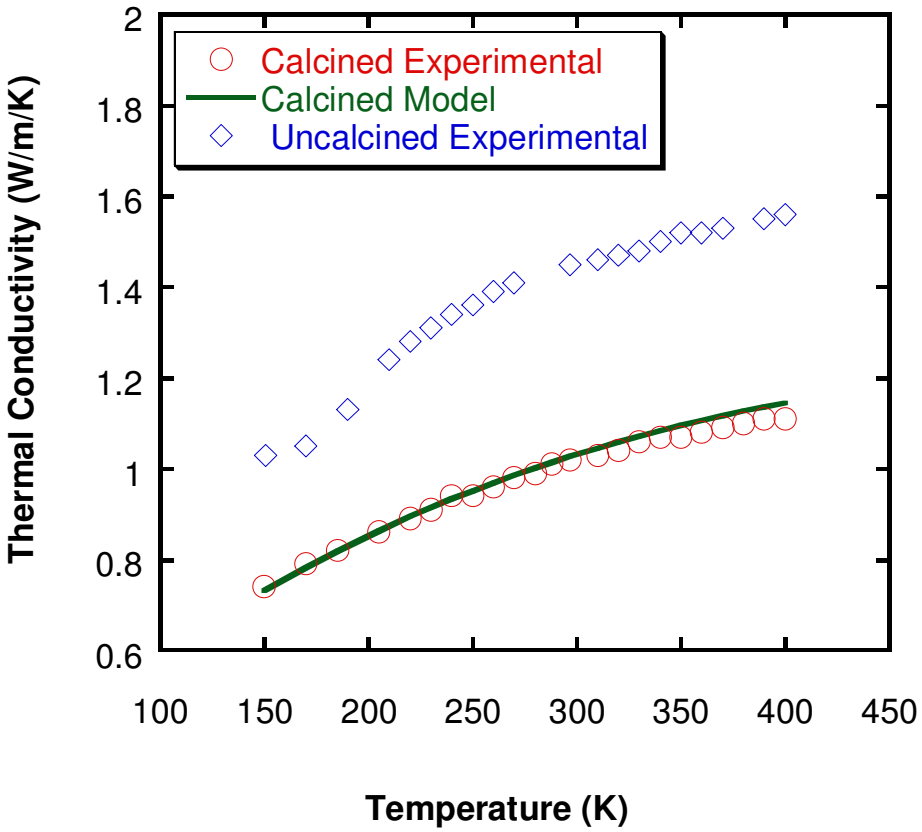

Figure 45: Comparison of thermal transport properties of calcined and uncalcined MFI zeolite [6].

6.2.3 Thermal Conductivity Measurements using a Photoacoustic Method

Although our thermal conductivity measurements using 3-omega method provided a set of high-quality thermal conductivity data, the method is still rather laborious and sensitive to a number of experimental conditions. The surface roughness of the film plays an important role in obtaining a good heater deposition, and thus ensuring a high signal-to- noise ratio in the measurement. Photoacoustic methods have been

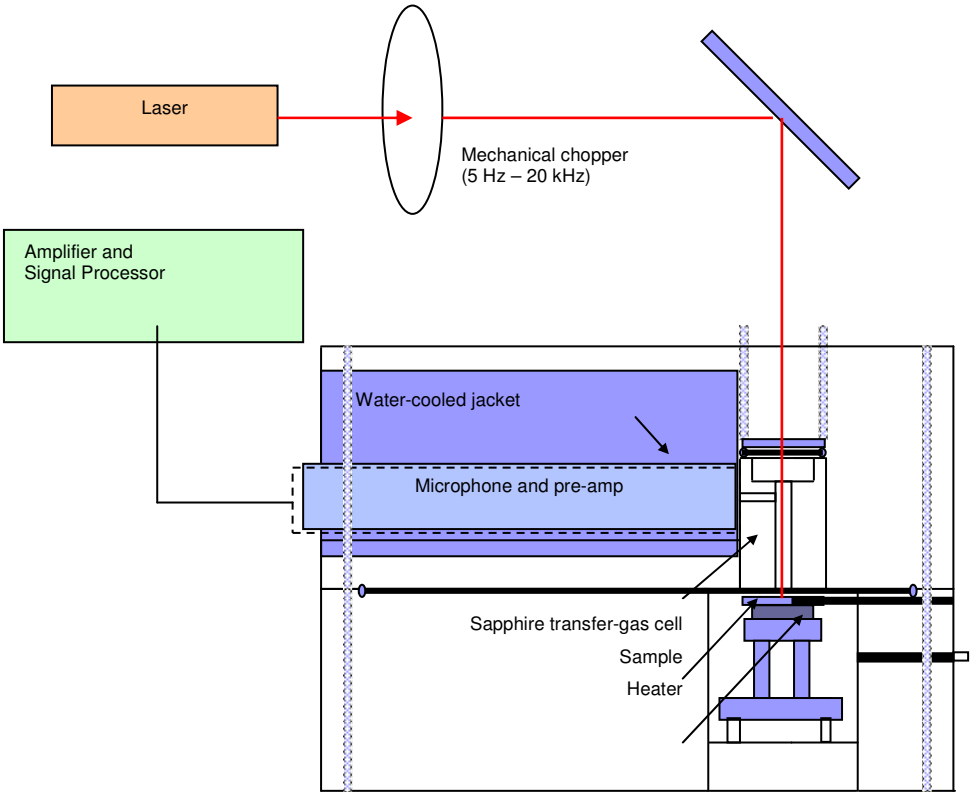

Figure 46: Schematic of photoacoustic system for measuring thermal conductivity. A laser and mechanical chopper provide a pulsed source to thermally excite the sample. The photoacoustic response transferred by the gas (e.g., helium) in the sapphire chamber above the sample, is detected by a microphone and analyzed with a simple heat transfer model of the gas. The sample temperature can be controlled up to about 700 K, and the microphone is water- cooled.

considered in order to measure the thermal conductivity of semiconductor materials [130-135]. This method will be considerably simpler than 3-omega methods because, the surface morphology of the film does not affect the photoacoustic signal. The photoacoustic technique has previously been studied in our group to non-invasively measure the concentration profile of MFI zeolite [136, 137]. These studies have shown that MFI zeolite gives a high photoacoustic signal-to-noise ratio. We have designed, and

partially built, a photoacoustic system to measure the thermal conductivity of thin films (Figure 46). The system is currently designed to measure the thin film thermal conductivity from room temperature to about 450K. Future work would consist of fully operationalizing the system and using it to perform thermal transport measurements under a variety of conditions.

6.2.4 Thermal Conductivity Calculation Using Non-Equilibrium Molecular Dynamics Simulation

As presented in Chapter 5, the non-equilibrium molecular dynamics can accurately predict the thermal conductivity of simple materials such as Argon and Quartz. However, this method has possibly failed to correctly predict the thermal conductivity of MFI zeolite. As described in the previous chapter, the phonons followed Bose-Einstein distribution, while in classical MD; the momentum follows the Maxwell-Boltzmann distribution. Thus, classical MD cannot predict the temperature dependence on the specific heat and thermal conductivity accurately. Accounting the quantum effects in the MD simulations is currently not practical. In fact, the idea of classical MD simulations is to ignore the quantum effects and thus save computational time. Therefore, several authors have addressed this issue by mapping the classical MD results on to an equivalent quantum system [138]. This method could be explored further in the future.

Finally, one of the important parameters in this NEMD method is the choice of the fictitious force. One issue that has not been studied in detail in this thesis pertains to the limit of fictitious force values that are require to obtain correct thermal conductivity

values. This issue can possibly be addressed in a manner similar to that employed in the Parinello-Rahman molecular dynamics method (PRMD) [139]. PRMD is usually used to investigate phase transitions, mechanical behavior of solids, elastic constants, and materials compressibility. In PRMD, the shape, volume and orientation of the simulation cell are treated as variables, and the materials properties are calculated from the sampled fluctuations of thermodynamic functions. A detailed algorithm for this method can be found in [140]. Previous studies have found that the thermodynamic convergence in PRMD depends on the appropriate choice of the cell mass. This cell mass parameter is comparable to the fictitious force used in this thesis, and hence it may be possible to develop a similar method to determine the appropriate choice of fictitious force.

APPENDIX A

The detailed MD simulation data for Argon at 86.5 K are presented below. The effect of the decay time on the heat flux was observed. The simulation was conducted on a cell with 108 Argon atoms.

Decay time = 0.02 ps

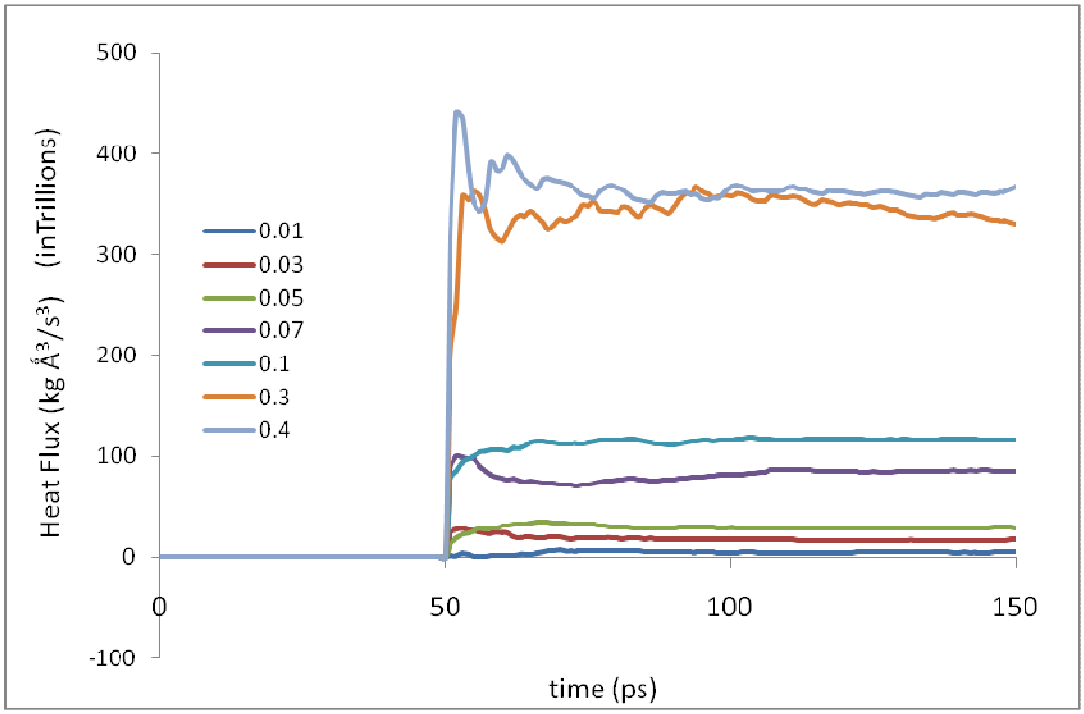

Figure 47: The calculated heat flux of solid argon with the Nose-Hoover parameter of 0.02 ps

Decay time = 0.05 ps

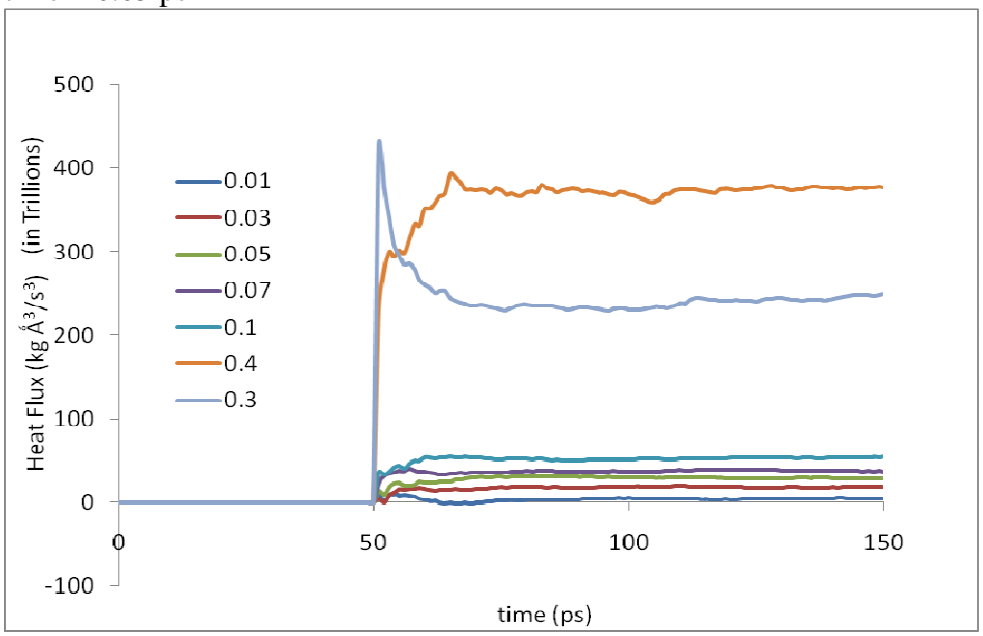

Figure 48: The calculated heat flux of solid argon with the Nose-Hoover parameter of 0.05ps

Decay time = 100 ps

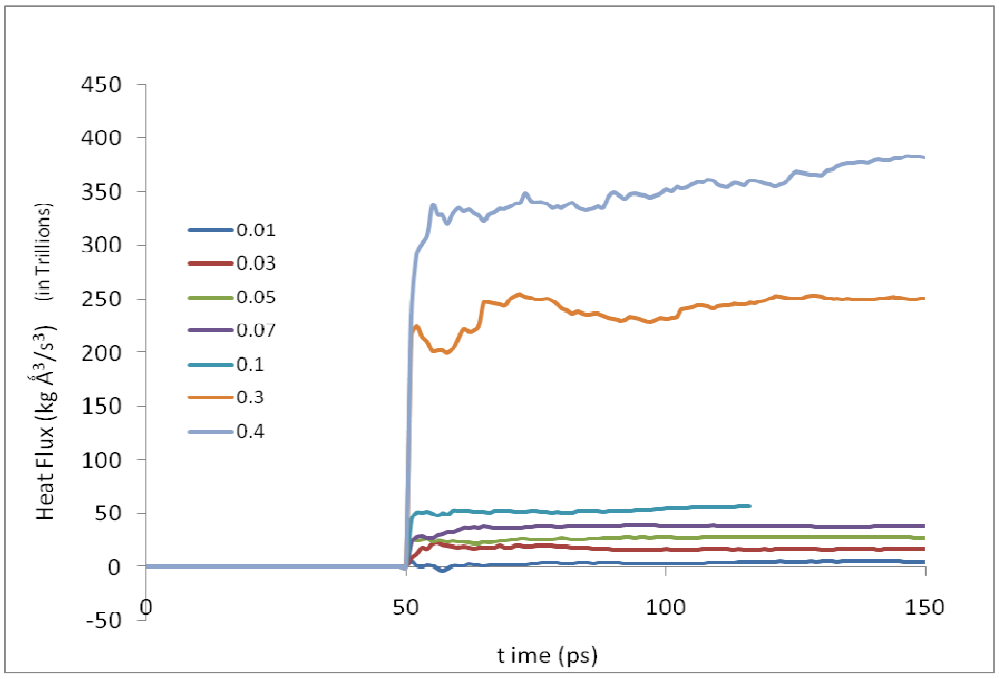

Figure 49: The calculated heat flux of solid argon with the Nose-Hoover parameter of 100 ps

APPENDIX B

The thermal conductivity of solid Argon was calculated at temperatures of 20K, 50K, and 70K. The thermal conductivity responses as a function of fictitious force are presented in this appendix. The calculated heat fluxes are also presented.

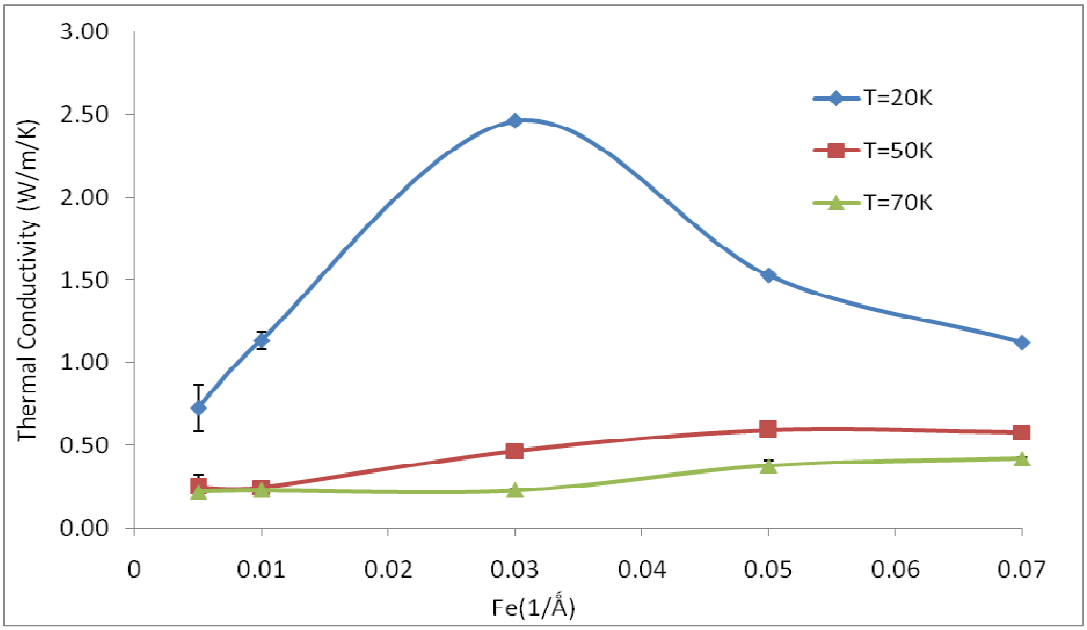

Figure 50: Thermal conductivity of solid argon (108 atoms) as a function of fictitious force at temperature of 20, 50, and 70K

T = 20K

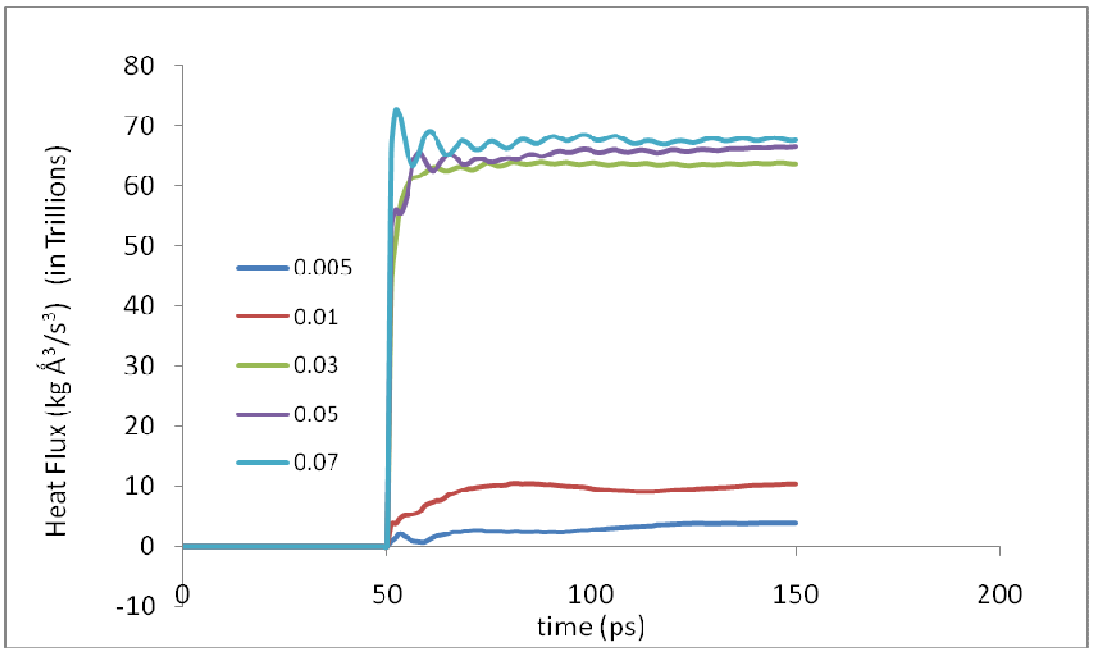

Figure 51: The calculated heat flux of solid argon at 20K

T = 50K

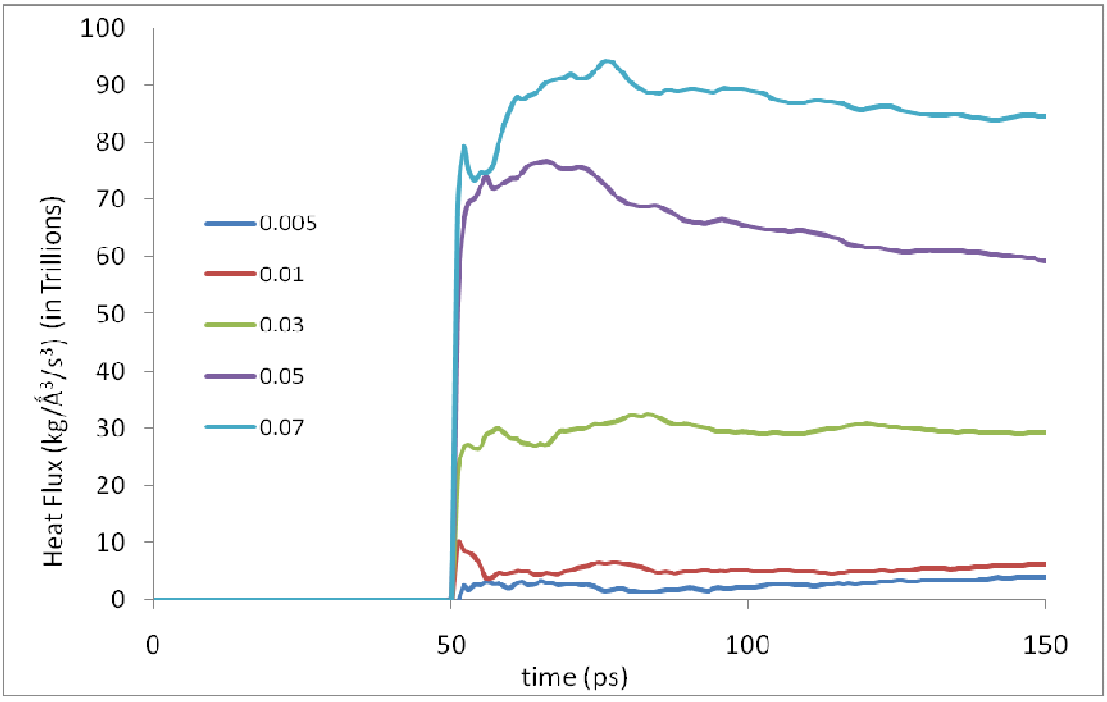

Figure 52: The calculated heat flux of solid argon at 50K

T = 70K

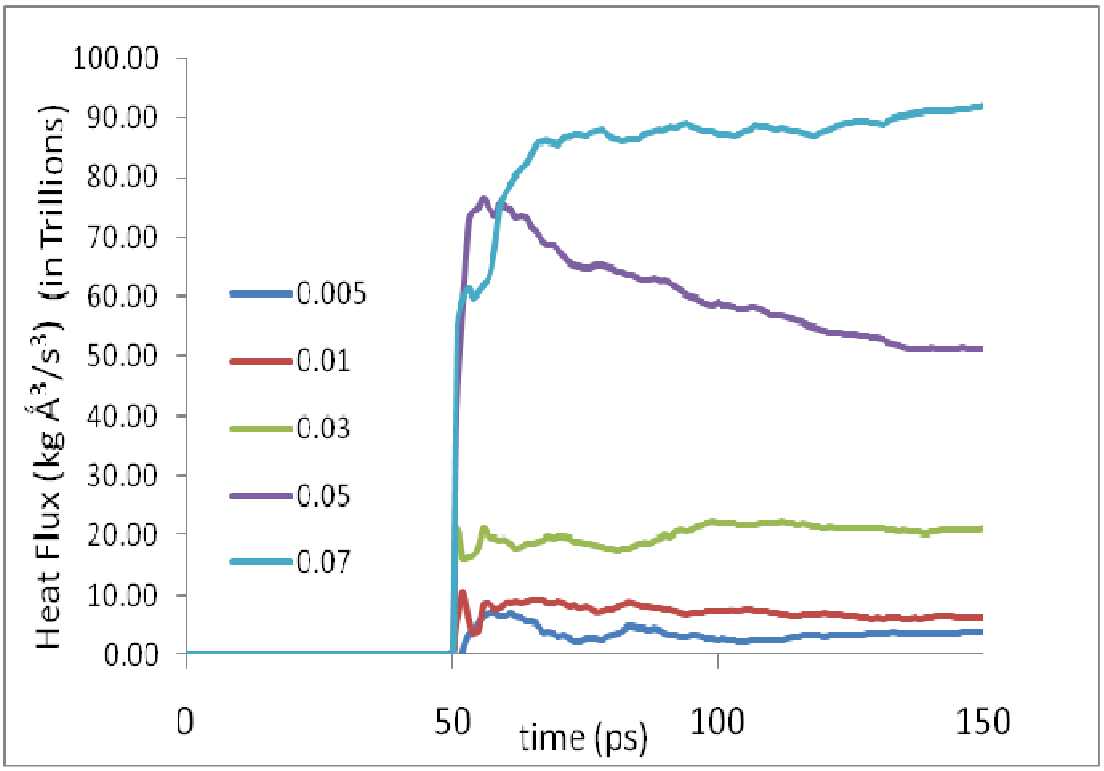

Figure 53: The calculated heat flux of solid argon at 70K

REFERENCES

1. Davis, M.E., *Ordered porous materials for emerging applications.* Nature, 2002. **417**(6891): p. 813-821.

2. Kim, W., R. Wang, and A. Majumdar, *Nanostructuring expands thermal limits.* Nano Today, 2007. **2**(1): p. 40-47.

3. Li, D.Y., et al., *Thermal transport in nanostructured solid-state cooling devices.* Journal of Heat Transfer-Transactions of the ASME, 2005. **127**(1): p. 108-114.

4. Auerbach, S.M., K.A. Carrado, and P.K. Dutta, *Handbook of zeolite science and technology*. 2003, New York: M. Dekker. xii, 1184 p.

5. Cundy, C.S. and P.A. Cox, *The hydrothermal synthesis of zeolites: History and development from the earliest days to the present time.* Chemical Reviews, 2003. **103**(3): p. 663-701.

6. Greenstein, A.M., et al., *Thermal properties and lattice dynamics of polycrystalline MFI zeolite films.* Nanoscale and Microscale Thermophysical Engineering, 2006. **10**(4): p. 321-331.

7. McGaughey, A.J.H. and M. Kaviany, *Thermal conductivity decomposition and analysis using molecular dynamics simulations - Part II. Complex silica structures.* International Journal of Heat and Mass Transfer, 2004. **47**(8-9): p. 1799-1816.

8. Murashov, V.V., *Thermal conductivity of model zeolites: molecular dynamics simulation study.* Journal of Physics-Condensed Matter, 1999. **11**(5): p. 1261-1271.

9. Boerio-Goates, J., et al., *Heat capacity calorimetry - Detection of low frequency modes in solids and an application to negative thermal expansion materials.* Journal of Thermal Analysis and Calorimetry, 2002. **69**(3): p. 773-783.

10. Marinkovic, B.A., et al., *Negative thermal expansion in hydrated HZSM-5 orthorhombic zeolite.* Microporous and Mesoporous Materials, 2004. **71**(1-3): p. 117-124.

11. Gordon, J.M., et al., *The electro-adsorption chiller: a miniaturized cooling cycle with applications to micro-electronics.* International Journal of Refrigeration-Revue Internationale Du Froid, 2002. **25**(8): p. 1025-1033.

12. Wojcik, A.M.W., J.C. Jansen, and T. Maschmeyer, *Regarding pressure in the adsorber of an adsorption heat pump with thin synthesized zeolite layers on heat exchangers.* Microporous and Mesoporous Materials, 2001. **43**(3): p. 313-317.

13. Li, Z.J., et al., *Mechanical and dielectric properties of pure-silica-zeolite low-k materials.* Angewandte Chemie-International Edition, 2006. **45**(38): p. 6329-6332.

14. Wang, Z.B., et al., *Pure-silica zeolite low-k dielectric thin films.* Advanced Materials, 2001. **13**(10): p. 746-749.

15. Davis, M.E., *Zeolite films for low k applications,* U.S. Patents No. 7109130, 2006.

16. Yan,Y., Z. Wang, and H. Wang, *Silica zeolite low-k dielectric thin films*, U.S. Patent No. 6630696, 2003.

17. Yan, Y., *Hydrophilic zeolite coating,* U.S. Patent No. 6849568, 2005.

18. Yan, Y. and D. Beving, *High aluminum zeolite coatings on corrodible metal surfaces*, U.S. Patents No. 7179547, 2007.

19. Coetzer, J. and M.M. Thackeray, *Electrochemical cell and anode for an electrochemical cell* 1981, The South African Inventions Development Corporation.

20. Singhal, S.C., *Advances in solid oxide fuel cell technology.* Solid State Ionics, 2000. **135**(1-4): p. 305-313.

21. Griesinger, A., K. Spindler, and E. Hahne, *Measurements and theoretical modelling of the effective thermal conductivity of zeolites.* International Journal of Heat and Mass Transfer, 1999. **42**(23): p. 4363-4374.

22. Murashov, V.V. and M.A. White, *Thermal properties of zeolites: effective thermal conductivity of dehydrated powdered zeolite 4A.* Materials Chemistry and Physics, 2002. **75**(1-3): p. 178-180.

23. Schelling, P.K., S.R. Phillpot, and P. Keblinski, *Comparison of atomic-level simulation methods for computing thermal conductivity.* Physical Review B, 2002. **65**(14): p. 144306.

24. Berber, S., Y.K. Kwon, and D. Tomanek, *Unusually high thermal conductivity of carbon nanotubes.* Physical Review Letters, 2000. **84**(20): p. 4613-4616.

25. Baerlocher, C., W.M. Meier, and D. Olson, *Atlas of zeolite framework types*. 5th rev. ed. 2001, Amsterdam ; New York: Elsevier. vi.

26. Cundy, C.S. and P.A. Cox, *The hydrothermal synthesis of zeolites: Precursors, intermediates and reaction mechanism.* Microporous and Mesoporous Materials, 2005. **82**(1-2): p. 1-78.

27. Chang, C.D. and A.T. Bell, *Studies on the Mechanism of Zsm-5 Formation.* Catalysis Letters, 1991. **8**(5-6): p. 305-316.

28. Burkett, S.L. and M.E. Davis, *Mechanism of Structure Direction in the Synthesis of Si-Zsm-5 - an Investigation by Intermolecular H-1-Si-29 Cp Mas Nmr.* Journal of Physical Chemistry, 1994. **98**(17): p. 4647-4653.

29. Wang, Z.B. and Y.S. Yan, *Controlling crystal orientation in zeolite MFI thin films by direct in situ crystallization.* Chemistry of Materials, 2001. **13**(3): p. 1101-1107.

30. Choi, J., et al., *Uniformly a-oriented MFI zeolite films by secondary growth.* Angewandte Chemie-International Edition, 2006. **45**(7): p. 1154-1158.

31. Lai, Z.P., M. Tsapatsis, and J.R. Nicolich, *Siliceous ZSM-5 membranes by secondary growth of b-oriented seed layers.* Advanced Functional Materials, 2004. **14**(7): p. 716-729.

32. Xomeritakis, G., et al., *Growth, microstructure, and permeation properties of supported zeolite (MFI) films and membranes prepared by secondary growth.* Chemical Engineering Science, 1999. **54**(15-16): p. 3521-3531.

33. Lai, S.M., L.T.Y. Au, and K.L. Yeung, *Influence of the synthesis conditions and growth environment on MFI zeolite film orientation.* Microporous and Mesoporous Materials, 2002. **54**(1-2): p. 63-77.

34. Boudreau, L.C., J.A. Kuck, and M. Tsapatsis, *Deposition of oriented zeolite A films: in situ and secondary growth.* Journal of Membrane Science, 1999. **152**(1): p. 41-59.

35. Ulla, M.A., et al., *Synthesis and characterization of ZSM-5 coatings onto cordierite honeycomb supports.* Applied Catalysis a-General, 2003. **253**(1): p. 257-269.

36. Greenstein, A.M., *Analysis of Thermal Conductivity Models with an Extension to Complex Crystalline Materials*, PhD Thesis, *S*chool of Mechanical Engineering., Georgia Institute of Technology: Atlanta, 2008.

37. Callaway, J., *Low-Temperature Lattice Thermal Conductivity.* Physical Review, 1961. **122**(3): p. 787.

38. Srivastava, G.P., *The physics of phonons*. 1990, Bristol, England; New York, NY, USA: A. Hilger. xiii.

39. Tien, C.L., A. Majumdar, and F.M. Gerner, *Microscale energy transport*. 1998, Washington, D.C.: Taylor & Francis. xiv.

40. Cahill, D.G., et al., *Nanoscale thermal transport.* Journal of Applied Physics, 2003. **93**(2): p. 793-818.

41. Dove, M.T., *Introduction to lattice dynamics*. Cambridge topics in mineral physics and chemistry; 4. 1993, Cambridge: Cambridge University Press. xvii.

42. Kittel, C., *Introduction to solid state physics*. 7th ed. 1996, New York: Wiley. xi.

43. Che, J.W., et al., *Thermal conductivity of diamond and related materials from molecular dynamics simulations.* Journal of Chemical Physics, 2000. **113**(16): p. 6888-6900.

44. Cahill, D.G., *Thermal-Conductivity Measurement from 30-K to 750-K - the 3-Omega Method.* Review of Scientific Instruments, 1990. **61**(2): p. 802-808.

45. Olson, B. and S. Graham, *Measuring Material Thermal Properties using the 3-omega*. 2003, Sandia National Laboratories

46. Olson, B.W., S. Graham, and K. Chen, *A practical extension of the 3 omega method to multilayer structures.* Review of Scientific Instruments, 2005. **76**(5): p. 053901.

47. Munro, R.G., *Evaluated material properties for a sintered alpha-alumina.* Journal of the American Ceramic Society, 1997. **80**(8): p. 1919-1928.

48. Kittel, C., *Introduction to solid state physics*. 7th ed. 1996, New York: Wiley. xi.

49 Kittel, C. and H. Kroemer, *Thermal physics*. 2d ed. 1980, San Francisco: W. H. Freeman. xvii.

50. Gale, J.D., *GULP: A computer program for the symmetry-adapted simulation of solids.* Journal of the Chemical Society-Faraday Transactions, 1997. **93**(4): p. 629-637.

51. Kramer, G.J., et al., *Interatomic Force-Fields for Silicas, Aluminophosphates, and Zeolites - Derivation Based on Abinitio Calculations.* Physical Review B, 1991. **43**(6): p. 5068-5080.

52. Sanders, M.J., M. Leslie, and C.R.A. Catlow, *Interatomic Potentials for Sio2.* Journal of the Chemical Society-Chemical Communications, 1984(19): p. 1271-1273.

53. Stillinger, F.H. and T.A. Weber, *Computer-Simulation of Local Order in Condensed Phases of Silicon.* Physical Review B, 1985. **31**(8): p. 5262-5271.

54. Hay, D.G. and H. Jaeger, *Orthorhombic Monoclinic Phase-Changes in Zsm-5 Zeolite Silicalite.* Journal of the Chemical Society-Chemical Communications, 1984(21): p. 1433-1433.

55. Park, S.H., et al., *The thermal expansion of the zeolites MFI, AFI, DOH, DDR, and MTN in their calcined and as synthesized forms.* Progress in Zeolite and Microporous Materials, Pts a-C, 1997. **105**: p. 1989-1994.

56. Grau-Crespo, R., E. Acuay, and R.R. Ruiz-Salvador, *A free energy minimisation study of the monoclinic-orthorhombic transition in MFI zeolite.* Chemical Communications, 2002(21): p. 2544-2545.

57. Klemens, P.G., *Thermal Conductivity and Lattice Vibrational Modes.* Solid State Physics-Advances in Research and Applications, 1958. **7**: p. 1-98.

58. McGaughey, A.J.H. and M. Kaviany, *Molecular Dynamics Calculations of the Thermal Conductivity of Silica Based Crystals*, in *8th AIAA/ASME Joint Thermophysics and Heat Transfer Conference*. 2002: S. Louis, Missouri.

59. Holland, M.G., *Analysis of Lattice Thermal Conductivity.* Physical Review, 1963. **132**(6): p. 2461.

60. Morelli, D.T., J.P. Heremans, and G.A. Slack, *Estimation of the isotope effect on the lattice thermal conductivity of group IV and group III-V semiconductors.* Physical Review B, 2002. **66**(19): p. 195304 .

61. Srivastava, G.P., *The Physics of Phonons*. 1990, Bristol, UK: Adam Hilger.

62. Ladd, A.J.C., B. Moran, and W.G. Hoover, *Lattice Thermal-Conductivity - a Comparison of Molecular-Dynamics and Anharmonic Lattice-Dynamics.* Physical Review B, 1986. **34**(8): p. 5058-5064.

63. Klemens, P.G., *The Thermal Conductivity of Dielectric Solids at Low Temperatures - Theoretical.* Proceedings of the Royal Society of London Series a-Mathematical and Physical Sciences, 1951. **208**(1092): p. 108-133.

64. Slack, G.A. and S. Galginaitis, *Thermal Conductivity + Phonon Scattering by Magnetic Impurities in Cdte.* Physical Review a-General Physics, 1964. **133**(1A): p. A253.

65. Debye, P. and J. Kern, *The treatment of coupled systems according to the method of the own oscillations.* Physikalische Zeitschrift, 1914. **15**: p. 490-497.

66. Davis, T.M., et al., *Mechanistic principles of nanoparticle evolution to zeolite crystals.* Nature Materials, 2006. **5**(5): p. 400-408.

67. Gonzalez, G., et al., *Characterization of defects and surface structures in microporous materials by HRTEM, HRSEM, and AFM.* Microscopy and Microanalysis, 2004. **10**(2): p. 224-235.

68. Kaszkur, Z., *Test of applicability of some powder diffraction tools to nanocrystals.* Zeitschrift Fur Kristallographie, 2006: p. 147-154.

69. Vankoningsveld, H., J.C. Jansen, and H. Vanbekkum, *The Monoclinic Framework Structure of Zeolite H-Zsm-5 - Comparison with the Orthorhombic Framework of as-Synthesized Zsm-5.* Zeolites, 1990. **10**(4): p. 235-242.

70. Huang, B.L., A.J.H. McGaughey, and M. Kaviany, *Thermal conductivity of metal-organic framework 5 (MOF-5): Part I. Molecular dynamics simulations.* International Journal of Heat and Mass Transfer, 2007. **50**(3-4): p. 393-404.

71. Ikeda, T., et al., *Structural study of sodium-type zeolite LTA by combination of Rietveld and maximum-entropy methods.* Chemistry of Materials, 1998. **10**(12): p. 3996-4004.

72. Leung, P.C.W., K.B. Kunz, and K. Seff, *Crystal-Structures of Hydrated and Dehydrated Potassium-Exchanged Zeolite-A.* Journal of Physical Chemistry, 1975. **79**(20): p. 2157-2162.

73. Appel, W., et al., *Low-Pressure and Temperature-Dependent Phase-Transitions of a Potassium Exchanged Zeolite-A.* Zeolites, 1987. **7**(5): p. 423-426.

74. Breck, D.W., W.G. Eversole, and R.M. Milton, *New Synthetic Crystalline Zeolites.* Journal of the American Chemical Society, 1956. **78**(10): p. 2338-2339.

75. Breck, D.W., et al., *Crystalline Zeolites .1. The Properties of a New Synthetic Zeolite, Type-A.* Journal of the American Chemical Society, 1956. **78**(23): p. 5963-5971.

76. Bursill, L.A., et al., *New Light on the Crystal-Structure of Zeolite-A.* Journal of Physical Chemistry, 1981. **85**(16): p. 2409-2421.

77. Eddy, M.M., A.K. Cheetham, and W.I.F. David, *Powder Neutron-Diffraction Study of Zeolite Na-Zk-4 - an Application of New Functions for Peak Shape and Asymmetry.* Zeolites, 1986. **6**(6): p. 449-454.

78. Hasegawa, K., et al., *A synchrotron powder diffraction study of Na-LTA.* Japanese Journal of Applied Physics Part 1-Regular Papers Short Notes & Review Papers, 1999. **38**: p. 65-68.

79. Hayashi, H., et al., *Zeolite a imidazolate frameworks.* Nature Materials, 2007. **6**(7): p. 501-506.

80. Ikeda, T., et al., *Structural study of sodium-type zeolite LTA by combination of Rietveld and maximum-entropy methods (vol 12, pg 3996, 1998).* Chemistry of Materials, 2003. **15**(24): p. 4698-4698.

81. Ohgushi, T., A. Yusa, and T. Takaishi, *Percolation of Gases into (K, Ca)-a Zeolites and Their Cation Distribution.* Journal of the Chemical Society-Faraday Transactions I, 1978. **74**: p. 613-621.

82. Pluth, J.J. and J.V. Smith, *Accurate Redetermination of Crystal-Structure of Dehydrated Zeolite-a - Absence of near Zero Coordination of Sodium - Refinement of Si,Al-Ordered Superstructure.* Journal of the American Chemical Society, 1980. **102**(14): p. 4704-4708.

83. Reed, T.B. and D.W. Breck, *Crystalline Zeolites .2. Crystal Structure of Synthetic Zeolite, Type-A.* Journal of the American Chemical Society, 1956. **78**(23): p. 5972-5977.

84. Subramanian, V. and K. Seff, *Near Zero Coordinate Sodium Ion in Dehydrated Zeolite 4a, Na12-A.* Journal of Physical Chemistry, 1977. **81**(24): p. 2249-2251.

85. Sugiyama, S., et al., *AFM observation of double 4-rings on zeolite LTA crystals surface.* Microporous and Mesoporous Materials, 1999. **28**(1): p. 1-7.

86. Takaishi, T., et al., *Changes in Sieving Action and Thermal-Stability of Zeolite-a Produced by Ion-Exchange.* Journal of the Chemical Society-Faraday Transactions I, 1975. **71**(1): p. 97-105.

87. Yanagida, R.Y., A.A. Amaro, and K. Seff, *Redetermination of Crystal-Structure of Dehydrated Zeolite a-4.* Journal of Physical Chemistry, 1973. **77**(6): p. 805-809.

88. Vega, A.J., *A model for random Si/Al distribution in a zeolite framework restricted by Loewenstein's rule.* Journal of Physical Chemistry, 1996. **100**(2): p. 833-836.

89. Yusa, A., T. Ohgushi, and T. Takaishi, *Application of Percolation Theory to Ion-Exchanged Molecular Sieves-A.* Journal of Physics and Chemistry of Solids, 1977. **38**(11): p. 1233-1236.

90. Ohgushi, T., *Relaxation theory for sodium ion in dehydrated Na-A zeolite (LTA) and elucidation of ion movements.* Journal of Physical Chemistry C, 2007. **111**(12): p. 4688-4694.

91. Seff, K. and Shoemake.Dp, *Structures of Zeolite Sorption Complexes .I. Structures of Dehydrated Zeolite 5a and Its Iodine Sorption Complex.* Acta Crystallographica, 1967. **22**: p. 162-170.

92. Armstrong, A.R., et al., *Structure and Electronic-Properties of Cesium-Loaded Zeolite-A.* Journal of Physical Chemistry, 1994. **98**(37): p. 9279-9284.

93. Barrer, R.M. and P.J. Coen, *Dielectric Properties of Some Synthetic Minerals.* Transactions of the Faraday Society, 1963. **59**(490): p. 2376.

94. Barrer, R.M. and P.J. Coen, *Dielectric Loss and Hydration of Sodium Chabazite.* Nature, 1963. **199**(489): p. 587.

95. Freeman, D.C. and D.N. Stamires, *Electrical Conductivity of Synthetic Crystalline Zeolites.* Journal of Chemical Physics, 1961. **35**(3): p. 799.

96. Goto, T., Y. Nozue, and T. Kodaira, *Optical and Magnetic-Properties of Alkali-Metal in Zeolite.* Materials Science and Engineering B-Solid State Materials for Advanced Technology, 1993. **19**(1-2): p. 48-52.

97. Jansen, F.J. and Schoonhe.Ra, *Electrical Properties of Hydrated and Partially Hydrated Zeolites X and Y.* Advances in Chemistry Series, 1973(121): p. 96-105.

98. Jansen, F.J. and Schoonhe.Ra, *Electrical Properties of Crystalline Synthetic Zeolites Types X and Y, Exchanged with Monovalent Cations.* Journal of the Chemical Society-Faraday Transactions I, 1973. **69**(8): p. 1338-1355.

99. Jansen, F.J. and Schoonhe.Ra, *Dielectric Properties of Hydrated Zeolites.* Industrie Chimique Belge-Belgische Chemische Industrie, 1973. **38**(5): p. 526-530.

100. Kasai, P.H., *Electron Spin Resonance Studies of Gamma- and X-Ray-Irradiated Zeolites.* Journal of Chemical Physics, 1965. **43**(9): p. 3322.

101. Kodaira, T., Y. Nozue, and T. Goto, *Optical-Absorption Spectra of Sodium Clusters Incorporated into Zeolite Lta.* Molecular Crystals and Liquid Crystals, 1992. **216**: p. 579-584.

102. Kodaira, T., et al., *Optical-Properties of Potassium Clusters Incorporated into Zeolite Lta.* Physical Review B, 1993. **48**(16): p. 12245-12252.

103. Kodaira, T., et al., *Magnetic and optical properties of sodium clusters in zeolite LTA.* Surface Review and Letters, 1996. **3**(1): p. 717-720.

104. Nozue, Y., T. Kodaira, and T. Goto, *Ferromagnetism of Potassium Clusters Incorporated into Zeolite Lta.* Physical Review Letters, 1992. **68**(25): p. 3789-3792.

105. Nozue, Y., et al., *Ferromagnetic Properties of Potassium Clusters Incorporated into Zeolite Lta.* Physical Review B, 1993. **48**(16): p. 12253-12261.

106. Nozue, Y., et al., *Ferromagnetism of alkali-metal clusters incorporated in the periodic space of zeolite LTA.* Surface Review and Letters, 1996. **3**(1): p. 701-706.

107. Ohba, M., et al., *A unique feature of Bacillus thuringiensis H-serotype flora in soils of a volcanic island of Japan.* Journal of General and Applied Microbiology, 2002. **48**(4): p. 233-235.

108. Ohgushi, T., S. Komarneni, and A.S. Bhalla, *Mechanism of microwave heating of zeolite A.* Journal of Porous Materials, 2001. **8**(1): p. 23-35.

109. Ohgushi, T. and M. Nagae, *Quick activation of optimized zeolites with microwave heating and utilization of zeolites for reusable desiccant.* Journal of Porous Materials, 2003. **10**(2): p. 139-143.

110. Srdanov, V.I., et al., *Evidence for an antiferromagnetic transition in a zeolite-supported cubic lattice of F centers.* Physical Review Letters, 1998. **80**(11): p. 2449-2452.

111. Allen, M.P. and D.J. Tildesley, *Computer simulation of liquids*. 1987, Oxford [Oxfordshire] New York: Clarendon Press ; Oxford University Press. xix.

112. Frenkel, D. and B. Smit, *Understanding molecular simulation : from algorithms to applications*. [2nd ed. 2002, San Diego, Calif. ; London:Academic. xxii.

113. Li, J., L. Porter, and S. Yip, *Atomistic modeling of finite-temperature properties of crystalline beta-SiC - II. Thermal conductivity and effects of point defects.* Journal of Nuclear Materials, 1998. **255**(2-3): p. 139-152.

114. Schelling, P.K., S.R. Phillpot, and P. Keblinski, *Comparison of atomic-level simulation methods for computing thermal conductivity.* Physical Review B, 2002. **65**(14): p. 144306.

115. Volz, S.G. and G. Chen, *Molecular-dynamics simulation of thermal conductivity of silicon crystals.* Physical Review B, 2000. **61**(4): p. 2651-2656.

116. Evans, D.J., *Homogeneous NEMD Algorithm for Thermal-Conductivity - Application of Non-Canonical Linear Response Theory.* Physics Letters A, 1982. **91**(9): p. 457-460.

117. Evans, D.J. and G.P. Morriss, *Statistical mechanics of nonequilibrium liquids*. 1990, London ; San Diego, CA: Academic Press. xiii.

118. Jund, P. and R. Jullien, *Molecular-dynamics calculation of the thermal conductivity of vitreous silica.* Physical Review B, 1999. **59**(21): p. 13707-13711.

119. Maiti, A., G.D. Mahan, and S.T. Pantelides, *Dynamical simulations of nonequilibrium processes - Heat flow and the Kapitza resistance across grain boundaries.* Solid State Communications, 1997. **102**(7): p. 517-521.

120. Oligschleger, C. and J.C. Schon, *Simulation of thermal conductivity and heat transport in solids.* Physical Review B, 1999. **59**(6): p. 4125-4133.

121. Evans, D.J. and G.P. Morriss, *Statistical Mechanics of Nonequilibrium Liquids*. 1st ed. 1990, London: Academic Press.

122. Demontis, P., S. Spanu, and G.B. Suffritti, *Application of the Wolf method for the evaluation of Coulombic interactions to complex condensed matter systems: Aluminosilicates and water.* Journal of Chemical Physics, 2001. **114**(18): p. 7980-7988.

123. Tretiakov, K.V. and S. Scandolo, *Thermal conductivity of solid argon from molecular dynamics simulations.* Journal of Chemical Physics, 2004. **120**(8): p. 3765-3769.

124. Touloukian, Y.S., Thermophysical *properties of matter,* Purdue University, Thermophysical Properties Research Center*,* 1970, New York: IFI/Plenum. 14 v. in 15.

125. McGaughey, A.J.H. and M. Kaviany, *Observation and description of phonon interactions in molecular dynamics simulations.* Physical Review B, 2005. **71**(18): p. 184305

126. Burton, A., et al., *Structure-directing agent location and non-centrosymmetric structure of fluoride-containing zeolite SSZ-55.* Journal of Physical Chemistry B, 2006. **110**(11): p. 5273-5278.

127. Cox, S.D., T.E. Gier, and G.D. Stucky, *2nd Harmonic-Generation by the Self-Aggregation of Organic Guests in Molecular-Sieve Hosts.* Chemistry of Materials, 1990. **2**(5): p. 609-619.

128. Cox, S.D., et al., *Inclusion Tuning of Nonlinear Optical-Materials - Switching the Shg of Para-Nitroaniline and 2-Methyl-Para-Nitroaniline with Molecular-Sieve Hosts.* Journal of the American Chemical Society, 1988. **110**(9): p. 2986-2987.

129. Villaescusa, L.A., et al., *Pure silica large pore zeolite ITQ-7: Synthetic strategies, structure-directing effects, and control and nature of structural disorder.* Chemistry of Materials, 2007. **19**(7): p. 1601-1612.

130. Cola, B.A., et al., *Photoacoustic characterization of carbon nanotube array thermal interfaces.* Journal of Applied Physics, 2007. **101**(5): p. 054313.

131. Lachaine, A. and P. Poulet, *Photoacoustic Measurement of Thermal-Properties of a Thin Polyester Film.* Applied Physics Letters, 1984. **45**(9): p. 953-954.

132. Srinivasan, R., M. Jayachandran, and K. Ramachandran, *Photoacoustic studies on optical and thermal properties of p-type and n-type nanostructured porous silicon for (100) and (111) orientations.* Crystal Research and Technology, 2007. **42**(3): p. 266-274.

133. Srinivasan, R. and K. Ramachandran, *EPR and photoacoustic studies on 30 kev H+ ion-implanted n-GaAs.* Journal of Luminescence, 2007. **124**(1): p. 28-32.

134. Xu, M.H., J.C. Cheng, and S.Y. Zhang, *A new method of reconstruction of thermal conductivity-depth profiles from photoacoustic or photothermal measurements.* Journal of Physics D-Applied Physics, 1998. **31**(21): p. 3154-3159.

135. Zhuo, Y.Z., et al., *Depth profile reconstruction of the thermal conductivity of inhomogeneous solids: application to laser-hardened Al alloys.* Applied Physics a-Materials Science & Processing, 2000. **71**(3): p. 319-323.

136. Oh, W. and S. Nair, *Concentration profiling of a molecular sieve membrane by step-scan photoacoustic spectroscopy.* Journal of Physical Chemistry B, 2004. **108**(26): p. 8766-8769.

137. Oh, W. and S. Nair, *Spatially resolved in situ measurements of the transport of organic molecules in a polycrystalline nanoporous membrane.* Applied Physics Letters, 2005. **87**(15): p. 151912.

138. McGaughey, A.J.H. and M. Kaviany, *Phonon Transport in Molecular Dynamics Simulations: Formulation and Thermal Conductivity Prediction*, in *Advances In Heat Transfer*. 2006, Elsevier, Inc. p. 106.

139. Andersen, H.C., *Molecular-Dynamics Simulations at Constant Pressure and-or Temperature.* Journal of Chemical Physics, 1980. **72**(4): p. 2384-2393.

140. Li, M., W.L. Johnson, and W.A. Goddard III, *Ergodicity and Convergence of Fluctuations in Parrinello-Rahman Molecular Dynamics.* Materials Theory and Modeling, MRS Symposium, 1993. **291**: p. 285